Topics in Strong Dynamics of The Standard Model and Beyond

By

James A. Osborne

A dissertation submitted in partial fulfillment of

the requirements for the degree of

Doctor of Philosophy

(Physics)

at the

UNIVERSITY OF WISCONSIN-MADISON

2017

Date of final oral examination: 05/16/2017

The dissertation is approved by the following members of the Final Oral Committee:

- Yang Bai, Associate Professor, Physics
- Vernon Barger, Professor, Physics
- Sridhara Dasu, Professor, Physics
- Lisa Everett, Professor, Physics
- Pupa Gilbert, Professor, Chemistry

Acknowledgements

First and foremost, I must express my gratitude to my adviser Dr. Yang Bai, without whom this thesis would not be possible.

I wish to thank my other collaborators here at UW Madison: Josh Berger, Sida Lu, and Ben Stefanek, whose contributions to my projects and experience in Madison have been invaluable.

I wish to thank my family for their emotional and financial support. I would especially like to recognize my father and mother, Thomas and Judith Osborne, as well as my grandmother, Helen Brock, for enabling me to pursue my dreams.

Finally, I wish to thank all of the friends who I have met while pursuing my Ph.D. here in Wisconsin, including Ben, Clint, Ed, Ryan, and many others. Without all of you, I would never have made it this far.

Contents

List of Tables

List of Figures

Abstract

We examine the potential for the Large Hadron Collider to discover new physics related to strong dynamics, both within the non-perturbative regime of QCD and also due to possible extensions of the Standard Model involving new QCD-charged particles or new strong gauge groups. We first examine a phenomenological model of the QCD static potential, and determine that it predicts the existence of a $bb\overline{b}\overline{b}$ tetraquark state with a narrow resonance in the four lepton channel at the LHC. We next examine a class of models where scalar dark matter couples to the Standard Model via QCD gluons and explore the signatures of QCD-charged mediators of such interactions. We conclude that mediator-specific searches can greatly improve the sensitivity of the LHC to this class of models. Next, we explore a model of new strong dynamics by introducing an additional $SU(N) \times U(1)$ gauge symmetry under which $SU(5)_{\mathrm{GUT}}$-embedded matter content is charged. We explore the discovery potential of such a model as well as the features that distinguish it from other vector-like $SU(N)$ theories. Finally, we present an improved search method for discovering heavy supersymmetric top partners at the 13 TeV LHC in the kinematic regime with merged top jets.

1 Introduction

The Standard Model of particle physics is a theory describing three of the four known fundamental forces in the universe and categorizes all known elementary particles. The theory was developed throughout the second half of the 20th century, culminating in the current formulation which combines quantum chromodynamics with electroweak theory. It has been an incredibly successful model, including successfully predicting the existences of the top quark (discovered at the Fermilab Tevatron Collider in 1995 [1,2]), the tau neutrino (discovered at the Fermilab DONUT experiment in 2000 [3]), and the Higgs boson (discovered at CERN's Large Hadron Collider in 2012 [4,5]). The Large Hadron Collider is currently probing the validity of the Standard Model at center of mass energies up to 13 TeV, the highest collider energies in history.

However, despite the tremendous success of the Standard Model it is considered incomplete due to both current experimental observations and theoretical considerations. Consequently, there are many proposed extensions to the Standard Model that offer resolution of these issues. Many of the proposed extensions involve strong interactions, either by introducing additional $SU(3)_C$-charged matter content or by extending the Standard Model gauge group to include new strong gauge symmetries. In this dissertation, we examine the potential for the Large Hadron Collider to discover new strong dynamics physics, both within the non-perturbative regime of Standard Model quantum chromodynamics and also possible extensions including new strong dynamics.

This dissertation proceeds as follows. The remainder of this chapter provides a brief overview of the Standard Model, its limitations, and a few popular extensions. Chapter 2 describes a model of the non-perturbative effective potential of quantum chromodynamics and demonstrates its prediction of heavy tetraquark bound states. Chapter 3 examines the search for dark matter at the Large Hadron Collider within the framework of effective field theories, focusing on interactions between dark matter and gluons. Chapter 4 discusses extensions of the Standard Model with new strong dynamics, focusing on a TeV-scale theory with new chiral matter. Chapter 5 examines the state of searches for the supersymmetric partner of the top quark at the Large Hadron Collider.

Gauge Bosons (Spin 1)		Representation
G_μ^a	Color	$(\mathbf{8},\, \mathbf{1},\, 0)$
W_μ^i	Weak isospin	$(\mathbf{1},\, \mathbf{3},\, 0)$
B_μ	Hypercharge	$(\mathbf{1},\, \mathbf{1},\, 0)$
Scalar Bosons (Spin 0)		Representation
H	Higgs field	$(\mathbf{1},\, \mathbf{2},\, \frac{1}{2})$

Fermions (Spin $\frac{1}{2}$)		Representation
Q_L^i	Left-handed quarks	$(\mathbf{3},\, \mathbf{2},\, \frac{1}{6})$
u_R^i	Right-handed u-type quarks	$(\mathbf{3},\, \mathbf{1},\, \frac{2}{3})$
d_R^i	Right-handed d-type quarks	$(\mathbf{3},\, \mathbf{1},\, -\frac{1}{3})$
L_L^i	Left-handed leptons	$(\mathbf{1},\, \mathbf{2},\, -\frac{1}{2})$
e_R^i	Right-handed electrons	$(\mathbf{1}, \mathbf{1}, -1)$

Table 1: Vector boson, scalar boson, and Weyl fermion content of the SM including their representations under the gauge group $SU(3)_C \times SU(2)_L \times U(1)_Y$. Hypercharge normalization is chosen such that the electric charge is $Q = T^3 + Y$. $i = 1, 2, 3$ runs over the three generations of fermions.

1.1 The Standard Model

The Standard Model (SM) describes the strong, weak, and electromagnetic forces within the framework of a quantum field theory. It is an $SU(3)_C \times SU(2)_L \times U(1)_Y$ gauge theory, and all known elementary particles are categorized under representations of this gauge group. The field content of the SM consists of spin-one vector bosons, spin one-half chiral fermions, and a spin-zero scalar field, and is shown in Table 1. This theory has been extensively tested, proving to be robust under the scrutiny of experiments probing up to TeV energy scales.

The full Lagrangian of the SM can be succinctly summarized by

$$\mathcal{L}_{\text{SM}} = \mathcal{L}_{\text{gauge}} + \mathcal{L}_{\text{fermion}} + \mathcal{L}_{\text{Higgs}} + \mathcal{L}_{\text{Yukawa}}\,, \tag{1}$$

where

$$\mathcal{L}_{\text{gauge}} = -\frac{1}{4} G^a_{\mu\nu} G^{a\,\mu\nu} - \frac{1}{4} W^i_{\mu\nu} W^{i\,\mu\nu} - \frac{1}{4} B_{\mu\nu} B^{\mu\nu}\,, \tag{2}$$

$$\mathcal{L}_{\text{fermion}} = \overline{Q}{}^i_L i\not{D} Q^i_L + \overline{u}{}^i_R i\not{D} u^i_R + \overline{d}{}^i_R i\not{D} d^i_R + \overline{L}{}^i_L i\not{D} L^i_L + \overline{e}{}^i_R i\not{D} e^i_R\,, \tag{3}$$

$$\mathcal{L}_{\text{Higgs}} = (D_\mu H)^\dagger\,(D^\mu H) + \mu^2 H^\dagger H - \lambda (H^\dagger H)^2\,, \tag{4}$$

$$\mathcal{L}_{\text{Yukawa}} = -y_u^{ij} \overline{Q}{}^i_L H^c u^j_R - y_d^{ij} \overline{Q}{}^i_L H d^j_R - y_e^{ij} \overline{L}{}^i_L H e^j_R + \text{h.c.}\,. \tag{5}$$

Eq. (2) contains the gauge kinetic terms, Eq. (3) contains the fermion kinetic terms, Eq. (4) contains the Higgs kinetic term and potential, and Eq. (5) contains the terms coupling the fermions to the Higgs field. $F^a_{\mu\nu}$ are the gauge field strength tensors, $\not{D} = \gamma^\mu D_\mu$ are the covariant derivatives appropriate for each fermion's gauge representation, y^{ij} are the Yukawa coupling matrices, and $H^c = i\sigma_2 H^*$ is the charge conjugate of the Higgs field. There are 18 free perturbative parameters in the SM that are fixed by experiment. They are the three gauge couplings, nine Yukawa couplings, three CKM mixing angles, one CKM CP-violating phase, the Higgs boson mass, and the Higgs vacuum expectation value (VEV). There is one additional free non-perturbative parameter, θ_{QCD}, which is briefly discussed in Section 1.2.

Electroweak Symmetry Breaking

The breaking of the $SU(2)_L \times U(1)_Y$ electroweak gauge symmetry to $U(1)_{\mathrm{EM}}$ occurs when the Higgs field H acquires a VEV. The Higgs scalar potential,

$$V(H) = -\mu^2 H^\dagger H + \lambda (H^\dagger H)^2 \,, \tag{6}$$

has a stable minimum at

$$\langle H^\dagger H \rangle = \frac{\mu^2}{2\lambda} \equiv \frac{v_{\mathrm{EW}}^2}{2} \tag{7}$$

for $\mu^2, \lambda > 0$. In unitary gauge, we can shift to the minimum of the potential by letting

$$H \to \frac{1}{\sqrt{2}} \begin{pmatrix} 0 \\ h + v_{\mathrm{EW}} \end{pmatrix} \,, \tag{8}$$

where h is a real scalar field. The Higgs potential then takes the form

$$V(h) = \frac{1}{2} m_h^2 h^2 + \lambda \, v_{\mathrm{EW}} \, h^3 + \frac{\lambda}{4} h^4 \,, \tag{9}$$

where $m_h^2 = 2\mu^2 = 2\lambda \, v_{\mathrm{EW}}^2$ is the mass of the real scalar Higgs boson. This spontaneously breaks the weak isospin and hypercharge symmetries, $SU(2)_L \times U(1)_Y \to U(1)_{\mathrm{EM}}$, leaving one combination, the electromagnetic gauge symmetry, unbroken.

From Goldstone's theorem, there are three residual massless Goldstone bosons. In unitary gauge, one can see that the Goldstone bosons are "eaten" by the weak gauge fields, providing them an additional massive degree of freedom. The eigenstates of the massive vector bosons are

$$W^{\pm}_{\mu} = \frac{1}{\sqrt{2}}\left(W^1_{\mu} \mp i\, W^2_{\mu}\right)\,, \qquad m_W^2 = \frac{1}{4} v_{\rm EW}^2\, g_2^2\,, \tag{10}$$

$$Z^0_{\mu} = \frac{1}{\sqrt{g_1^2+g_2^2}}\left(g_2 W^3_{\mu} - g_1 B_{\mu}\right)\,, \qquad m_Z^2 = \frac{1}{4} v_{\rm EW}^2 \left(g_1^2+g_2^2\right)\,, \tag{11}$$

where g_1 and g_2 are the gauge couplings for $U(1)_Y$ and $SU(2)_L$, respectively. Similarly, the Yukawa couplings between the fermions and the Higgs field generate Dirac masses for the fermions, with masses $m_\psi = v_{\rm EW}\, y/\sqrt{2}$.

Quantum Chromodynamics

After electroweak symmetry breaking, the spectrum of the SM consists of massive Dirac fermions – up-type quarks, down-type quarks, and electrons, charged under the unbroken $SU(3)_C \times U(1)_{\rm EM}$ gauge symmetry – as well as massless neutrinos. Quantum Chromodynamics (QCD) is an $SU(3)$ non-Abelian gauge symmetry, characterized by its infrared (IR) confining behavior. The one-loop QCD beta function is

$$\beta(g_s) \equiv \frac{\partial g_s}{\partial \log \mu} = \frac{g_s^3}{16\pi^2}\left(\frac{2}{3}n_f - 11\right)\,, \tag{12}$$

where g_s is the QCD gauge coupling and n_f is the number of quark flavors with masses $m_q \lesssim \mu$. For $n_f \leq 16$, the beta function is negative, such that the coupling becomes weaker as the energy scale increases, known as asymptotic freedom. Conversely, the coupling gets larger at smaller energies, ultimately becoming non-perturbative. The QCD gauge coupling running is shown in Figure 1.

In a classical field theory, the absence of a mass scale in the theory implies a conformal symmetry. However, the dependence of the gauge coupling on energy in a quantum theory suggests that this conformal symmetry is anomalous. The dimensionless coupling diverges at a scale Λ and a

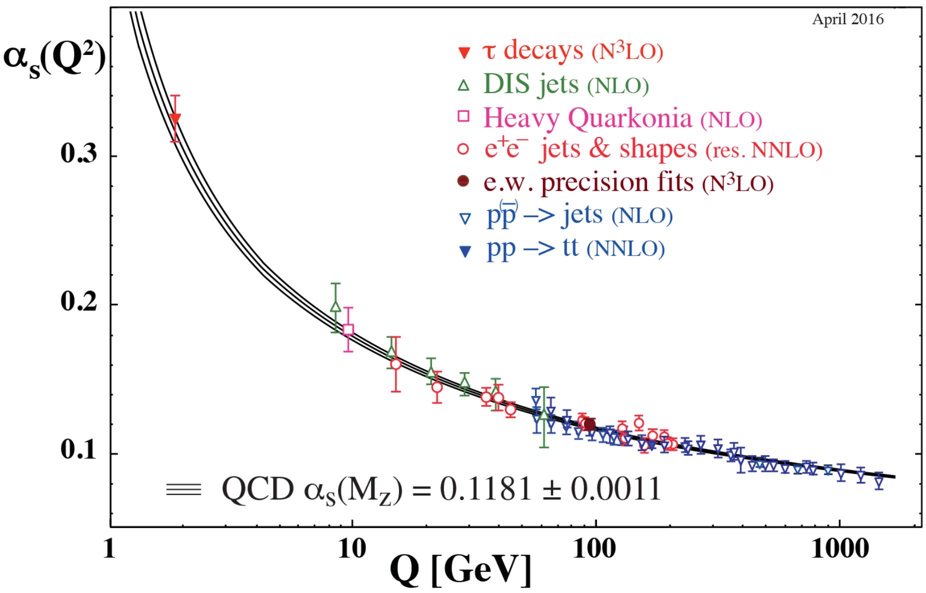

Figure 1: Value of the QCD coupling, $\alpha_s \equiv g_s^2/4\pi$, as a function of energy. Various experimentally determined values are shown at their natural energy scale. The central black line shows the coupling running for the world average value. (Figure from Ref. [6].)

mass scale spontaneously arrises in the theory, known as dimensional transmutation. For QCD, the coupling diverges in the IR, and the scale of divergence is $\Lambda_{\text{QCD}} \sim 150$ MeV. This gives rise to quark confinement, resulting in multiquark states (hadrons) that are described only non-perturbatively within the QCD framework.

Chiral Symmetry Breaking

At low energies, QCD contains only the lightest quarks – up and down – with masses $m_u = 2.3$ MeV and $m_d = 4.8$ MeV in the $\overline{\text{MS}}$ scheme at a renormalization scale of 2 GeV [6]. The theory contains an approximate $SU(2)_L \times SU(2)_R$ global chiral symmetry, characterized by the transformation

$$\psi_{L,R} \equiv \begin{pmatrix} u \\ d \end{pmatrix}_{L,R} \rightarrow \exp\left(-i\,\boldsymbol{\theta}_{L,R} \cdot \boldsymbol{\tau}\right) \psi_{L,R}\,. \tag{13}$$

Dirac mass terms, $m\,\overline{\psi}\psi = m\left(\overline{\psi}_L\psi_R + \overline{\psi}_R\psi_L\right)$, explicitly break this symmetry. Before electroweak symmetry breaking, these terms are forbidden by the $SU(2)_L \times U(1)_Y$ gauge symmetry. After the electroweak symmetry breaks to $U(1)_{\mathrm{EM}}$, the terms are no longer forbidden and the Higgs mechanism generates such masses. However, for the lightest fermions chiral symmetry remains an approximate symmetry of the system.

The very low spectrum of QCD is made up of hadrons, bound states of quarks. This occurs due to the nonperturbative behavior of QCD at low energeis, when the quark condensates develop a non-zero VEV, $\langle\overline{\psi}\psi\rangle$. The condensates spontaneously break the global chiral symmetry to a vectoral isospin symmetry, $SU(2)_L \times SU(2)_R \to SU(2)_V$. From Goldstone's theorem, there would then be three massless Goldstone bosons, the pions $\pi^{\pm}$ and π^0. However, the non-zero masses of the up and down quarks explicitly break this symmetry, and the pions are instead massive pseudo-Goldstone bosons.

If ones includes the next lightest quark in the QCD spectrum, the strange quark with mass $m_s =$ 95 MeV ($\overline{\mathrm{MS}}$ scheme, $\mu = 2$ GeV), the chiral symmetry and its symmetry breaking pattern is extended to $SU(3)_L \times SU(3)_R \to SU(3)_V$. This theory then describes eight pseudo-Goldstone bosons – the three pions, four kaons, and the eta meson.

Chiral Perturbation Theory

As discussed above, at low energies the degrees of freedom in QCD are hadrons rather than quarks and gluons. However, because QCD becomes non-perturbative at those scales, the tools for analytic solutions are limited. A typical approach is instead to develop an effective theory of hadrons which satisfies all the symmetries of the system, but whose coefficients must be determined by experiment, known as Chiral Perturbation Theory (ChiPT). We demonstrate some of the relevant properties of ChiPT below for the two-quark system where pions are the only remaining degrees of freedom.

We begin with a non-linear parameterization of the pion fields,

$$U = \exp\left(i\,\boldsymbol{\tau}\cdot\boldsymbol{\pi}/f_\pi\right) = \exp\left[\frac{i}{f_\pi}\begin{pmatrix} \pi^0 & \sqrt{2}\,\pi^+ \\ \sqrt{2}\,\pi^- & -\pi^0 \end{pmatrix}\right], \tag{14}$$

where f_π is the pion decay constant. At lowest order, the Lagrangian is

$$\mathcal{L}_\pi \supset \frac{f_\pi^2}{4}\,\mathrm{Tr}\left[D_\mu U D^\mu U^\dagger\right] + \frac{f_\pi^2 B_0}{2}\,\mathrm{Tr}\left[m_q U^\dagger + U m_q^\dagger\right] , \tag{15}$$

where B_0 is a constant and m_q is the u, d quark mass matrix. Expanding the second term gives us the bare pion masses in terms of the parameters of the effective theory,

$$m_\pi^2 = (m_u + m_d) B_0 \, . \tag{16}$$

The mass splitting between π^0 and $\pi^\pm$ is mainly due to QED radiative corrections, and is estimated to be

$$\delta m_\pi^2 = m_{\pi^\pm}^2 - m_{\pi^0}^2 \approx \frac{3e^2}{16\pi^2}\,\Lambda^2 \, , \tag{17}$$

where e is the QED coupling constant and $\Lambda \approx 4\pi f_\pi$ is the chiral symmetry breaking scale. A subdominant contribution also arises from the difference in bare quark masses.

Charged pions decay through the weak interactions, predominantly through $\pi^+ \to \ell^+ \, \nu_\ell$. In fact, due to helicity suppression charged pions decay predominantly to muons with a branching fraction $B(\pi^+ \to \mu^+ \, \nu_\mu) = 0.999877$. Neutral pions, however, decay primarily through triangle anomaly diagrams involving virtual nucleons into two photons, $\pi^0 \to \gamma \, \gamma$, with a branching fraction of $B(\pi^0 \to \gamma \, \gamma) = 0.98823$.

Anomaly Cancellation

Gauge anomalies in a quantum field theory arise at one-loop order due to diagrams such as Fig. 2, and lead to negative-norm states which are inconsistent with statistical mechanics. In order to avoid such a catastrophe, the sum of all such diagrams must cancel. An example of anomaly cancellation is shown below for a single generation of SM chiral fermions with hyperchages Y_i. Left-handed

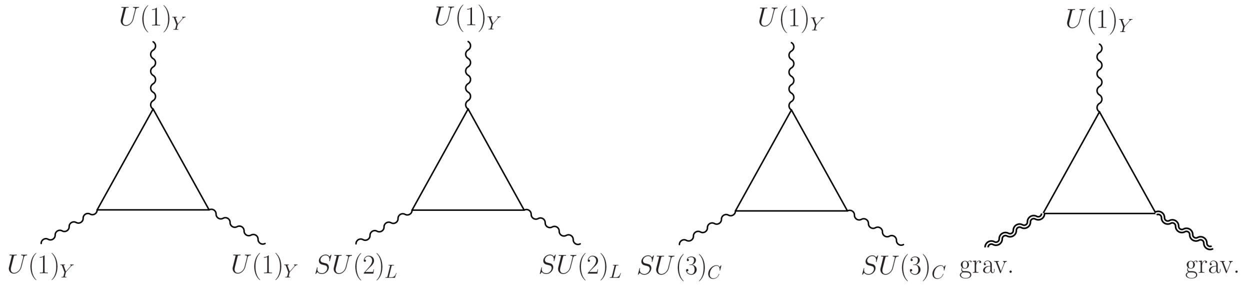

Figure 2: Representative Feynman diagrams contributing to gauge anomalies in the SM. Anomalies with a single external $SU(2)$ or $SU(3)$ vertex vanish due to $\mathrm{tr}[t^a] = 0$ or $\mathrm{tr}[\tau^i] = 0$, and diagrams with three external $SU(2)$ vertices vanish because $\{\sigma^i, \sigma^j\} = 2\delta^{ij}$. Diagrams with three external $SU(3)$ vertices vanish because the QCD couplings are left-right symmetric.

fermions contribute a (-1) relative to right-handed fermions, leading to the cancellation conditions

$$[U(1)_Y, U(1)_Y, U(1)_Y]: \qquad +3Y_{u_R}^3 + 3Y_{d_R}^3 + Y_{e_R}^3 - 6Y_{Q_L}^3 - 2Y_{L_L}^3 = 0\,, \tag{18}$$

$$[U(1)_Y, SU(2)_L, SU(2)_L]: \qquad -3Y_{Q_L} - Y_{L_L} = 0\,, \tag{19}$$

$$[U(1)_Y, SU(3)_C, SU(3)_C]: \qquad +Y_{u_R} + Y_{d_R} - 2Y_{Q_L} = 0\,, \tag{20}$$

$$[U(1)_Y, \mathrm{grav.}, \mathrm{grav.}]: \qquad +3Y_{u_R} + 3Y_{d_R} + Y_{e_R} - 6Y_{Q_L} - 2Y_{L_L} = 0\,, \tag{21}$$

Up to an overall normalization, the unique solution is the hypercharge values shown in Table 1. The gauge anomaly is a chiral anomaly, and so any chiral theory like the SM must ensure such cancellations. In theories with purely vector-like fermions such as QCD, the gauge anomaly cancellation is automatically satisfied.

1.2 Limitations of the Standard Model

Despite the many successes of the SM, it is an incomplete theory. Perhaps the most obvious omission is gravity, which is not incorporated into the theory. Although gravity is by far the weakest known force, the quantum effects of gravity are expected to be non-negligible at energy scales around $M_{\mathrm{Pl}} \sim 10^{19}$ GeV. However, attempting to describe gravitational interactions within the framework of a quantum field theory results in a non-renormalizable theory that is, therefore, not predictive. Dark energy, which accounts for 68% of the total energy of the observable universe in the Standard Model of Cosmology (ΛCDM), is not accounted for within the SM. This energy is believed to drive the observed accelerating expansion of the universe. However, the SM prediction for the cosmological constant is up to 120 orders of magnitude larger than the value obtained using ΛCDM [7].

Baryon asymmetry, the observation that there is more baryonic than antibaryonic matter in the universe, is also not explained within the SM. Electroweak baryogenesis requires that electroweak symmetry breaking be a first-order phase transition, which requires a lighter Higgs boson than the observed $m_H = 125$ GeV. Additionally, the CP violation in the CKM matrix is not enough to account for the observed amount of baryon asymmetry. Theoretically, there are additional complications. Within QCD, another term is allowed by the gauge symmetry which violates CP,

$$\mathcal{L}_{\mathrm{QCD}} \supset -n_f \frac{g_s^2 \theta_{\mathrm{QCD}}}{32\pi^2} G^a_{\mu\nu} \widetilde{G}^{a\,\mu\nu} \,, \tag{22}$$

where $\widetilde{G}^{a\,\mu\nu} = \frac{1}{2}\epsilon^{\mu\nu\rho\sigma} G^a_{\rho\sigma}$. This term would contribute to the neutron electric dipole moment (EDM) d_n, which is currently constrained to be $|d_n| \lesssim 3.0 \times 10^{-26}$ $e{\cdot}$cm [8]. As there is no symmetry to prevent such a term in the SM, requiring such a small (or zero) free parameter represents a *fine tuning* problem, and is known as the *strong CP problem*.

The SM does not include right-handed neutrinos, which would be completely sterile under its $SU(3)_C \times SU(2)_L \times U(1)_Y$ gauge group. Correspondingly, neutrinos do not obtain masses via the Higgs mechanism and remain massless. However, there is now abundant evidence of neutrino oscillations (see, e.g., Ref. [9] and references therein), which occur when their flavor eigenstates differ from their mass eigenstates and thus require massive neutrinos. Measuring the neutrino masses, their mixing, and the amount of CP violation in the neutrino sector is an active area of research. It is currently an open question whether neutrinos are primarily Dirac or Majorana fermions.

Dark Matter

Observations of galactic rotation curves, anisotropies in the cosmic microwave background (CMB), and galaxy collisions like the Bullet Cluster all suggest that the majority of matter in our universe

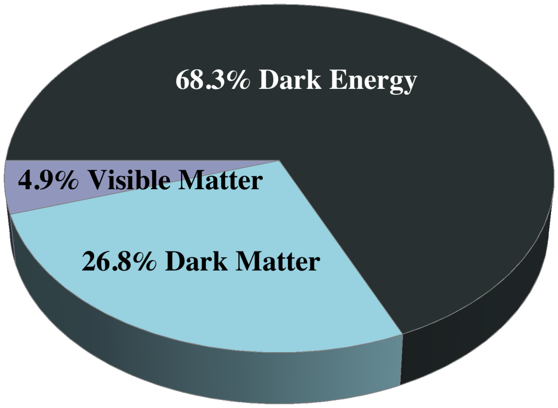

Figure 3: Mass-energy distribution of the observed universe according to the Standard Model of Cosmology.

is non-luminous (see, e.g., Ref. [10] for a recent review). The most widely accepted explanation is the existence of non-baryonic dark matter (DM) which does not interact electromagnetically and must interact with SM particles with tiny cross sections. DM makes up 27% of the mass-energy of the observable universe and 84.5% of the matter. The mass-energy density distribution in the observable universe is shown in Figure 3. The SM, however, does not appear to contain a viable DM candidate. [1]

It is an open question whether the DM particle density was created in thermal equilibrium in the early universe, or arose because of a phase transition. Asymmetric DM is a class of models where their relic abundance is generated due to a particle-antiparticle asymmetry similar to baryon asymmetry. On the other hand, thermal DM is in equilibrium with the SM in the early universe. The DM must be long-lived to have a stable relic abundance, but it can be created or destroyed pairwise via processes such as

$$\overline{\chi}\chi \longleftrightarrow \overline{\psi}\psi\,, \tag{23}$$

where χ is the DM particle. As the universe cools, the thermal energy becomes insufficient to pair-produce new DM, and the back-reaction freezes out. As the DM density declines, the Hubble

---

[1] Ref. [11] proposes a scenario where DM may be explained within the framework of QCD.

expansion of the universe prevents DM particles from finding one another, and a stable particle density is obtained.

An appealing coincidence is uncovered when one examines the cross-section for the process in Eq. (23) required to produce the present-day DM relic abundance. This requirement is $\langle \sigma v \rangle \sim 1$ pb, which is the expected interaction scale for particles interacting under the weak force with masses $m_\chi = \mathcal{O}(100 \text{ GeV})$ and with the expected DM velocitiy spectrum, $\langle v \rangle \sim 0.2\, c$. This coincidence, known as the "WIMP miracle," has motivated a great deal of experimental searches for such particles. However, there is as of yet no conclusive observation of a WIMP-scale DM particle [12].

The Electroweak Hierarchy Problem

Last, a large theoretical motivation driving high energy theory and experiments for the last several decades has been the electroweak hierarchy problem. Unlike classical field theory, in a quantum field theory particles receive radiative corrections to their masses. For fermions, the corrections go as

$$\delta m_\psi \propto \frac{e^2}{16\pi^2}\, m_0 \log\left(\frac{\Lambda_{\text{UV}}^2}{m_0^2}\right) , \tag{24}$$

where m_0 is the bare mass and we have used a momentum cutoff regulator. Λ_{UV} is interpreted as the energy scale at which the effective theory becomes invalid. Even if $\Lambda_{\text{UV}} = M_{\text{Pl}}$, the corrections to fermion masses are small. It can be said that chiral symmetry is protecting the fermion masses, as setting $m_0 \to 0$ restores an exact symmetry of the system and the corrections to fermion masses are of the order of the symmetry-breaking scale m_ψ.

On the other hand, scalar fields receive corrections of the form

$$\delta m_h^2 \propto -\frac{y^2}{16\pi^2}\, \Lambda_{\text{UV}}^2 \,, \tag{25}$$

and are thus quadratically sensitive to the scale of new physics. Scalar masses are not protected by any enhanced symmetry as $m_\phi \to 0$. The dominant Feynman diagram contributing to corrections

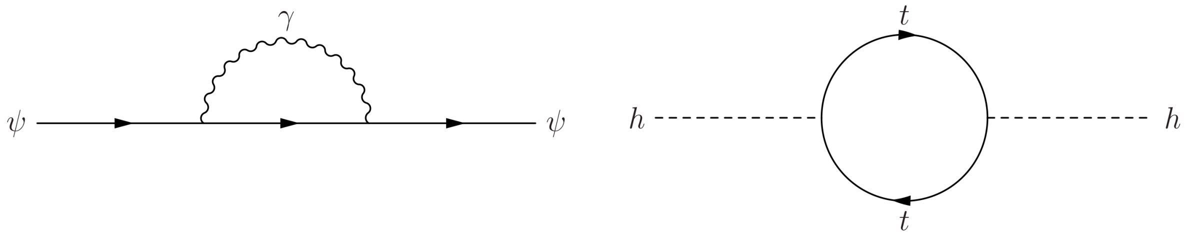

Figure 4: Representative Feynman diagrams contributing to the mass corrections for fermions (**left**) and scalars (**right**).

to the Higgs mass is shown in Figure 4. This is the problem that plagues physicists about the Higgs boson, the only fundamental scalar in the SM. Since we observe the Higgs boson mass to be $m_h = 125$ GeV, there must either be a very fine cancellation between it's bare mass and its radiative corrections, $m_h^2 = m_0^2 + \delta m_h^2 = (125\ \text{GeV})^2$, which is *fine-tuned* for $\Lambda_{\text{UV}} = M_{\text{Pl}}$, or the SM must break down near the electroweak scale, $\Lambda_{\text{UV}} \sim \mathcal{O}(\text{TeV})$. The belief that the electroweak hierarchy problem must be resolved around the TeV scale helped to motivate, in part, the design goals of the LHC.

1.3 Extensions of the Standard Model

Due to the shortcomings of the SM listed in the previous section, there have been many proposals to extend physics beyond the SM (BSM). The simplest extensions attempt to add one or more new particles to the SM in order to explain phenomenon such as DM or neutrino masses. New gauge symmetries and hidden sectors have been proposed which lead to vastly different phenomenology. Theories such as supersymmetry (SUSY), extra dimensions, and partial compositeness can attempt to resolve the electroweak hierarchy problem. Grand unified theories (GUTs) suggest that the electroweak and strong forces may unify at high scales, and present a stepping stone toward a complete theory of everything. Supergravity and string theory attempt to incorporate gravity into a quantum framework. This is by no means an exhaustive list.

An important consequence of many of the above theories is the prediction of new physics near the TeV energy scale, which is currently being probed. There exists a symbiotic relationship between high-energy theory and experiment, with theory able to help guide and shape the future of high-energy experiments while the feedback from such experiments helps to inform and shape the theoretical landscape. Below, we will give a brief introduction to a few of the theories of BSM physics that are relevant to this dissertation.

Grand Unification

The fact that electric charge is quantized is of fundamental importance to the existence of the universe as we know it, and yet there is no explanation for this fact within QED. If, however, all the forces unified into a single gauge symmetry with one unified coupling, this would necessarily be true. Additionally, the three SM gauge couplings run close to a unified value at high energies, providing tantalizing evidence for GUTs. The first GUT was proposed by Howard Georgei and Sheldon Glashow in 1974 [13]. It suggests an embedding of the SM into a single $SU(5)$ gauge group. The gauge group is then spontaneously broken into the SM gauge group $SU(3)_C \times SU(2)_L \times U(1)_Y$ gauge group at the scale M_{GUT}, where the SM couplings diverge from their unified value. Although the simplest $SU(5)$ GUT model can be excluded from limits on proton decay, it can serve as an informative introduction to the topic.

Similar to the Higgs mechanism for electroweak symmetry breaking discussed in Sec. 1.1, symmetry breaking in the Georgi-Glashow model occurs when a heavy scalar in the adjoint representation of $SU(5)$ develops a VEV, with the symmetry breaking pattern $SU(5)_{\text{GUT}} \to SU(3)_C \times SU(2)_L \times U(1)_Y$. The $SU(5)_{\text{GUT}}$ gauge field breaks as

$$24 \to (8,1,0) \oplus (1,3,0) \oplus (1,1,0) \oplus (3,2,-5/6) \oplus (\overline{3},2,5/6)\,, \tag{26}$$

where the first three fields are the SM gauge bosons. The left-handed fermions of the SM (e.g. $u_L = u_R^c$) fit into three generations of $\overline{5} \oplus 10$, which break as

$$\overline{5} \;\to (\overline{3},1,1/3) \oplus (1,2,-1/2)\,, \tag{27}$$

$$10 \to (3,2,1/6) \oplus (\overline{3},1,-2/3) \oplus (1,1,1)\,, \tag{28}$$

and gives the fermion content of Table 1. The SM Higgs doublet is embedded into a fundamental

Chiral Superfields		Spin 0	Spin 1/2	Representation
Squarks, quarks (3 generations)	Q	$(\widetilde{u}_L,\, \widetilde{d}_L)^T$	$(u_L,\, d_L)^T$	$(\mathbf{3},\, \mathbf{2},\, \frac{1}{6})$
	$\overline{u}$	$\widetilde{u}^*_R$	$u^\dagger_R$	$(\overline{\mathbf{3}},\, \mathbf{1},\, -\frac{2}{3})$
	$\overline{d}$	$\widetilde{d}^*_R$	$d^\dagger_R$	$(\overline{\mathbf{3}},\, \mathbf{1},\, \frac{1}{3})$
Sleptons, leptons (3 generations)	L	$(\widetilde{\nu}_L,\, \widetilde{e}_L)^T$	$(\nu_L,\, e_L)^T$	$(\mathbf{1},\, \mathbf{2},\, -\frac{1}{2})$
	$\overline{e}$	$\widetilde{e}^*_R$	$e^\dagger_R$	$(\mathbf{1},\, \mathbf{1},\, 1)$
Higgs, higgsinos	H_u	$(H_u^+,\, H_u^0)^T$	$(\widetilde{H}_u^+,\, \widetilde{H}_u^0)^T$	$(\mathbf{1},\, \mathbf{2},\, \frac{1}{2})$
	H_d	$(H_d^0,\, H_d^-)^T$	$(\widetilde{H}_d^0,\, \widetilde{H}_d^-)^T$	$(\mathbf{1},\, \mathbf{2},\, -\frac{1}{2})$

Vector Superfields	Spin 1/2	Spin 1	Representation
Gluino, gluon	$\widetilde{G}^a$	G^a_μ	$(\mathbf{8},\, \mathbf{1},\, 0)$
Winos, W bosons	$\widetilde{W}^i$	W^i_μ	$(\mathbf{1},\, \mathbf{3},\, 0)$
Bino, B boson	$\widetilde{B}$	B_μ	$(\mathbf{1},\, \mathbf{1},\, 0)$

Table 2: Field content of the MSSM and their representation under the gauge group $SU(3)_C \times SU(2)_L \times U(1)_Y$. Hypercharge normalization is chosen such that the electric charge is $Q = T^3 + Y$. The bar on the $\bar{u}$, $\bar{d}$, $\bar{e}$ is part of our naming convention and does not denote conjugation.

5 of $SU(5)$. The additional Higgs states form a color-triplet scalar, which mediates baryon and lepton number violation and thus must be heavy [14].

Supersymmetry

SUSY is a proposed extension to the SM that includes an additional global symmetry relating bosons and fermions. The explicit symmetry guarantees that the superpartners of the SM fields (spin-0 *squarks* and *sleptons* for SM fermions and spin-1/2 *higgsinos* and *gauginos* for SM bosons) share the same masses and non-spin quantum numbers as their SM counterparts. SUSY is a well-motivated candidate for BSM physics for several reasons: it naturally alleviates the hierarchy problem and potentially includes a DM candidate as discussed in Sec. 1.2, and can unify the SM gauge couplings as discussed in the previous subsection. However, since we have not observed any additional fields differing from the SM fields by only their spin, SUSY must be at best a broken symmetry. Thus, the masses of the superpartners may be heavier than their SM counterparts, while still offering solutions to many of the formerly-mentioned SM issues.

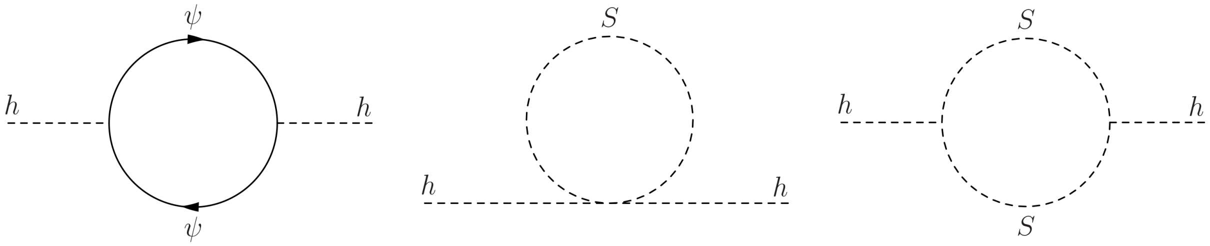

Figure 5: Representative Feynman diagrams contributing to Higgs mass corrections in SUSY. The first two diagrams are quadratically divergent, while the third is logarithmically divergent.

The Minimal Supersymmetric Standard Model (MSSM) is so-named because it contains the minimal amount of additional matter content to supersymmetrize the SM. The field content is shown in Table 2. This more than doubles the matter content of the SM. In particular, there must be an additional Higgs doublet superfield, both because holomorphic requirements dictate that a single Higgs field can not couple to both the up- and down-type quarks and leptons, and also because the addition of only a single higgsino would introduce a gauge anomaly. The superpotential thus contains the terms

$$W_{\text{MSSM}} = \overline{u}\, y_u\, Q\, H_u + \overline{d}\, y_d\, Q\, H_d + \overline{e}\, y_e\, L\, H_d + \mu\, H_u\, H_d\,, \tag{29}$$

where y are 3×3 matrices. Expanding the matter content to incorporate SUSY and including new parameters to break it, the MSSM introduces $\mathcal{O}(100)$ new free parameters compared to the SM.

Additional terms are allowed in the MSSM superpotential from gauge symmetry alone, which are

$$\lambda_1\, \overline{u}\, \overline{d}\, \overline{d} + \lambda_2\, \overline{d}\, Q\, L + \lambda_3\, \overline{e}\, L\, L + \kappa\, L\, H_u\,. \tag{30}$$

Such terms, however, violate baryon or lepton number, and when taken together lead to phenomenologically unacceptable processes such as proton decay. To avoid this, an additional $\mathcal{Z}_2$ symmetry, R-parity, is introduced under which the superfields transform as H_u, $H_d \to H_u$, H_d and Q, $\overline{u}$, $\overline{d}$, L, $\overline{e} \to -\big(Q, \overline{u}, \overline{d}, L, \overline{e}\big)$. Under R-parity all SM fields have parity $+1$ while all their superpartners have parity -1. Not only does this symmetry forbid the above terms, but if R-parity is an exact symmetry it also protects the lightest supersymmetric particle from decay. The lightest

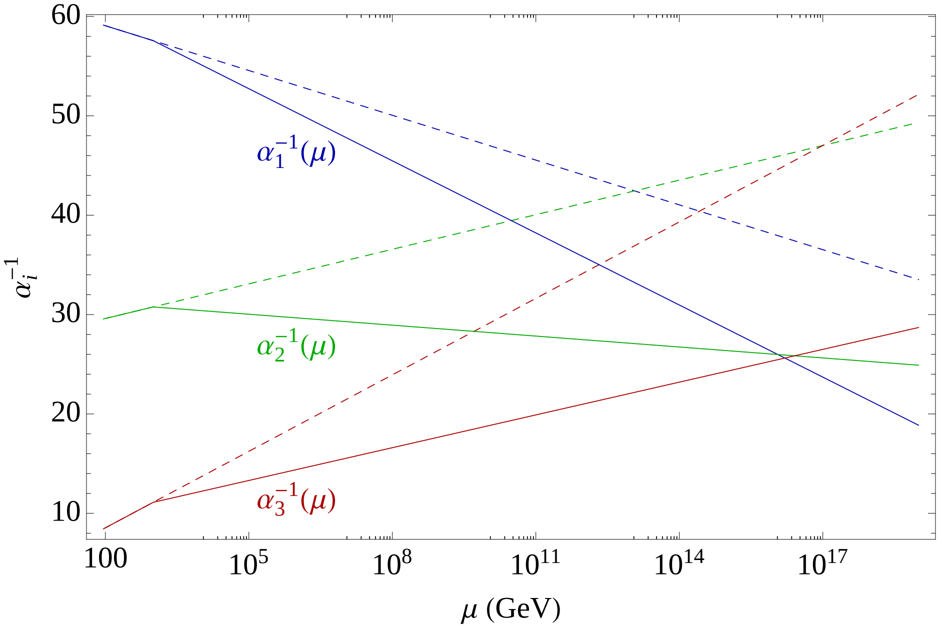

Figure 6: Extrapolation of the running coupling constants for the SM (dashed) and the MSSM (solid) with a universal SUSY scale of $M_{\mathrm{SUSY}} = 1$ TeV. The couplings are $\alpha_3 = g_s^2/(4\pi)$, $\alpha_2 = g_2^2/(4\pi)$, and $\alpha_1 = (\sqrt{5/3}\, g_1)^2/(4\pi)$.

SUSY particle should interact only weakly, and so the theory also predicts a likely WIMP-scale DM candidate.

As a consequence of SUSY, the electroweak hierarchy problem is naturally resolved as long as the scale of SUSY is near the electroweak scale. Because SUSY is a chiral theory, the scalar superpartners inherit the same chiral symmetry protection as their fermionic counterparts. Using a momentum cutoff regulator, corrections to scalar masses such as the Higgs boson in an unbroken SUSY theory are

$$\delta m_h^2 = -\frac{|\lambda_f|^2}{16\pi^2}\Lambda_{\mathrm{UV}}^2 + \frac{\lambda_S}{16\pi^2}\Lambda_{\mathrm{UV}}^2\,, \tag{31}$$

where the first term is the contribution from a Weyl fermion with coupling λ_f, the second term is the contribution from complex scalar loops with coupling λ_S, and the relative minus sign between the first and second terms is due to the closed fermion loop. The Feynman diagrams leading to Eq. 31 are the first two shown in Figure 5. The quadratic divergences are exactly cancelled for

$|\lambda_f|^2 = \lambda_S$, which is guaranteed for SUSY superpartners. However, when SUSY is broken additional contributions from diagrams like the third in Fig. 5 create logarithmically divergent corrections to the Higgs mass proportionate to the SUSY-breaking masses m_S. In this way, the Higgs field is still sensitive to the masses of the heaviest SUSY scalars.

Finally, it is interesting to note that SUSY can dramatically improve the unification of the three SM gauge couplings. The addition of the spectrum of SUSY partners at the scale M_{SUSY} modifies the running couplings of the $SU(3)_C \times SU(2)_L \times U(1)_Y$ gauge group. The one-loop running couplings are shown in Fig. 6 for the SM and the MSSM. The MSSM predicts a unification scale of around $M_{\text{GUT}} \sim 10^{16}$ GeV.

2 Heavy Tetraquarks

QCD is the primary example of strong dynamics within the SM. As an unbroken $SU(3)$ gauge symmetry, QCD confines at low scales and is responsible for the majority of the visible mass in our universe. However, at low energies the coupling becomes strong and perturbation theory, the primary method of calculation within the SM, breaks down. In order to study the low-energy spectrum of hadrons, we turn to either phenomenological models or computationally-expensive Lattice QCD methods. Historically, a great deal of effort was spent to develop and test models of the low-energy QCD effective potential. The short-distance behavior of QCD can be described using a $1/r$ Coulomb-like potential, while the long-distance behavior is best described by a potential linear in r. Models incorporating such behavior have been used extensively to study the spectrum of mesons and baryons.

Recently, signatures of potentially exotic hadrons with four quarks have been observed (e.g. Refs. [15–18]). In each case, the signals are best described by hadrons consisting of at least some light quarks. In these situations, the $1/r$ Coulomb-like potential dominates the interactions. On the other hand, exotic mesons consisting of purely heavy quarks are ideally suited to probe the linear behavior of the QCD potential. In this chapter, we examine a Lattice-motivated phenomenological model of the QCD static potential particularly suited to heavy quark systems where the full multi-body dynamics become important. We use this model to predict the ground state binding energy of a $bb\bar{b}\bar{b}$ system. The main body of this chapter has been reproduced from Ref. [19].

2.1 Introduction

In the seminal work of Ref. [20], Applequist and Politzer interpreted heavy quark bound states as positronium-like atoms subject to non-relativistic quantum mechanics calculations. In this context, the spectroscopy of quarkonia can be well understood by solving Schrödinger's equation based on the static potential between two heavy quarks [21–23] mediated by the asymptotically-free QCD interaction. Ever since, two-body heavy quark systems have been used to understand the long distance behavior of QCD.

Multi-quark states arose as an explanation for the observed spectrum of hadrons in the 1960's. This now universally-accepted picture of mesons (baryons) as two- (three-)quark states has been hugely successful, and suggests that the mass of ordinary matter can be explained by the binding energy between quarks. More recently, enormous progress has been made both theoretically and experimentally in our understanding of four-quark states containing at least one light quark [24,25]. On the other hand, four-quark states containing only heavy quarks have not been directly confirmed by experimental searches. With new data from CMS, ATLAS, and LHCb at the LHC, a multi-quark state containing only bottom and/or charm quarks is very likely to be tested. From the theoretical side, such heavy quark states provide a unique environment to examine the non-relativistic QCD effective potential of many-body systems. In this chapter, we concentrate on a potential tetraquark state comprised of two b and two $\bar{b}$ quarks.

In QED, the equivalent system is the di-positronium molecule (Ps_2), first postulated by Wheeler in 1946 [26]. Using the variational method, the binding energy against dissociation into two positronium atoms is calculated to be 0.435 eV [27–29], which is around 3.2% of the binding energy of two positronium atoms. However, it wasn't until 2007 that the use of positron traps and accumulators led to the experimental confirmation of the Ps_2 molecular state [30]. For the neutral positronium atoms, the electric dipole-dipole interaction can be used to generate the splitting between the ground and excited states. After the standard quantum mechanical perturbative calculation, the additional binding energy can be interpreted in terms of a R^{-6} London-Van der Waals force [31].

For QCD, there is no equivalent chromo-electric dipole interaction for a color-neutral meson, but one still has the transition-dipole interaction from color-neutral state to color-octet state. Depending on the relation between the inter-meson distance and intra-meson binding energy, second-order perturbative calculations reveal a similar R^{-6} London-Van der Waals force [32, 33] or an R^{-7} Casimir-Polder force [34–36]. As emphasized in Ref. [32], the Van der Waals force arises at leading order in α_s and depends only on the geometric ratio of inter-meson and intra-meson binding energies. In the heavy quark limit where the QCD effective potential is Coulomb-like, one can use the Van der Waals force to calculate the additional inter-meson binding energy and obtain a ratio of $\mathcal{O}(1\%)$ of the total intra-meson binding energy, similar to the Ps_2 case. For bottom quarks with finite mass, one should also include a long-range linear contribution to the potential [37].

Several methods have been proposed in the literature to calculate the energies of tetraquark systems comprised of purely heavy quarks. One could, for example, rely on the QCD sum rule method as in Ref. [38]. However, the small separation between quarks in the four-b system requires the use of higher-derivative moments to reliably estimate the non-perturbative bound state physics, which in turn calls into question the convergence of the perturbative expansion for such moments. Even for the two-b system, this approach can become less trustable than the similar charmonium calculations [39]. A separate approach is to treat the $bb(\bar{b}\bar{b})$ system as a composite diquark bound state and then calculate the inter-diquark binding energy [40,41]. However, this simplified approach turns out to be inadequate as the average distance between the two diquarks is comparable to the separation between their constituent quarks, necessitating a complete four-body calculation.

Here, we adopt a phenomenological potential with its parameters determined by fitting to the two-body $b\bar{b}$ spectrum and verified by lattice simulation. We then numerically solve the Schrödinger equation to obtain the ground state energy and approximate wave function for the four-b tetraquark. After that, we discuss spin-dependent (SD) corrections and obtain a final estimate for the ground state mass.

2.2 QCD Static Potential

For a two-body $q\bar{q}$ system, the Cornell potential $V(r) = -4\alpha_s/(3\,r) + r/a^2$ has been widely used to understand bottomonia and charmonia spectroscopy [22,23]. The $-1/r$ Coulomb term is understood simply as the spin-independent contribution from one-gluon exchange. The r/a^2 linear term is the long-range contribution due to QCD confinement. When one extends this phenomenological potential to many-body system, all flux-tube configurations must be checked to minimize the static potential. For three-body systems like baryons, lattice QCD calculations predict that only two flux-tube configurations matter; which one to choose depends on whether an interior angle of the

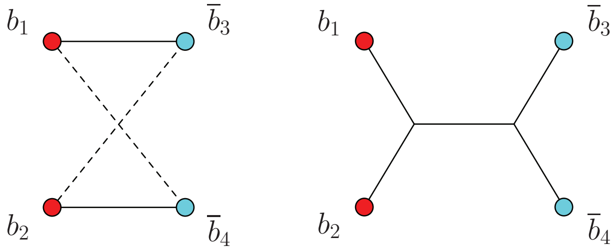

Figure 7: Left panel: the flip-flop configuration of disconnected di-mesons. Right panel: the butterfly configuration with two connected diquarks. The two middle connecting points are chosen to minimize the total path.

triangle formed by the three quarks is greater than 120° [42].

For the four-body system there are in general three relevant configurations, with the flux-tubes reconfiguring in such a way as to minimize the total potential. The first two configurations, which in combination is sometimes referred to as the "flip-flop" configuration, is shown in the left panel of Fig. 7. Depending on the relative distance between (r_{13}, r_{24}) and (r_{14}, r_{23}), one has the di-meson configuration of either $(b_1\bar{b}_3, b_2\bar{b}_4)$ or $(b_1\bar{b}_4, b_2\bar{b}_3)$. The third, so-called "butterfly" configuration, is shown in the right panel of Fig. 7. This is the diquark-diquark configuration with two bottom quarks, b_1 and b_2, forming a color-anti-triplet (or less-favored sextet), and the two anti-bottom quarks, $\bar{b}_3$ and $\bar{b}_4$, forming a color-triplet. For the butterfly configuration, the middle two connecting points should be chosen to minimize the total flux-tube length.

The effective potential for the di-meson system is either

$$V^{\text{di-meson}}_{(13,24)} = -\frac{4\,\alpha_s}{3}\left(\frac{1}{r_{13}} + \frac{1}{r_{24}}\right) + \frac{1}{a^2}\,(r_{13} + r_{24}) \tag{32}$$

or $V^{\text{di-meson}}_{(14,23)}$, which differs only by exchanging $\bar{b}_3 \leftrightarrow \bar{b}_4$. The flip-flop potential is defined as the minimum of the two di-meson configurations for any four-particle phase space and is given by

$$V^{\text{flip-flop}} \equiv \min\left[V^{\text{di-meson}}_{(13,24)}, V^{\text{di-meson}}_{(14,23)}\right]\,. \tag{33}$$

The effective potential for the butterfly configuration is

$$V^{\text{butterfly}} = -\frac{\alpha_s}{3}\left(\frac{1}{r_{13}} + \frac{1}{r_{14}} + \frac{1}{r_{23}} + \frac{1}{r_{24}}\right) - \frac{2\,\alpha_s}{3}\left(\frac{1}{r_{12}} + \frac{1}{r_{34}}\right) + \frac{1}{a^2}\,L_{\text{min}}\,. \qquad (34)$$

Here, L_{min} is the minimum value of the total flux-tube length for all possible connecting points in the right panel of Fig. 7. The formula for the sextet diquark configuration is obtained by replacing the coefficients $(-1/3, -2/3)$ by $(-5/6, 1/3)$. As the sextet configuration has both attractive and repulsive Coulomb forces, it generically leads to a larger potential energy and thus will not contribute to the ground state energy calculation. The total four-quark potential is defined to be the minimum of the three possible configurations and is given by

$$V^{4Q} \equiv \min\left(V^{\text{flip-flop}}, V^{\text{butterfly}}\right)\,. \qquad (35)$$

There is a priori no reason to expect that the two potential parameters, α_s and $1/a$, should have the same values for four-quark states as in two-quark states. Fortunately, the lattice QCD studies of Ref. [43] find consistency in this approach for a large set of four-quark spatial configurations. Therefore, we will use fitted values of α_s and $1/a$ from the two-body quarkonia spectrum to calculate the solution to the four-body Schrödinger equation and obtain the ground state energy.

2.3 Diffusion Monte Carlo

There are a plethora of ways to calculate the energy levels of many-body non-relativistic systems. For the four-lepton di-positronium molecule, variational methods with a very large amount of trial functions have been used to accurately obtain the ground state energy [27–29]. Minimizing the Hamiltonian for so many variational parameters, however, can be extremely computationally expensive (see Ref. [44] for a recent attempt). For our numerical calculation, we will instead adopt the more efficient but perhaps less accurate Diffusion Monte Carlo (DMC) method (see Ref. [45] for an introduction). To test the numerical calculation, we successfully reproduced the binding energy for the di-positronium molecule.

The central idea behind the DMC method is to replace real time by an imaginary time and adjust the guessed ground state energy based on the behavior of the wave function. The time-dependent wave function evolves as $\sum_n e^{-iE_nt}\Psi_n(\vec{x})$, where E_n and $\Psi_n(\vec{x})$ are the true energy eigenvalues and eigenfunctions of the Hamiltonian, respectively. Scaling the energy eigenvalues E_n by a constant guessed value E_g makes no physical change to wave function. Thus, after making the substitutions $E_n \to E_n - E_g$ and $t \to -i\tau$, the evolution of the wave function becomes $\sum_n e^{-(E_n-E_g)\tau}\Psi_n(\vec{x})$. When $E_g \approxeq E_0$, only the ground state wave function will be stable while the excited states will diffuse away. If $E_g > E_0$, the wave function will diverge, while for $E_g < E_0$ even the ground state will diffuse away. By adjusting the value of E_g based on the behavior of the wave function, we are able to obtain the correct ground state energy.

Practically, the wave function in the DMC algorithm is represented by random walks of many particles in phase space. To observe the behavior of the wave function with respect to E_g, a "birth-death" mechanism is implemented such that when E_g is too large, the particles will replicate themselves to increase the total number of particles, and vise versa. For each step, the algorithm adjusts E_g based on the change in the total number of particles until it converges to the ground state energy E_0. The stabilized walker distribution then gives us the ground state wave function.

For the system at hand, we also need to find $L_{\min}$ for the butterfly configuration. This is similar to the well-known Fermat and Torricelli problem to link three points with a minimal network, which is a special case of the Steiner tree problem in mathematics. The added connecting points in the middle are known as Steiner points, and the original points are called terminals. In two-dimensional space, the Steiner tree problem has an analytical solution, however it is still an NP-complete problem in higher dimensions. To find the positions of the two Steiner points the Steiner configuration for the two vertices in the right panel of Fig. 7, we adopt Smith's algorithm [46]. This iterative algorithm determines an equation for each Steiner point, k, from summing all possible links surrounding it to both terminals and other Steiner points: $\sum_{kj-\text{linked}}(\vec{x}_k^{(i+1)} - \vec{x}_j^{(i+1)})/|\vec{x}_k^{(i)} - \vec{x}_j^{(i)}| = 0$. Here, $\vec{x}_j^{(i)}$ is the position of point j after the i-th iteration. Usually after only 20 iterations this algorithm gives a solution that matches the true solution to a very high precision.

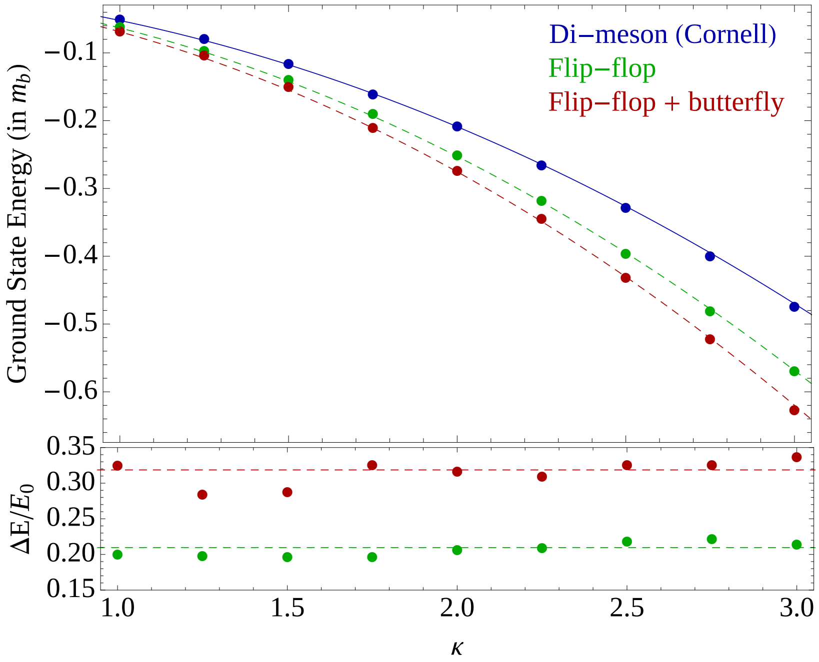

Figure 8: The ground-state energy for three different static potentials using Benchmark-I of Eq. (36) as a function of an effective numerical running parameter κ. The lower panel shows the ratios of binding energy difference for the flip-flop and flip-flop+butterfly configurations over the dissociated di-meson binding energy.

2.4 Spin-Independent Binding Energy

To calculate the tetraquark mass, we will adopt two sets of benchmark parameters for m_b, α_s and $1/a$,

$$\begin{aligned} \text{BM-I}: \quad & m_b = 4.79\ \text{GeV}\,, \quad \alpha_s = 0.38\,, \quad a = 2.43\ \text{GeV}^{-1}\,, \\ \text{BM-II}: \quad & m_b = 5.17\ \text{GeV}\,, \quad \alpha_s = 0.36\,, \quad a = 2.34\ \text{GeV}^{-1}\,. \end{aligned} \tag{36}$$

Both of them can provide a good fit to the bottomonium spectra [22, 23], although the second one requires a universal shift of energy levels of around −0.77 GeV, to take into account that the dynamic bottom-quark mass could be different from the bare heavy quark mass.

To check the stability of our numerical calculation, we fix the DMC parameters—initial particle number, time step, and simulation length—and modify the total potential by an overall factor of

	Benchmark-I	Benchmark-II
$E_0/2$ (di-meson)	9.455 GeV	9.460 GeV
ΔE (flip-flop)	-52 MeV	-51 MeV
ΔE (flip-flop+butterfly)	-80 MeV	-79 MeV

Table 3: Additional binding energy for the two benchmark parameter sets of Eq. (36).

κ. This is equivalent to scaling the reduced mass and ground state energy while keeping numerical running conditions fixed. In dimensionless units, the binding energy is anticipated to scale as κ^2, which is clear from Fig. 8. Furthermore, the ratio of additional binding energy, ΔE, over the di-meson binding energy, E_0, for the flip-flop and flip-flop+butterfly potentials should be independent of κ, which is also approximately true up to small numerical fluctuations. From the lower panel of Fig. 8, it is clear that the flip-flop and flip-flop+butterfly configurations account for an additional 20% and 30% binding energy, respectively.

In Table 3, we show the additional binding energy due to the different four-particle effective potential configurations. Within the error of our calculation, we have found that an additional ~ 50 MeV and ~ 80 MeV of binding energy can be attributed to the flip-flop or flip-flop+butterfly configurations. The total binding energy for the flip-flop+butterfly configuration is around 330 MeV for BM-I and 300 MeV for BM-II (without accounting for the constant energy shift of -0.77×2 GeV). These binding energies are large enough to suggest that the four b state should be treated as a true tetraquark system rather than a weakly-coupled molecular system.

Before we move on to discuss the spin-dependent corrections, we show the wave functions for the tetra-quark state. To generate the wave functions in Fig. 9 and simplify the multiple-dimension numerical integration, we have treated the wave-function as approximately flat in r_{12} and r_{34} and kept the remaining three variables: r_{13}, r_{14} and a relative angle between them. In the upper panel of Fig. 9, we show the squared wave function times r_{13}^2 for different static potentials, while in the lower panel we show the value of the squared wave function near the origin. One can see that the squared wave function for the flip-flop+butterfly potential is around 0.59 of the value for dissociated

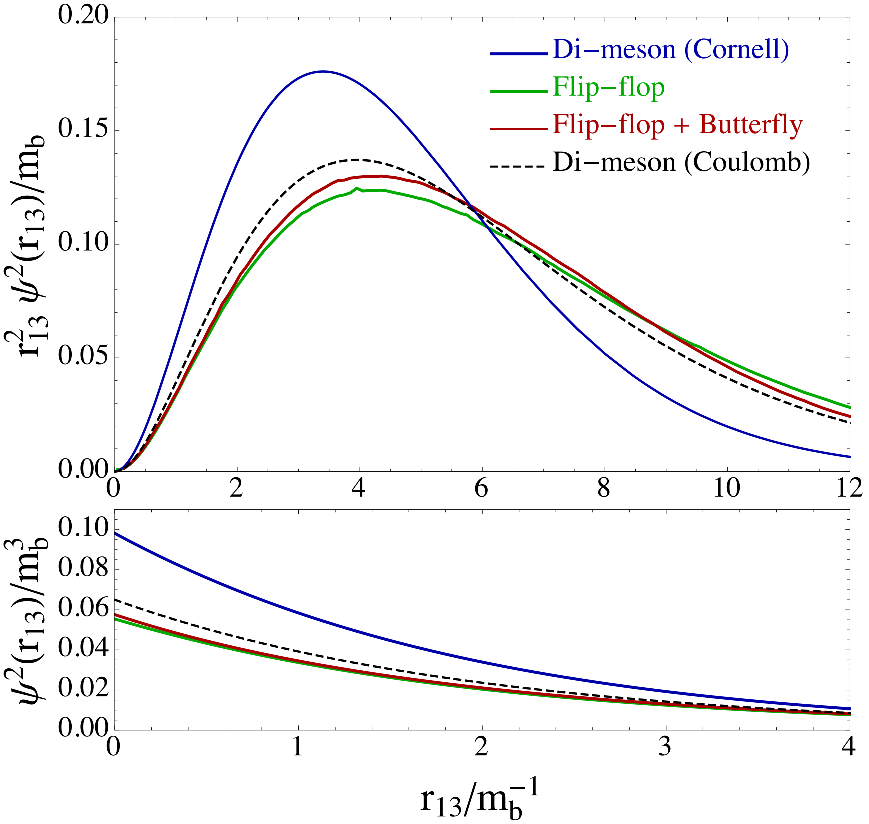

Figure 9: The squared wave function in terms of r_{13} for different static potentials using benchmark-I of Eq. (36).

di-meson configuration at the origin. There is only around 5% difference between the flip-flop and flip-flop+butterfly squared wave functions. We also note that because of the symmetries $\bar{b}_3 \leftrightarrow \bar{b}_4$ and $b_1 \leftrightarrow b_2$, the wave functions are identical when plotted in terms of r_{14}, r_{23} or r_{24}.

2.5 Spin-Dependent Corrections

For a two particle system, short-range spin-dependent interactions contain a local δ-function force [47, 48]

$$H_{\mathrm{SD}} \supset \Delta C_2\, \alpha_s\, \frac{2}{3\, m_1\, m_2}\, \vec{s}_1 \cdot \vec{s}_2\, 4\pi\, \delta(r_{12})\,, \tag{37}$$

with ΔC_2 as the difference of quadratic Casimir. For the four particle system, we anticipate the ground state spatial wave function to be predominantly S-wave so additional corrections proportional to $\vec{L}\cdot\vec{S}$ should be negligible. From Fig. 9, it is apparent that the wave function for the flip-flop configuration closely approximates the wave function for the flip-flop + butterfly configuration. Thus, to implement the SD correction for the 0^{++} tetraquark, we will focus on the flip-flop configuration.

The general ground state wave function for the flip-flop di-meson configuration is

$$\Psi = \begin{cases} \psi(r_{13})\,\psi(r_{24}) \otimes |(b_1\bar{b}_3)_1(b_2\bar{b}_4)_1\rangle \otimes \chi^{(0,0)}_{13,24} & \text{for } R_1\,, \\ \psi(r_{14})\,\psi(r_{23}) \otimes |(b_1\bar{b}_4)_1(b_2\bar{b}_3)_1\rangle \otimes \chi^{(0,0)}_{14,23} & \text{for } R_2\,. \end{cases} \tag{38}$$

Here, R_1 represents the region with $V^{\text{di-meson}}_{(13,24)} < V^{\text{di-meson}}_{(14,23)}$ and otherwise for R_2; $(b_1\bar{b}_3)_1$ represents the color-singlet contraction of b_1 and $\bar{b}_3$. The product of the spatial and color wave functions is symmetric under the interchange of $b_1 \leftrightarrow b_2$ and $\bar{b}_3 \leftrightarrow \bar{b}_4$, so the spin-zero wave functions should be

$$\chi^{(0,0)}_{13,24} = +\frac{1}{2}(b_1^{\uparrow}b_3^{\downarrow} - b_1^{\downarrow}b_3^{\uparrow})(b_2^{\uparrow}b_4^{\downarrow} - b_2^{\downarrow}b_4^{\uparrow})\,, \tag{39}$$

$$\chi^{(0,0)}_{14,23} = -\frac{1}{2}(b_1^{\uparrow}b_4^{\downarrow} - b_1^{\downarrow}b_4^{\uparrow})(b_2^{\uparrow}b_3^{\downarrow} - b_2^{\downarrow}b_3^{\uparrow})\,. \tag{40}$$

The relative minus between the above two terms is necessary to satisfy the Pauli exclusion principle, and provides the lowest ground state energy after hyperfine splitting.

Calculating the matrix element $\langle\Psi|H_{\text{SD}}|\Psi\rangle$, the spin-dependent correction for the 0^{++} ground state is approximately

$$\begin{aligned} \Delta E_{\text{SD}} &= -\frac{4\,\alpha_s(\mu)}{3}\,\frac{1}{m_b^2}\,\left[\psi^2(r_{13}=0) + \psi^2(r_{24}=0)\right] \\ &\approx -145 \pm 30\ \text{MeV}\,, \end{aligned} \tag{41}$$

for BM-I with $\alpha_s(2\,m_b) \approx 0.2$. The result for BM-II is similar. The symmetries $b_1 \leftrightarrow b_2$ and

$\bar{b}_3 \leftrightarrow \bar{b}_4$ imply that the contributions of R_1 and R_2 to the matrix element are the same, and thus we double the expression for region R_1 in our calculation. Here, the relative error is taken to be $\mathcal{O}(\alpha_s) \approx 20\%$ [49] and should only be used as guidance from the theoretical calculation. Altogether, the energy for the ground state 0^{++} mode is

$$M(0^{++}) = 18.69 \pm 0.03 \text{ GeV}\,, \tag{42}$$

which is below the energy thresholds of $2M(\eta_b) = 18.798$ GeV and $2M[\Upsilon(1S)] = 18.920$ GeV.

2.6 Discussion

For the di-positronium molecule, the leading decay channel comes from e^+e^- annihilation, giving $\text{Ps}_2 \to 2\gamma + e^+e^-$ [50]. Similarly, the leading decay channel for the four-b tetraquark ground state is $0^{++} \to 2g + b\,\bar{b}$. The decay width is $\mathcal{O}(10 \text{ MeV})$ and is comparable to the decay width of η_b. It can also decay into one on-shell and one off-shell $\Upsilon(1S)$ via spin rearrangement [51], providing a possible four-lepton final state resonance: $0^{++} \to \Upsilon(1S)\Upsilon(1S)^* \to \ell^+\ell^-\ell^+\ell^-$ with ℓ as e, μ, on top of the continuous double $\Upsilon(1S)$ background [52].

Within the framework of our calculation, one could also calculate heavier states including spin-one and spin-two excitations. The detailed mass spectrum requires one to calculate the spatial excitation energy as well as the full wave-functions in terms of all degrees of freedom. These are conceptually straightforward, but numerically complicated. Furthermore, one could also apply our calculation procedure to other four-heavy quark system like $c\bar{c}c\bar{c}$ and $c\bar{c}b\bar{b}$. For instance, the ground state, 0^{++}, of $c\bar{c}c\bar{c}$ is estimated to be 5.97 ± 0.04 GeV, using benchmark-I in Eq. (36) with $m_c = 1.37$ GeV and $\alpha_s(2m_c) \approx 0.25$ for the spin-dependent correction. While this is below twice the J/Ψ mass, it is unclear within the calculation's uncertainty if the ground state will be below twice the η_c mass, $2M(\eta_c) = 5.966$ GeV. Similar to the four-b state, this ground state could have a decay mode of $0^{++} \to \Psi(1S)\Psi(1S)^* \to \ell^+\ell^-\ell^+\ell^-$. However, if the decay channel to two on-shell η_b is open the branching ratio to this four-lepton final state may be significantly smaller than in the four-b case.

In summary, based on the static potential of the flux-tube model for four heavy quark interactions we have used a diffusion Monte Carlo algorithm to numerically solve the many-body non-relativistic Schrödinger equation. We have found a ground state, 0^{++}, with a mass of 18.69 ± 0.03 GeV, which is approximately 100 MeV below twice the mass of η_b expected for a disassociated di-meson ground state. Our calculation predicts the existence of an observable new state made of purely non-relativistic heavy quarks, whose discovery can help further our understanding of QCD long-range forces.

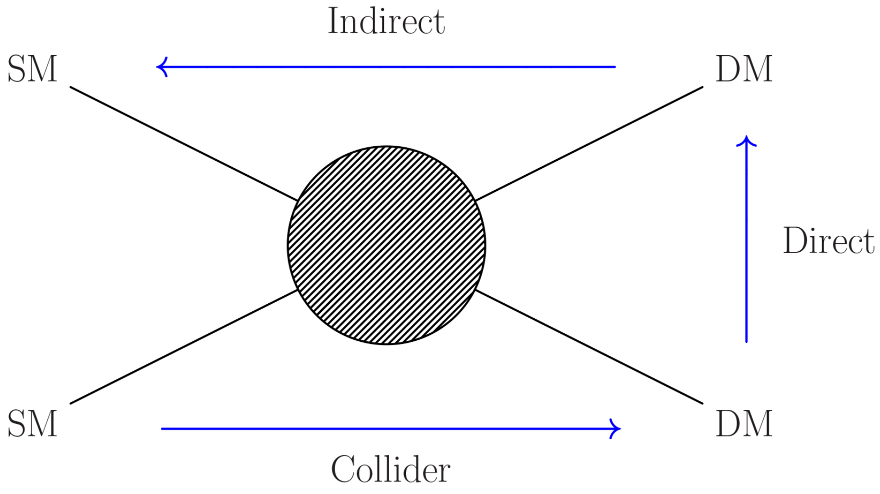

Figure 10: A representation of interactions between DM and the SM. The blue arrows show the direction of time flow for the different types of experimental searches.

3 Chromo-Rayleigh Interactions of Dark Matter

As discussed in Sec. 1.2, the existence of DM is well-established. One of the primary mysteries surrounding DM is what, if any, non-gravitational interactions it has with the SM. There are three primary ways we search for such interactions: direct detection experiments look for evidence of DM-nucleon scattering, indirect detection experiments look for astronomical evidence of DM annihilating into SM particles, and collider searches aim to directly produce DM via high-energy collisions of SM particles. A representative Feynman diagram showing the relationship between these three strategies is shown in Fig. 10. It is an open question as to what interactions complete the bubble in the diagram.

Interactions between WIMP-scale DM and nucleons have been extensively searched for by terrestrial direct detection experiments, however there has yet to be any conclusive evidence for DM-nucleon interactions. Recent limits on the DM-nucleon cross section from direct detection experiments are shown in Fig. 11. As can be seen, the interaction cross section has become increasingly constrained for typical DM masses of $m_\chi \gtrsim 10$ GeV. For lighter DM, however, the recoil energy of the nucleons in direct detection experiments is likely below the detector thresholds, and the constraints are weaker. In this regime, collider searches may provide better sensitivity to DM than direct detection searches.

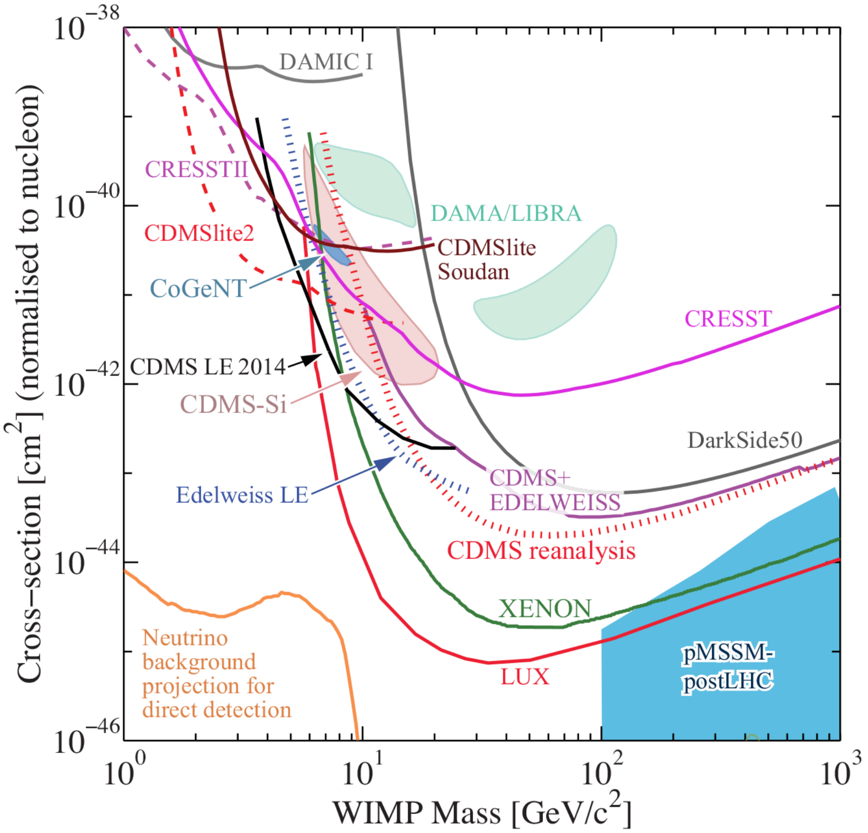

Figure 11: Limits on the wimp-nucleon spin-independent cross section as a function of DM mass. The DAMA/LIBRA, CDMS-Si, and CoGeNT shaded regions represent potential signals. These regions, however, appear to be excluded from various other experiments. This figure was reproduced from Ref. [6].

The mechanism for interaction between DM and SM fields is important for predicting the expected sensitivity of the LHC. The LHC, as a proton-proton collider, is especially sensitive to new QCD-charged particles. Although DM must be color-neutral, interactions with new QCD-charged particles provide direct portal to DM production at the LHC. In this chapter, we explore the constraints on DM interactions with QCD gluons, first within the framework of an effective field theory and then with a simple UV-complete model where DM interacts with new heavy QCD-charged fields. The main body of this chapter has been reproduced from Ref. [53], and reflects the state of the field at the time of its publishing.

3.1 Introduction

Although there is no doubt that DM interacts gravitationally both among itself and with SM particles, we still have no convincing evidence for other dark matter interactions. Among the three forces in the SM, DM can not have order-one couplings under the electroweak forces. Otherwise, it will either emit photons or scatter off nuclei with a too-large cross section in direct detection experiments. Suppressed couplings to the Z boson or the Higgs boson will be probed further in upcoming dark matter experiments [54]. For QCD interactions, the DM particle can not have a color charge due to confinement. If, instead, it is a QCD composite particle, the hadronic bound states should have a large interaction strength with SM pions and thus have a large scattering cross section with nucleons. This type of dark matter can not penetrate the Earth to reach detectors in underground direct detection experiments, but satellite-based X-ray quantum calorimetry experiments impose stringent bounds on the scenario [55].

Another way for dark matter to interact with gluons is through effective contact interactions, comparable to photon–molecule Rayleigh interactions. Introducing such higher-dimensional effective operators to describe dark matter *chromo-Rayleigh* interactions is then independent of whether the dark matter is elementary or composite. For instance, in supersymmetric models the neutralino can couple to two gluons via a stop–top quark loop. In extra-dimensional models, a similar loop from the top quark and its Kaluza-Klein mode can generate the effective chromo-Rayleigh dark matter interaction [56]. Composite dark matter models can also generate chromo-Rayleigh interactions, with strengths typically suppressed by the composite scale [57]. In this chapter, we perform a generic study on dark matter chromo-Rayleigh interactions. We pay particular attention to collider searches and the potential signatures associated with chromo-Rayleigh interactions. This study is similar to searches for electrical Rayleigh interactions of dark matter in Ref. [58, 59], where the electrically charged particles can be searched for directly at the LHC.

For simplicity, we choose the dark matter particle to be a complex scaler denoted as X. We study two types of dimension-six interactions: $X^\dagger X\, G^2$ and $\left(XX - X^\dagger X^\dagger\right) G\widetilde{G}$, where G is the QCD field tensor. For direct detection searches, the first operator provides spin-independent scattering while the second operator provides spin-dependent and momentum-suppressed scattering. For collider searches, the SM-independent signature is a mono-jet plus missing transverse energy. Taking into account the well-known limitations of such searches [60–77], we introduce simplified models to UV-complete these two operators. Collider signatures owing to such UV-completions depend strongly on how the colored mediators decay. We discuss several possible signatures, including multi-jets and pair-produced di-jet resonances with missing transverse energy.

3.2 Contact Interactions

Our model consists of a complex scalar dark matter field, X, which is a singlet under the SM gauge group. We introduce the following two CP-conserving, dimension six operators coupling dark matter to the gluon field

$$\mathcal{O}_1^{\text{cRayleigh}} = \frac{\alpha_s}{4\,\pi\,\Lambda_1^2} X^\dagger X G^a_{\mu\nu} G^{a\,\mu\nu}\,, \tag{43}$$

$$\mathcal{O}_2^{\text{cRayleigh}} = \frac{i\,\alpha_s}{4\,\pi\,\Lambda_2^2} (XX - X^\dagger X^\dagger) G^a_{\mu\nu} \widetilde{G}^{a\,\mu\nu}\,, \tag{44}$$

where Λ_i is the cutoff scale and $\widetilde{G}^{a\,\mu\nu} = \frac{1}{2}\,\epsilon^{\mu\nu\alpha\beta} G^a_{\alpha\beta}$ is the dual gluon field strength tensor. The overall operator normalization accounts for a loop factor. In order for X to be stable, we impose a $\mathcal{Z}_2$ symmetry under which X is odd. Based on these two effective operators, we first calculate the thermal relic abundance, direct detection cross sections, and collider constraints.

Thermal Relic Abundance

Depending on the UV physics, the dark matter sector could be more complicated than just one state. Therefore, the dark matter thermal relic abundance calculation based entirely on the operators in Eqs. (43) and (44) can only provide a guidance for the potential parameter space in M_X and Λ_i for thermal dark matter. For the first operator, we have the dark matter self-annihilation rate from the process $X^\dagger X \to G\,G$ as

$$\frac{1}{2}\left[\langle\sigma v\rangle(X^\dagger X \to G\,G)\right] = \frac{1}{2}\left[\frac{\alpha_s^2}{\pi^3}\,\frac{M_X^2}{\Lambda_1^4}\right] \equiv s\,, \tag{45}$$

to leading order in the dark matter's relative velocity v expansion. Here, the overall factor of 1/2 is due to the relic density being comprised of particles and antiparticles. For the second operator, we have the annihilation rate from the process $XX[X^\dagger X^\dagger] \to G\,G$, in terms of components with $X = (X_R + iX_I)/\sqrt{2}$, as

$$\frac{1}{2}\left[\langle\sigma v\rangle(X_R X_I \to G\,G)\right] = \frac{1}{2}\left[\frac{\alpha_s^2}{\pi^3}\,\frac{M_X^2}{\Lambda_2^4}\right] \equiv s\,. \tag{46}$$

The dark matter relic abundance is inversely proportional to the annihilation rate and has a formula $\Omega_X h^2 \approx 1.07\times 10^9~\mathrm{GeV}^{-1}\,x_F/(\sqrt{g^*}\,M_{\rm pl}\,s)$ with g^* as the number of relativistic degrees of freedom at the freeze-out temperature and is taken to be 86.25 and the Planck scale is $M_{\rm pl} = 1.22\times 10^{19}$ GeV. The freeze-out temperature x_F is given by $x_F = \ln\left[0.05\,g\,M_{\rm pl} M_X s/(\sqrt{g^*\,x_F})\right]$ with $g = 2$ and is typically $\mathcal{O}(20)$.

Direct Detection

For the first operator $\mathcal{O}_1^{\rm cRayleigh}$, we can use the matrix element of $G^a_{\mu\nu}G^{a\,\mu\nu}$ inside a nucleon to derive the dark matter coupling to two nucleons. The trace anomaly of the QCD energy-momentum tensor implies [78, 79]

$$m_N\langle N|N\rangle = \langle N|\sum_{1\le i\le n_f} m_i\overline{\psi}_i\psi_i(1+\gamma) + \left(\frac{\beta^{n_f}}{2\,\alpha_s^2}\right)\alpha_s G^a_{\mu\nu}G^{a\,\mu\nu}|N\rangle\,, \tag{47}$$

where $\beta^{n_f} = -(11-2n_f/3)\alpha_s^2/4\pi$ is the beta function at leading order, n_f is the number of quarks, and γ is the anomalous dimension of the quark field. So, at leading order in α_s and keeping only $n_f = 3$ light quarks, we have

$$\langle N|\alpha_s G^a_{\mu\nu}G^{a\,\mu\nu}|N\rangle = \frac{8\pi}{9}\,m_N\left[\frac{1}{m_N}\langle N|m_u\overline{u}u + m_d\overline{d}d + m_s\overline{s}s|N\rangle - 1\right] \equiv \frac{8\pi}{9}\,m_N\left[(f_u+f_d+f_s)-1\right]\,. \tag{48}$$

Recent Lattice QCD updates of the calculation for the strange quark matrix element has $f_u + f_d + f_s = 0.085^{+0.022}_{-0.014}$ [80]. In our numerical calculation, we will use $\langle N|\alpha_s G^a_{\mu\nu}G^{a\,\mu\nu}|N\rangle \approx -2.56\,m_N$.

The formula of the scattering cross section is then calculated to be

$$\sigma^{\rm SI}_{XN} \,=\, \frac{\kappa^2\, m_N^4}{4\pi\, \Lambda_1^4\, (m_N + M_X)^2}\,, \tag{49}$$

with $\kappa = \frac{2}{9}(f_u + f_d + f_s - 1) \approx -0.20$.

For the second operator, $\mathcal{O}_2^{\rm cRayleigh}$, we need to know the matrix element of $G\widetilde{G}$ inside a nucleon. This matrix element is related to the anomalous divergence of the iso-singlet axial current operator by

$$\sum_{i=1,\cdots,n_f} \partial^\mu(\bar{\psi}_i\gamma_\mu\gamma_5\psi_i) \,=\, \frac{n_f}{4\pi}\alpha_s\, G^a_{\mu\nu}\widetilde{G}^{a\,\mu\nu} \,+\, \sum_{i=1,\cdots,n_f} 2i\, m_i\bar{\psi}_i\gamma_5\psi_i\,. \tag{50}$$

In the large-N_c and chiral limit and using the relation $\langle N|\bar{u}i\gamma_5 u + \bar{d}i\gamma_5 d + \bar{s}i\gamma_5 s|N\rangle = 0$, one finds [81–83]

$$\langle p|\frac{\alpha_s}{8\pi}G^a_{\mu\nu}\widetilde{G}^{a\,\mu\nu}|p\rangle = 389\,{\rm MeV} \equiv \eta_p m_p\,, \quad \langle n|\frac{\alpha_s}{8\pi}G^a_{\mu\nu}\widetilde{G}^{a\,\mu\nu}|n\rangle = -2\,{\rm MeV} \equiv \eta_n m_n\,, \tag{51}$$

where the dimensionless parameters are $\eta_p \approx 0.41$ and $\eta_n \approx -0.0021$ (the instanton calculation in Ref. [84] obtained dramatically different numbers). The large difference between η_p and η_n indicates a large isospin violation for pseudo-scalar coupling to nucleons. One can then use the matrix elements to translate $\mathcal{O}_2$ to the interaction between dark matter and nucleons, giving

$$\frac{2i\,\eta_N\, m_N}{\Lambda_2^2}(XX - X^\dagger X^\dagger)\,\overline{N}i\gamma_5 N\,. \tag{52}$$

In the non-relativistic limit, one has $\overline{N}i\gamma_5 N \approx 2i\vec{q}\cdot\vec{s}$ with $\vec{q}$ as the exchange momentum of the scattering process and $\vec{s}$ as the spin of a nucleon. So, for this interaction, we have both spin-dependent and momentum-suppressed scattering. The spin-dependent differential scattering cross section is

$$\frac{d\sigma^{\rm SD}_{X\,N}}{d\cos\theta} = \frac{\eta_N^2\, m_N^2}{2\,\pi\,\Lambda_2^4}\frac{q^2}{(m_N + M_X)^2}\,. \tag{53}$$

M_X (GeV)	Λ_1 (GeV)	Λ_2 (GeV)
1	130	170
10	120	180
100	120	180
200	110	160
400	90	130

Table 4: The collider constraints on the cutoff of the effective operators for different dark matter masses at 90% CL. The mono-jet analysis with $E_T^{\rm miss} > 500$ GeV from the CMS collaboration in Ref. [89] has been used.

For $M_X \sim 100$ GeV, a small cutoff scale of $\Lambda_2 \sim 100$ GeV, and a typical exchange momentum of $q \sim \mu_{XA}\, v \sim 100$ MeV, the spin-dependent scattering cross section of dark matter off a proton is 10^{-7} pb. This is far below the current direct detection experimental bound [85, 86].

Collider Constraints

For the two operators considered here, the universal signature at the LHC is that of a mono-jet plus missing transverse energy [87, 88]. For fermion dark matter coupling to two gluons, both the CMS [89] and ATLAS [90] collaborations have imposed limits on the cutoffs of the effective operators. To estimate the constraints on our scalar dark matter case, we use `FeynRules` [91] to generate a model file for `MadGraph` [92]. We then use `Pythia` [93] to shower and hadronize the parton-level events. Finally, we use `PGS` [94] to cluster hadrons into jets and simulate detector effects.

Following the same analysis procedure from the CMS collaboration in Ref. [89] at 8 TeV and with 19.7 fb^{-1} luminosity, we have found that imposing a cut on the missing transverse energy $E_T^{\rm miss} > 500$ GeV (or requiring less than 164 signal events) provides the strongest bounds for a wide range of dark matter masses. We show the constraints on the cutoffs of the effective operators in Table 4 for different dark matter masses. The constraints stay constant for light dark matter below 100 GeV and become weaker as one increases the dark matter mass beyond around 100 GeV. One can also see that for heavier dark matter beyond 200 GeV, the constraints become much weaker such that the cutoff is even below M_X, which indicates a breakdown of the perturbative description of the effective field theory.

3.3 Simplified UV-Completion Models

As already can be seen from Table 4, the constraints on the cutoffs of the contact operators from the mono-jet searches are not that stringent. For a 100 GeV dark matter particle, the constrained cutoff is just comparable to the dark matter mass. This calls for UV-completed models to reduce the uncertainties from an effective field theory description. In this section, we consider several classes of models to illustrate that collider signatures beyond the mono-jet may provide a more sensitive probe of dark matter chromo-Rayleigh interactions.

Introducing only X and its allowed couplings to the SM under the dark $\mathcal{Z}_2$ symmetry, the renormalization interactions are

$$\mathcal{L}_X \supset \partial_\mu X^\dagger \partial^\mu X - M_X'^2 X^\dagger X - \frac{\lambda_X}{4}(X^\dagger X)^2 - \lambda_{HX} X^\dagger X \, H^\dagger H \,, \tag{54}$$

where H is the SM Higgs doublet and we choose a positive quartic coupling of $\lambda_X > 0$. After electroweak symmetry breaking, X receives a contribution to its mass from the Higgs mechanism and is assumed to have a positive mass of $M_X^2 = M_X'^2 + v^2 \lambda_{HX}/2$, where v is the Higgs vacuum expectation value. Similar to the Higgs-portal dark matter models, the SM Higgs boson can decay into two dark matter particles for $M_X < M_h/2$. At 7 TeV and 8 TeV LHC, the searches for the Higgs boson invisible decays have constrained the invisible branching ratio to be less than 0.28 at 95% C.L. [95, 96], which can be translated into a bound on λ_{HX} as $\lambda_{HX} \lesssim 0.015$ for a light dark matter mass.

Given the effective coupling of the Higgs boson with two gluons in the SM, one automatically generates the dark matter-gluon coupling of Eq. (43). The additional introduction of a color-neutral pseudo-scalar, which appears for instance in two-Higgs-doublet-portal dark matter models, can generate the dark matter chromo-Rayleigh interaction of Eq. (44) (see e.g. Refs. [72, 73, 97, 98]).

As the existing search strategies for the Higgs-portal and pseudo-scalar-portal dark matter cover this class of UV-completions [95], we consider two other ways to UV-complete the chromo-Rayleigh dark matter interactions with more novel collider signatures.

QCD-charged Particle Mediation for $\mathcal{O}_1^{\mathrm{cRayleigh}}$

In this subsection, we examine a class of models with additional QCD-charged scalars to generate the effective chromo-Rayleigh interaction of $\mathcal{O}_1^{\mathrm{cRayleigh}}$. For specificity's sake, we introduce a real color-octet and electroweak-singlet scalar, [2] G_H^a with $a = 1, \cdots, 8$ and a mass of M_{G_H}, which, for example, appears in the Renormalizable Coloron Model (ReCoM) [99, 100]. The scalar Lagrangian for this theory is

$$\begin{aligned}\mathcal{L}_{G_H} \supset \frac{1}{2} D_\mu G_H^a D^\mu G_H^a - \frac{1}{2} M'^2_{G_H} G_H^a G_H^a - \frac{\lambda_G}{8}(G_H^a G_H^a)^2 - \frac{\lambda_{HG}}{2} G_H^a G_H^a H^\dagger H \\ - \frac{\lambda_{XG}}{2} G_H^a G_H^a X^\dagger X + \mathcal{L}_{\mathrm{even(odd)}}\,, \end{aligned} \tag{55}$$

where D_μ is the covariant derivative. $\mathcal{L}_{\mathrm{even(odd)}}$ is specific to the identification of G_H as even (odd) under the dark $\mathcal{Z}_2$ symmetry,

$$\mathcal{L}_{\mathrm{even}} = -\mu_G d^{abc} G_H^a G_H^b G_H^c\,, \tag{56}$$

$$\mathcal{L}_{\mathrm{odd}} = -\eta_{XG} d^{abc} G_H^a G_H^b G_H^c (X + X^\dagger)\,, \tag{57}$$

with d^{abc} the totally symmetric $SU(3)_{\mathrm{QCD}}$ tensor. The scalar octet G_H also receives a contribution to its mass from the Higgs mechanism, which is $M^2_{G_H} = M'^2_{G_H} + v^2 \lambda_{HG}/2$. We note that a large value of $\lambda_{HG}/M^2_{G_H}$ can modify the effective interaction of the Higgs boson coupling to two gluons [101–105]. Using the limits from the LHC Run 1 [106], the limit is $|M_{G_H}/\sqrt{\lambda_{GH}}| \gtrsim 1.9\, v$.

At one-loop level, the effective operator can be generated through the diagrams in Fig. 12 and has

---

[2] A similar analysis can be performed for other QCD representations.

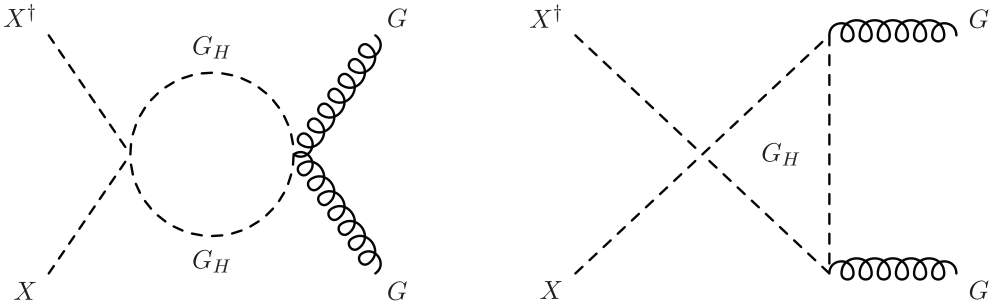

Figure 12: Representative loop diagrams for generating $\mathcal{O}_1^{\text{cRayleigh}}$ via colored scalar loops.

the following calculated form

$$F(\tau)\,\frac{\lambda_{XG}}{8\,M_{G_H}^2}\,\frac{\alpha_s}{4\pi}X^\dagger X\,G^a_{\mu\nu}G^{a\,\mu\nu}\,, \tag{58}$$

where the form factor $F(\tau)$, with $\tau = (p_1+p_2)^2/(4M_{G_H}^2)$, is one in the limit $\tau \to 0$. Here, p_1 and p_2 are the gluon momenta pointing to the vertex. In the limit that $M_{G_H} \gg M_X$ and with small gluon momenta much below $|p_1 + p_2|$, one can match the colored particle mass to the effective operator cutoff defined in Eq. (43) to obtain

$$\Lambda_1^2 = \frac{8}{\lambda_{XG}}\,M_{G_H}^2\,. \tag{59}$$

For this class of UV-complete models, one can also work out the collider constraints. Depending on whether the color-octet is odd or even under the dark matter $\mathcal{Z}_2$, one has different decay channels for G_H^a. If it is $\mathcal{Z}_2$-even, the cubic self-interaction of $\mathcal{L}_{\text{even}}$ can make G_H unstable. This introduces the decay of G_H into two gluons at one loop with a width of [99, 107]

$$\Gamma(G_H \to gg) = \frac{15\,\alpha_s^2\,\mu_G^2}{128\,\pi^3\,M_{G_H}}\left(\frac{\pi^2}{9}-1\right)^2\,. \tag{60}$$

$\mathcal{Z}_2$-even G_H can be pair-produced at the LHC from their QCD interactions, which then decay into paired dijets. Following the same reinterpretation of the experimental data as in Ref. [108], we find that the current searches for paired dijet resonances at the 8 TeV LHC have set a constraint on its mass of [109]

$$M_{G_H} \gtrsim 520 \text{ GeV}\,, \qquad\qquad \text{for } \mathcal{Z}_2\text{-even } G_H\,, \tag{61}$$

where we have only included the QCD productions.

If G_H is $\mathcal{Z}_2$-odd, the dark matter particle X has to appear in the G_H decay products. The operators mediating G_H decaying to X first occur at the dimension six level and contain the following two parity-conserving operators

$$\frac{D_\mu G^a_H \partial_\nu X\, G^{a\,\mu\nu}}{\Lambda_1'^2} + \text{h.c.}\,, \qquad\qquad \frac{G^a_H X \widetilde{H}\overline{Q}_L t^a t_R}{\Lambda_1''^2} + \text{h.c.}\,. \tag{62}$$

Here, t^a with $a = 1, 2, \cdots, 8$ are the $SU(3)_{\rm QCD}$ generators. For the second operator, we have only included the top quark by assuming that the coupling is proportional to the quark mass. Using the equation of motion, $D_\mu G^{a\,\mu\nu} = -g_s\, \bar{q}\gamma^\nu t^a q$, the first decay-inducing operator becomes

$$\frac{g_s}{\Lambda_1'^2}\, G^a_H \partial_\nu X\, \bar{q}\gamma^\nu t^a q\,. \tag{63}$$

As a result, the decay channels of the colored state G_H are mainly $G_H \to X\bar{q}q$. For each flavor, the three-body decay width is calculated to be

$$\begin{aligned} \Gamma(G_H \to X\bar{q}q) = & \frac{g_s^2}{3\cdot 2^9\,\pi^3 \Lambda_1'^4} \\ \times \int_{4m_q^2}^{(M_{G_H}-M_X)^2} ds & \left(1+\frac{2m_q^2}{s}\right)\left(1-\frac{4m_q^2}{s}\right)^{1/2} \left[\frac{M_X^4 + (M_{G_H}^2 - s)^2 - 2M_X^2(M_{G_H}^2 + s)}{M_{G_H}^2}\right]^{3/2}\,. \end{aligned} \tag{64}$$

Choosing $g_s = 1.1$, $M_{G_H} = 500$ GeV, $M_X = 10$ GeV, $\Lambda_1' = 1$ TeV, and neglecting the quark mass, $\Gamma = 0.0002$ GeV for each flavor and G_H can decay promptly for collider studies.

From the above assumptions, the collider signature for pair-produced $\mathcal{Z}_2$-odd G_H contains $4j + E_T^{\rm miss}$, $t\bar{t} + 2j + E_T^{\rm miss}$ and $2t + 2\bar{t} + E_T^{\rm miss}$. Generically, the top-quark rich final state can be easily searched for at the LHC. So, we concentrate on the first operator in Eq. (62) and derivate a more conservative bound based mainly on the $4j + E_T^{\rm miss}$ final state. Following the analysis in Ref. [110] at the 8 TeV LHC with 19.5 fb^{-1}, we find that the set of cuts with $300 < \not{H}_T < 450$ GeV, $800 < H_T < 1000$ GeV, $3 \leq N_{\rm jets} \leq 5$ with $p_T(j) > 50$ GeV and $|\eta| < 2.5$ provide the best constraint. For $M_{G_H} = 600$ GeV and $M_X = 10$ GeV, we have $\text{Br}(G_H \to 2j + X) = 97.5\%$ and $\text{Br}(G_H \to t\bar{t} + X) = 2.5\%$. The production cross section at the 8 TeV LHC after this set of cuts is approximately $1.9\,\text{fb} \times K$ with a K-factor of 1.8 [111]. This amounts to a total of 65.4 events at 19.5 fb^{-1}, which is very close to the allowed number of signal events (65.6 from Ref. [110]) at 90% C.L. So, for a large mass splitting between the color-octet state G_H and the dark matter X, the current LHC bound is

$$M_{G_H} \gtrsim 600 \text{ GeV}\,, \qquad\qquad \text{for } \mathcal{Z}_2\text{-odd } G_H\,. \tag{65}$$

Independent of how G_H decays, we have set a constraint on the G_H mass to be above 500-600 GeV. Using the relation in Eq. (59), this constraint translates to a limit on the effective cutoff scale of $\Lambda_1 \gtrsim 1.5 - 1.7$ TeV for $\lambda_{XG} = 1$, which is far more stringent than the limits in Table 4 set from the mono-jet search. To compare with the limits from direct detection experiments, we show the reinterpreted collider limits using $\Lambda_1 > 1.7$ TeV for the first chromo-Rayleigh interaction in the left panel of Fig. 18. The left panel of Fig. 18 shows a comparison between the limits on the scattering cross section $\sigma_{XN}^{\rm SI}$ obtained from direct detection, monojet, and $4j + E_T^{\rm miss}$ searches.

QCD-charged Particle Mediation for $\mathcal{O}_2^{\rm cRayleigh}$

To UV-complete the operator $\mathcal{O}_2^{\rm cRayleigh}$, we introduce a pair of vector-like fermions, which appear in a wide range of new physics models like the Kaluza-Klein fermions in the universal extra dimensional model [112] or the top partners in the little Higgs model with T-parity [113]. We fix the quantum numbers of these fermions to be the same as u_R for later convenience. The Lagrangian for this

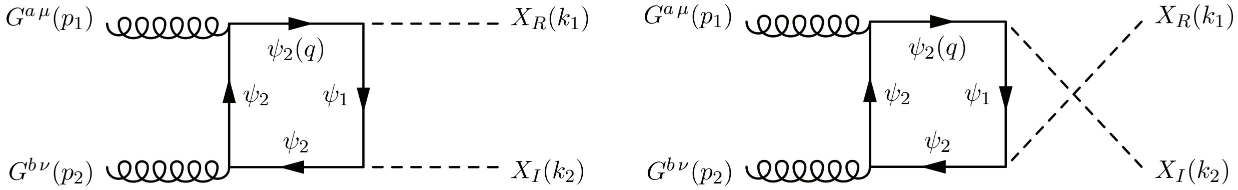

Figure 13: Representative loop diagrams for generating $\mathcal{O}_2^{\rm cRayleigh}$ via colored fermion loop.

sector is then

$$\begin{aligned}\mathcal{L}_\psi \supset\, & \overline{\psi}_1 \left(i\not{D} - m_{\psi_1}\right) \psi_1 + \overline{\psi}_2 \left(i\not{D} - m_{\psi_2}\right) \psi_2 - \left(\lambda_{\psi_{1(2)}} \overline{Q}_L \widetilde{H} \psi_{1(2)} + \text{h.c.}\right) \\ & - y_1 \left(X + X^\dagger\right) \left(\overline{\psi}_1 \psi_2 + \overline{\psi}_2 \psi_1\right) - y_2 \left(X - X^\dagger\right) \left(\overline{\psi}_1 \gamma_5 \psi_2 + \overline{\psi}_2 \gamma_5 \psi_1\right) \,. \end{aligned} \tag{66}$$

To conserve the dark $\mathcal{Z}_2$ symmetry, one of the fermion triplets must be $\mathcal{Z}_2$-odd while the other is $\mathcal{Z}_2$-even. Only the $\mathcal{Z}_2$-even fermion has an allowed Yukawa coupling with the SM Higgs boson. Using the freedom of field redefinitions of ψ_1 and ψ_2, one can keep the first coupling, y_1, to be a real number while the second coupling, y_2, may in general be complex. We choose y_2 to be a real number to satisfy CP symmetry. In terms of the components, $X = (X_R + i\,X_I)/\sqrt{2}$, we have the interactions

$$\mathcal{L} \supset -\sqrt{2}\, y_1\, X_R \left(\overline{\psi}_1 \psi_2 + \overline{\psi}_2 \psi_1\right) - \sqrt{2}\, i\, X_I \left(y_2\, \overline{\psi}_1 \gamma_5 \psi_2 + y_2\, \overline{\psi}_2 \gamma_5 \psi_1\right). \tag{67}$$

To preserve C and P, one has X_R to be C-even and P-even, and X_I to be C-even and P-odd. In terms of X_R and X_I, we have the effective operator

$$\mathcal{O}_2^{\rm cRayleigh} = -\frac{\alpha_s}{2\pi\Lambda_2^2} X_R X_I G^a_{\mu\nu} \widetilde{G}^{a\,\mu\nu} \,, \tag{68}$$

which conserves both C and P.

At one-loop level, one has the box diagrams in Fig. 13 to generate the effective operator $\mathcal{O}_2^{\rm cRayleigh}$. In the heavy particle limit with $m_{\psi_1}, m_{\psi_2} \gg M_{X_R}, M_{X_I}$, we have the matching condition (see

Appendix A.1 for a more detailed calculation)

$$\Lambda_2^2 = \frac{2\, m_{\psi_1} m_{\psi_2}}{|y_1 y_2|} \,. \tag{69}$$

For this specific UV-completion model, the first chromo-Rayleigh interaction can also be generated, since it does not break any discrete symmetries.

If $\mathrm{Im}(y_1 y_2) \neq 0$, the Lagrangian in Eq. (67) is P-conserving but C-breaking, so CP is also broken. [3] The lowest dimensional effective operator that is C-odd and P-even is at dimension-10, for instance $X_R X_I\, d_{abc}(D_\mu G^a_{\alpha\beta})(D_\nu G^{b\,\nu\alpha})\widetilde{G}^{c\,\beta\mu}$, further suppressed by powers of the cutoff scale. If parity was broken, lower-dimensional operators like $X_R X_I G^a_{\mu\nu} G^{a\,\mu\nu}$ could be generated with a stringent bound from the neutron electric dipole moment.

As mentioned before, in order to conserve the dark $\mathcal{Z}_2$ symmetry the two fields, ψ_1 and ψ_2, should have opposite dark parity. Fixing the mass relation $m_{\psi_2} > m_{\psi_1}$, we have two cases. The case A has $\mathcal{Z}_2$-even ψ_1 and $\mathcal{Z}_2$-odd ψ_2 and the case B has $\mathcal{Z}_2$-even ψ_2 and $\mathcal{Z}_2$-odd ψ_1. For both cases, we introduce the following dimension-5 operator to mediate the $\mathcal{Z}_2$-even particle decaying into two jets,

$$\frac{g_s^2}{4\pi\, \Lambda_2'} \bar{\psi}_{i\,L} \sigma^{\mu\nu} t^a u_R\, \widetilde{G}_a^{\mu\nu} \,. \tag{70}$$

Here, $i = 1(2)$ for case A(B). As a result of this decay mode, the unstable particle ψ_i behaves as a dijet resonance at colliders. One could also consider other potential decay channels by introducing the electroweak dipole moment operator, which has a clearer signature at colliders. The Yukawa operator with a coefficient, λ_{ψ_i}, in Eq. (66) can also mediate the $\mathcal{Z}_2$-even ψ_i decaying to one up quark plus Z or h. The constraint on the mass of $\mathcal{Z}_2$-even ψ_i is above between 720 GeV and 920 GeV for different branching fractions [115]. In our study, we will assume a negligible value of λ_{ψ_i} and concentrate on the more challenging fully-hadronic channel.

---

[3] For a complex y_2 with CP-violating interactions, one may wonder about generating the Weinberg operator [114], $f_{abc} G^a_{\mu\rho} G^{b\,\rho}_{\nu} \widetilde{G}^{c\,\mu\nu}$. We note that the P conservation forbids the generation of the effective Weinberg operator.

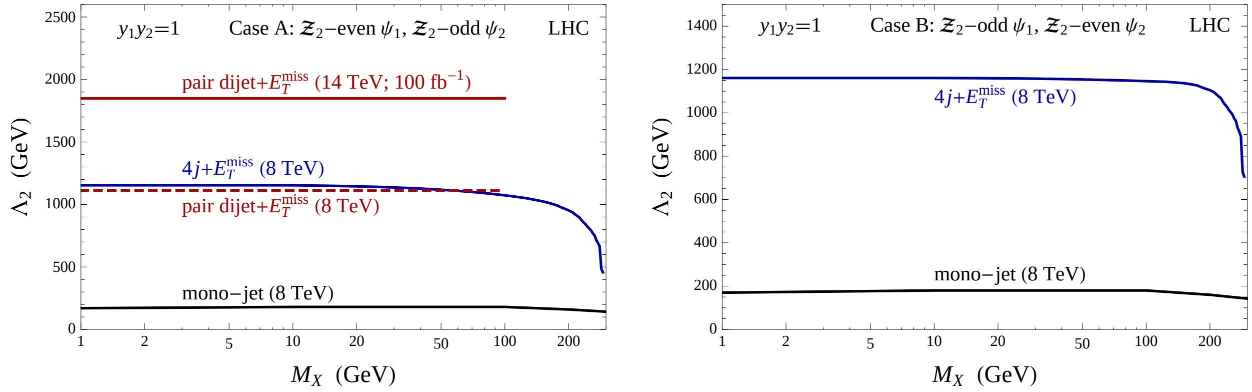

Figure 14: **Left panel:** constraints on the cutoff of the effective operator $\mathcal{O}_2^{\rm cRayleigh}$ for case A with $\mathcal{Z}_2$-even ψ_1 and $\mathcal{Z}_2$-odd ψ_2. **Right panel:** constraints for case B with $\mathcal{Z}_2$-odd ψ_1 and $\mathcal{Z}_2$-even ψ_2.

For case A with a $\mathcal{Z}_2$-even ψ_1, the collider signature of ψ_1 is pair-produced dijet resonances. The searches at the 8 TeV LHC have set a constraint on its mass [109] as $m_{\psi_1} \gtrsim 500$ GeV. Although the signature is interesting by itself, the discovery of this dijet resonance can not prove that dark matter has been produced at colliders. For the $\mathcal{Z}_2$-odd ψ_2 particle, the decay channel is $\psi_2 \to X + \psi_1 \to X + 2j$. Depending on the mass splitting of ψ_1 and ψ_2, one has ψ_1 to be off-shell for $m_{\psi_2} - m_{\psi_1} < M_X$ and on-shell for $m_{\psi_2} - m_{\psi_1} > M_X$. For the off-shell intermediate ψ_1 case, this signature is very similar to the SUSY squark searches with a heavy gluino [110], except with a larger production cross section than a single flavor squark. For dark matter mass $M_X \lesssim 100$ GeV, the constraint on the ψ_2 mass is $m_{\psi_2} \gtrsim 850$ GeV, assuming that the signal acceptance is similar to the squark one [110]. For a heavy dark matter mass close to 290 GeV, the constraint becomes weaker and is $m_{\psi_2} \gtrsim 500$ GeV. Using the conversion formula in Eq. (69), we show the constraints from $4j + E_T^{\rm miss}$ on the effective cutoff for different dark matter masses in the left panel of Fig. 14, by setting $m_{\psi_1} = m_{\psi_2} - M_X$ and $y_1 y_2 = 1$.

For the on-shell ψ_1 case, the signature is more interesting with a pair of dijet resonances plus a large $E_T^{\rm miss}$. The relevant production Feynman diagram is shown in the left panel of Fig. 15. We perform a detailed collider study for this interesting signature in Section 3.3. As a comparison, in the left panel of Fig. 14 we show the interpreted constrains for $M_X \lesssim 100$ GeV on the matched cutoff from Eq. (69) for both the 8 TeV LHC with 19.5 fb^{-1} and the 14 TeV LHC with 100 fb^{-1}.

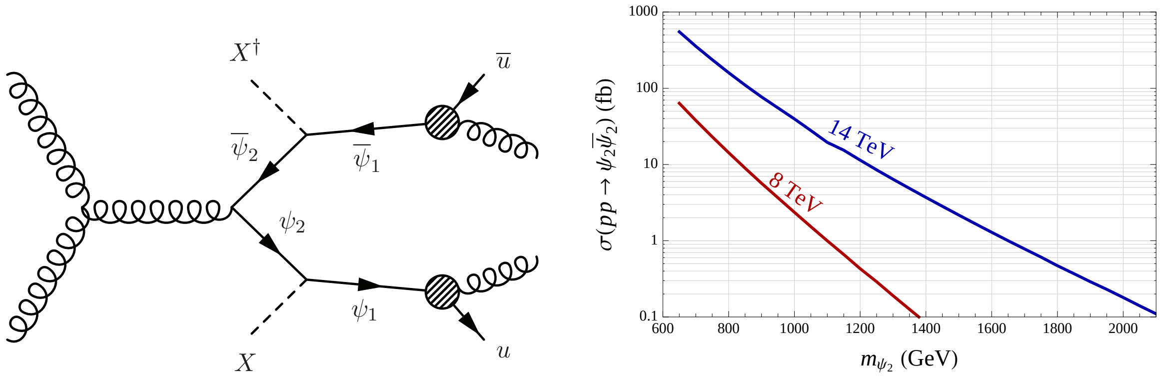

Figure 15: **Left panel:** the representive Feynman diagram for the process of $pp \to \psi_2\bar{\psi}_2 \to X+\psi_1+X^\dagger+\bar{\psi}_1 \to XX^\dagger+4j$. **Right panel:** the tree-level production cross sections of $pp \to \psi_2\bar{\psi}_2$.

One can see a clear improvement on constraining this effective chromo-Rayleigh interaction from a dedicated search beyond the simple mono-jet signature.

For case B with $\mathcal{Z}_2$-odd ψ_1 and $\mathcal{Z}_2$-even ψ_2, the searches for pair-produced dijet resonances provide a constraint of $m_{\psi_2} \gtrsim 500$ GeV. The decay of ψ_1 needs to go through an off-shell ψ_2 via $\psi_1 \to X + \psi_2^* \to X + 2j$. Applying the SUSY squark searches with a heavy gluino [110], the constraint on the ψ_1 mass is $m_{\psi_2} \geq m_{\psi_1} \gtrsim 850$ GeV for $M_X \lesssim 100$ GeV and $m_{\psi_1} \gtrsim 500$ GeV for M_X close to 290 GeV. In the right panel of Fig. 14, we show the reinterpreted constraints on the effective cutoff for $y_1 y_2 = 1$.

Pair-produced Dijet Resonances plus E_T^{miss}

In this section, we perform a detailed collider study for the process of $pp \to \psi_2\bar{\psi}_2 \to X + \psi_1 + X^\dagger + \bar{\psi}_1 \to XX^\dagger + 4j$. The collider signature is pair-produced dijet resonances plus missing transverse energy. In the left panel of Fig. 15, we show the Feynman diagram for this process. The QCD production cross sections for $\psi_2\bar{\psi}_2$ at the LHC are the same as vector-like $t'\bar{t}'$ [116]. We show the tree-level production cross sections, calculated using `MadGraph` [92], in the right panel of Fig. 15. In the following analysis, we will ignore the signal K-factor because we will use tree-level cross sections for backgrounds. [4]

---

[4] One might expect the overall significance in the later analysis to be increased by a factor of $\sim 1.2 - 1.3$ due to the inclusion of NLO effects.

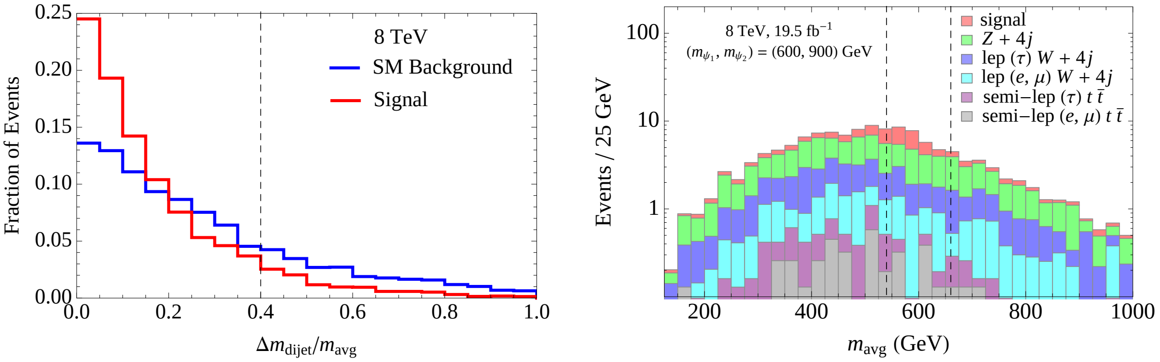

Figure 16: **Left panel:** the distributions of the fraction of events as a function of $\Delta m_{\rm dijet}/m_{\rm avg}$ for the signal of $(m_{\psi_1}, m_{\psi_2}) = (600, 900)$ GeV and the summed background. **Right panel:** the averaged dijet invariant mass distributions for the signal and various backgrounds, after the cut of $\Delta m_{\rm dijet}/m_{\rm avg} < 0.4$.

The main SM background comes from $Z/W^{\pm} + n$ jets with $Z \to \nu\bar{\nu}$ and leptonic decays of $W^{\pm}$. After comparing the results from matching parton showers and matrix elements [117], we have found that the background of parton-level $Z/W^{\pm} + 4$ jets with $p_T(j) > 120$ GeV provides a good estimation of total $Z/W^{\pm} + n$ jets background for the 8 TeV LHC. Therefore, we use $Z/W^{\pm} + 4$ jets as an approximation to save simulation time. There also exist additional, sub-dominant semi-leptonic $t\bar{t}$ backgrounds, which will be kept in our analysis.

Starting from the 8 TeV LHC with 19.5 fb^{-1}, we choose the model point $(m_{\psi_1}, m_{\psi_2}) = (600, 900)$ GeV as a benchmark to optimize our cuts on kinematic variables. We choose the basic cuts on the jet and missing transverse momenta to be $p_T(j_i) > 140$ GeV and $E_T^{\rm miss} > 275$ GeV and required at least four jets satisfying the jet p_T cut in the final state. To reduce the $t\bar{t}$ and $W^{\pm}$+jets backgrounds, we also veto events containing a lepton with $p_T(\ell) > 20$ GeV. Since our signal has a pair of dijet resonances with the same mass, we choose the combination among three possible dijet pairs with the smallest dijet invariant mass difference, $\Delta m_{\rm dijet}$. To further reduce the SM background, we show the event fraction histogram distribution in terms of the variable $\Delta m_{\rm dijet}/m_{\rm avg}$ in the left panel of Fig. 16. Signal events prefer a smaller value of dijet invariant mass difference than background events. As a result, we impose a cut on this variable with $\Delta m_{\rm dijet}/m_{\rm avg} < 0.4$ to further increase the discovery sensitivity. In the right panel of Fig. 16, we show the averaged dijet invariant

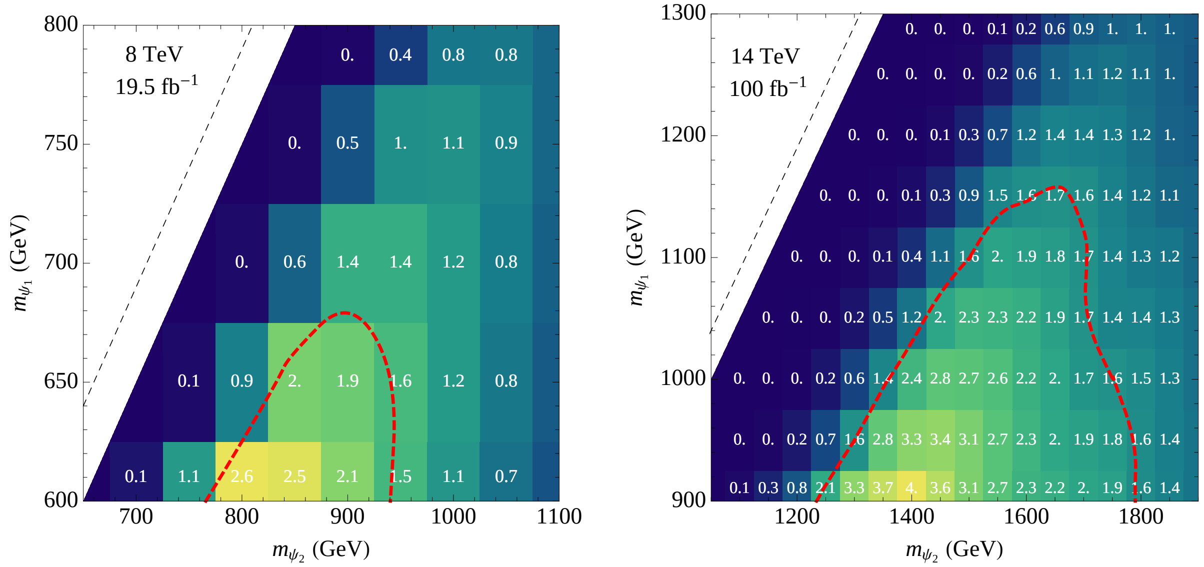

Figure 17: **Left panel:** the signal significance $S/\sqrt{B}$ for different model points with the cuts optimized for $(m_{\psi_1}, m_{\psi_2}) = (600, 900)$ GeV and $M_X = 10$ GeV at the 8 TeV LHC with 19.5 fb^{-1}. The red dashed line is the extrapolated 90% C.L. exclusion curve. The black dashed line has $m_{\psi_2} = m_{\psi_1} + M_X$. **Right panel:** the same as the left panel but for 14 TeV with 100 fb^{-1} and the set of cuts for the combined benchmark points $(m_{\psi_1}, m_{\psi_2}) = (900, 1800)$ GeV and $(900, 1500)$ GeV with $M_X = 10$ GeV.

mass distribution for the signal and backgrounds. Since the signal events mainly distribute around the ψ_1 particle mass, we also impose one additional cut with $|m_{\rm avg} - m_{\psi_1}| < 0.1\, m_{\psi_1}$ to further improve the sensitivity. With the above cuts, we show the values of $S/\sqrt{B}$ for different mass points in the left panel of Fig. 17. At 90% C.L., our simulated results show that the model point of $(m_{\psi_1}, m_{\psi_2}) = (650, 950)$ GeV can be covered, which corresponds to $\Lambda_2 \gtrsim 1.1$ TeV. Once again we see a dramatic improvement relative to the standard mono-jet signature.

At the 14 TeV LHC with 100 fb^{-1}, we choose two benchmark points with $M_X = 10$ GeV and $(m_{\psi_1}, m_{\psi_2}) = (900, 1800)$ $[(900, 1500)]$ GeV. To optimize the discovery sensitivity, we choose the following set of cuts: at least four jets with $p_T(j) > 200$ GeV; $E_T^{\rm miss} > 900$ $[600]$ GeV; $\Delta m_{\rm dijet}/m_{\rm avg} < 0.4$ $[0.3]$; $|m_{\rm avg} - m_{\psi_1}| < 0.1\, m_{\psi_1}$. The signal significances, $S/\sqrt{B}$, for different model points are shown in the right panel of Fig. 17, taking the larger $S/\sqrt{B}$ value from between the two benchmark points. We show the combined 90% C.L. exclusion contour in the red dashed line, which has the lower right region covered by the set of cuts for $(900, 1800)$ GeV and the upper right region by $(900, 1500)$ GeV. At 90% C.L., one can see that the model point of $(m_{\psi_1}, m_{\psi_2}) = (950, 1800)$ GeV can be excluded, which corresponds to $\Lambda_2 \gtrsim 1.8$ TeV.

3.4 Comparison to the Direct Detection Limits

To compare with the constraints from direct detection experiments, we show the interpreted dark matter-nucleon scattering cross sections from the LHC mono-jet, $4j + E_T^{\rm miss}$ and paired dijet$+E_T^{\rm miss}$ searches in Fig. 18. In the left panel, we show the spin-independent scattering cross section including the constraints from the LUX collaboration [89]. Compared to the direct detection limits, the constraints from the LHC are not strong for heavier dark matter masses, but are more stringent for a light dark matter mass below around 5 GeV. Compared to the limits from mono-jet searches, the $4j + E_T^{\rm miss}$ signature is definitely a more sensitive channel for constraining the spin-independent scattering cross section from the first chromo-Rayleigh interaction, $X^\dagger X G^a_{\mu\nu} G^{a\,\mu\nu}$.

In the right panel of Fig. 18, we show the interpreted collider constrains for the second operator, $i(XX - X^\dagger X^\dagger) G^a_{\mu\nu} \widetilde{G}^{a\,\mu\nu}$. Here, we only show the dark matter-proton scattering cross section, since it has a larger value than dark matter-neutron one for the same dark matter mass. For the interpreted limits from collider searches and because of the additional momentum suppression with $q \approx \mu_{XA} v$, we fix the dark matter velocity to be $v = 10^{-3}$ and choose a typical target nucleus mass $m_A = 100$ GeV in Eq. (53). Compared to the constraints from direct detection experiments, the collider searches obviously provide a more sensitive probe of this type of dark matter chromo-Rayleigh interactions.

3.5 Discussion

One advantage of introducing simplified models is that the relevant model is complete from the renormalizability point of view. There is no worry about trusting theoretical descriptions of the collider limits like in the effective operator approach. On the other hand, the simplified models typically contain more model parameters and make the comparison with the results from dark

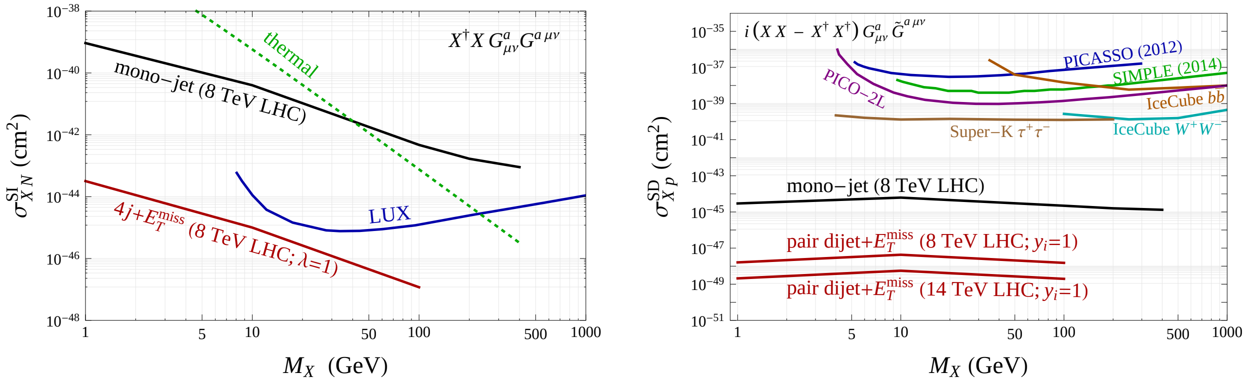

Figure 18: **Left panel:** the constraints on the dark matter spin-independent scattering cross sections from the LHC mono-jet [89] and multi-jet+$E_T^{\rm miss}$ [110] searches at the 8 TeV LHC with ~ 20 fb^{-1} and the LUX direct detection experiment [118]. **Right panel:** the same as the left one but for spin-dependent dark matter-proton scattering cross sections from the LHC, SIMPLE [119], PICASSO [120], PICO-2L [121], IceCube [122] and Super-K [123]. The scattering cross section is suppressed by both the spin-dependent scattering and the exchanging momenta.

matter direct or indirect detection less model-independent. For the simplified models studied here, the collider signatures highly depend on how the QCD charged particles decay. For the first operator, the color-octet scalar can decay into two gluons or two quarks plus the dark matter particle. For the second operator, the two color-triplet fermions could have many other possible decay channels beyond the ones in this chapter. For instance, one could replace the operator in Eq. (70) by $\bar{\psi}_{i\,L}\sigma^{\mu\nu}u_R\widetilde{B}^{\mu\nu}$, which can lead to the decay of $\psi \to u+\gamma/Z$. The final collider signature could be $2j + 2\gamma(Z) + E_T^{\rm miss}$ with or without a pair of $j+\gamma(Z)$ resonances. To cover the majority of simplified models for dark matter chromo-Rayleigh interactions, one should search for a wide range of potential signatures.

In conclusion, we have studied simplified models to UV-complete the chromo-Rayleigh interactions of dark matter. For the first operator, a new color-octet scalar particle could be in reach of the LHC. It may decay into just two jets or two jets plus missing transverse energy. The 8 TeV LHC can already constrain this color-octet scalar mass to be above 500-600 GeV, which can be translated into a constraint on the cutoff of the effective operator to be above 1.5-1.7 TeV. For the second operator, two QCD-charged fermions are predicted for the simplified model in this chapter.

A collider study of pair-produced dijet resonances plus missing energy at the 14 TeV LHC can constrain the geometric mean of the two fermion masses above around 800 GeV, which can be interpreted as a bound on the effective operator cutoff above around 1.8 TeV.

4 A Strongly Coupled Chiral Gauge Theory

In December 2015, both the CMS and ATLAS experiments at the LHC reported a significant excess of events at 750 GeV in the diphoton channel [124, 125]. The relatively large production cross section ($\sigma \sim 4.6$ fb) likely required strong dynamics to explain, and the possibility that this was the first signature of a SM-neutral pion from some new strongly interacting sector was explored in great detail. However, new data recorded in 2016 contained no such excess above the expected SM background [126, 127]. The observed events for 2015 and 2016 from the ATLAS collaboration is shown in Fig. 19. For a review of the vanishing 750 GeV excess including a comprehensive list of references, see Ref. [128].

This one-time 750 GeV resonance inspired a great deal of theoretical effort examining the possibility of new strong dynamics existing at the TeV scale. In this chapter, we explore the ramifications of extending the SM to include a sector containing a new confining $SU(N_b)$ gauge symmetry. We find that in order to combine such a sector with several other proposed extensions of the SM, the introduction of an additional gauge symmetry is required, under which the new fermionic fields are chiral. To examine the phenomenological ramifications of such a theory, we introduce a new sector, charged under an $SU(N_b) \times U(1)'$ gauge symmetry, with the new fields imbedded in complete $SU(5)_{\text{GUT}}$ representations. The main body of this chapter has been reproduced from Ref. [129].

4.1 Introduction

One of the simplest extensions of BSM physics is the introduction of new fermions in vector-like representations of the SM gauge group, which automatically satisfy the gauge anomaly cancellation conditions discussed in Sec. 1.1. The dynamics of the new fermions are drastically different if they are charged under a new confining non-Abelian gauge group. Condensation spontaneously breaks the chiral symmetry of the fermions and massless Nambu-Goldstone boson (NGB) modes manifest which potentially couple to SM gauge bosons via triangle anomalies [130]. The fermions must have an explicitly chiral symmetry breaking mass m in order to lift the NGB's masses and avoid

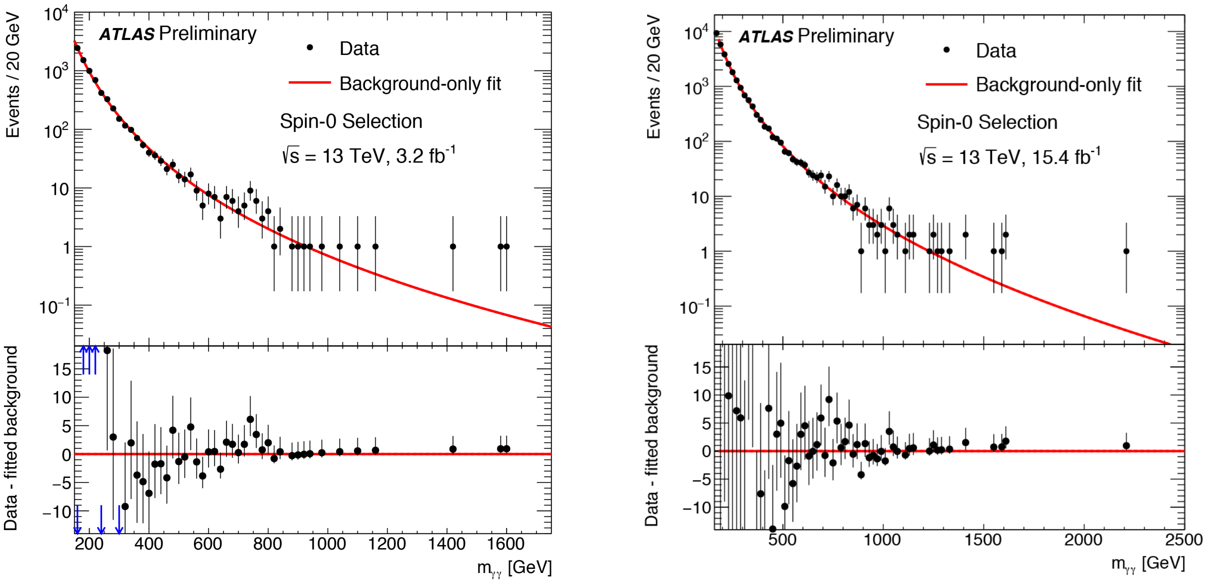

Figure 19: Diphoton events recorded by the ATLAS experiment in 2015 (left) and combined results from 2015 and 2016 (right). Images are reproduced from Refs. [125] and [127], respectively.

additional massless degrees of freedom.

If the confinement scale Λ is in the range probed by the LHC, the NGB modes are accessible only if $m \lesssim \Lambda$. If the fermion masses are heavy, $m \gg \Lambda$, the lightest degree of freedom will instead be a spin-zero glueball that is nearly decoupled from the SM even if the fermions are charged under the SM gauge groups. Although technically natural, there is no *a* priori reason to expect the fermion masses to be lighter than the confinement scale. This problem is even more acute in models that place the constituent fermions in representations of a Grand Unified Theory (GUT) gauge group. The fermion masses are then generally set by a combination of vector-like mass terms and couplings to the GUT-breaking sector as

$$-M\,\bar{\psi}\,\psi - y\,\bar{\psi}\,\Phi_{24}\,\psi\,, \tag{71}$$

with $\langle\Phi_{24}\rangle \sim \mathcal{O}(M_{\mathrm{GUT}})$. In order for the resulting fermion masses to be close to but below the confinement scale, these two contributions must either have very small coefficients, or cancel out very finely to arrange a TeV-scale mass. While this is true in GUT models, it can also be the case for example in models of right-handed neutrinos. Technical naturalness protects the fermion masses from large loop corrections, but they can still receive large contributions to their masses when coupled to any singlet which acquires a large VEV.

The SM QCD sector evades this puzzle and indeed has non-decoupled pions close to the scale of strong dynamics. The puzzle is resolved through a combination of factors: small Yukawa couplings, but also a chiral gauge symmetry structure. It is therefore plausible that the new strong dynamics sector operates in a similar way. Since the fermions cannot be chiral under the GUT gauge group and be consistent with constraints on a chiral fourth generation [131–135], they can only be chiral under a new gauge group. For simplicity, we study the case where this new gauge group is a $U(1)'$ Abelian group. If the fermions are charged under this additional gauge group, then the terms of Eq. (71) are forbidden without additional insertions of a $U(1)'$-breaking VEV. Given a $U(1)'$-breaking sector near the scale Λ, the lightest composite particles will also be near Λ and will have large couplings to the SM. While there is still a coincidence of scales, it is far less acute. The fermion masses will no longer be near the GUT scale, but rather the scale at which the hierarchy problem is ultimately resolved.

In this chapter, we consider a model with an $SU(N_b)$ (big-color) confining gauge group and a $U(1)'$ Abelian group. We also take the fermions in the big-color sector (big-quarks) to transform as fundamentals of an $SU(5)_{\text{GUT}}$ symmetry. [5] Their charge under the Abelian group is chiral, such that the big-quark masses will be forbidden without additional structure. To give the big-quarks mass, we introduce a scalar φ charged under $U(1)'$ that couples to the big-quarks. It develops a VEV through its coupling to the confining sector, lifting the big-pion masses to be close to, but below, the mass of φ. In this way, we construct a chiral model that not only has an experimentally-accessible spectrum, but also that alleviates the tension caused by the coincidence of scales.

The addition of the Abelian gauge group with chiral structure has important and interesting phenomenological consequences. In particular, there is an additional massive Z' gauge boson coupling to the big-quarks and mixing with the SM γ and Z. This opens new decay modes for the big-pions,

---

[5] It is challenging to unify all of $SU(5)_{\text{GUT}}$, $SU(N_b)$, and $U(1)'$ together due to anomaly cancellation. Given the SM fermion charges and gauge coupling running, $SU(5)_{\text{GUT}}$ unification has additional motivation from experimental data.

	$SU(N_b)$	$SU(5)_{\text{GUT}}$	$U(1)'$
$\left(\psi^{\text{T}}_{1,L},\ \psi^{\text{D}}_{1,L}\right)$	N_b	5	q_1
$\left(\psi^{\text{T}}_{1,R},\ \psi^{\text{D}}_{1,R}\right)$	N_b	5	q_2
$\left(\psi^{\text{T}}_{2,L},\ \psi^{\text{D}}_{2,L}\right)$	N_b	$\overline{5}$	$-q_1$
$\left(\psi^{\text{T}}_{2,R},\ \psi^{\text{D}}_{2,R}\right)$	N_b	$\overline{5}$	$-q_2$
φ	1	1	$q_1 - q_2$

Table 5: Field content of a chiral model with a confining QCD-like gauge group $SU(N_b)$ and $U(1)'$. Here, $q_1 \neq q_2$. The SM model fermions are neutral under $U(1)'$ and are not listed here. The $U(1)'$ charge assignment shown here to achieve anomaly cancellation is not unique; one may also assign charges of q_2 and q_1 for $\psi_{2,L}$ and $\psi_{2,R}$, respectively.

as well as the possibility of direct production of the Z'. The chiral structure also leads to additional accidentally approximate discrete and continuous symmetries that lead to three-body decays and potentially long-lived particles.

4.2 The Chiral Composite Pseudoscalar Model

As described above, we study a model with a confining gauge group $SU(N_b)$ with a confinement scale Λ_b at $\mathcal{O}(\text{TeV})$. We introduce big-quarks charged under both the SM gauge group and $SU(N_b)$. Due to the electroweak constraints mentioned above, the big-quarks cannot be chiral under the SM gauge group, so we introduce an Abelian $U(1)'$ gauge symmetry with chiral charges. In order for the $U(1)'$ group to be gauge anomaly-free, we must have two sets of big-quarks. The chiral structure of the charges prevents large quark mass contributions from UV scales such as the GUT scale. As in the SM, we introduce a scalar field φ charged under $U(1)'$ that can develop a VEV to spontaneously break $U(1)'$ and give a mass to the corresponding gauge boson Z'. We show the content of our model as well as the gauge symmetries in Table 5.

The new fermions, $\psi_{1,2}$, transform as fundamentals or anti-fundamentals under the $SU(5)_{\text{GUT}}$ gauge group. In terms of the SM gauge interactions, $[SU(3)_c, SU(2)_W]_{U(1)_Y}$, we separate them into the QCD color-triplet $\psi^{\text{T}}_1 = (3,1)_{-1/3}$ and weak-doublet $\psi^{\text{D}}_1 = (1,2)_{1/2}$, and similarly for ψ_2.

To have both the $SU(N_b)$ and $SU(3)_c$ gauge couplings asymptotically free in the UV, we require $2 \leq N_b \leq 5$. The case with $N_b = 2$ differs from the other allowed values because it has enhanced global symmetry due to the fact that the fundamental representation of $SU(2)$ is pseudo-real. [6] It also requires the choice of $q_2(q_1)$ for $\psi_{2,L}(\psi_{2,R})$ to forbid bare mass terms of the form $\psi^T_{1,L}\,\mathcal{C}\,\psi_{2,L}$ with $\mathcal{C}$ as the charge-conjugation operator. The remainder of this chapter will focus on the cases with $3 \leq N_b \leq 5$. [7]

The $U(1)'$ charge for the scalar field φ is chosen such that it can have renormalizable interactions with the big-quarks in this model. Because of chirality under the additional $U(1)'$ gauge symmetry, there are no bare big-quark masses. On the other hand, the complex scalar field φ can have Yukawa couplings to some of new fermions. The allowed renormalizable Yukawa interactions are

$$\mathcal{L}_{\text{Yukawa}} \supset -y_1^{\text{T}}\,\varphi\,\overline{\psi}^{\text{T}}_{1,L}\,\psi^{\text{T}}_{1,R} - y_1^{\text{D}}\,\varphi\,\overline{\psi}^{\text{D}}_{1,L}\,\psi^{\text{D}}_{1,R} - y_2^{\text{T}}\,\varphi^*\,\overline{\psi}^{\text{T}}_{2,L}\,\psi^{\text{T}}_{2,R} - y_2^{\text{D}}\,\varphi^*\,\overline{\psi}^{\text{D}}_{2,L}\,\psi^{\text{D}}_{2,R} + \text{h.c.} \tag{72}$$

For simplicity, we choose identical, real Yukawa couplings such that $y_1^{\text{T}} = y_2^{\text{T}} = y_{\text{T}}$ and $y_1^{\text{D}} = y_2^{\text{D}} = y_{\text{D}}$. The most general renormalizable potential for φ is

$$V(\varphi) = m_\varphi^2\,\varphi^*\varphi + \lambda_\varphi\,(\varphi^*\varphi)^2 + \lambda_{\varphi h}\,\varphi^*\varphi\,H^\dagger H\,. \tag{73}$$

with H the Higgs doublet in the SM. The Yukawa coupling of $\lambda_{\varphi h}$ can potentially modify the SM Higgs boson properties by introducing additional decay channels. In light of the good agreement of the Higgs boson properties with the SM, there could be a stringent constraint on $\lambda_{\varphi h}$. Absorbing the electroweak VEV correction, we define a new mass for the φ field as $\overline{m}_\varphi^2 = m_\varphi^2 + \lambda_{\varphi h}\,v_{\text{EW}}^2/2$ with $v_{\text{EW}} = 246$ GeV.

If $m_\varphi^2 < 0$, similar to the Higgs field in the SM, the scalar field can develop a non-zero VEV

---

[6] In the case where $N_b = 2$, the global symmetry breaking pattern would be $SU(20) \times U(1)_\varphi \to Sp(20)$ and we would expect (399 - 210) + 1 = 190 PNGB's. The decomposition is $190 = 4\times 24 + 3\times(10+\overline{10}) + 15 + \overline{15} + 1 + 1 + 1 + 1$. Additionally, the $N_b = 2$ case has a perturbative infrared fixed point and is likely to have an approximate conformal symmetry in the IR [136].

[7] There is some debate about whether $N_b = 3$ with $N_f = 10$ is inside the conformal window [137–141]. In the later part of this chapter, we assume confinement for $N_b = 3$ and $N_f = 10$.

independent of the strong dynamics sector. For $\lambda_{\varphi h} = 0$, the VEV is $\langle\varphi\rangle = (-m_\varphi^2/\lambda_\varphi)^{1/2}/\sqrt{2}$, which could be far above the TeV scale. For this case, we need to have small Yukawa couplings, $y_{\mathrm{T,D}}$, to have small big-pion masses. The situation is very similar to the light flavors in the SM QCD sector, except that for the new Z' gauge boson to be within the low energy spectrum below around 1 TeV its gauge coupling should be small. However, if $m_\varphi^2 > 0$ the situation is even more interesting. Because the big-quark condensate can generate a tadpole term for φ through the Yukawa interactions, φ can still develop a VEV, which is triggered by the $SU(N_b)$ confinement scale Λ_b. As a result, the Z' gauge boson mass should be related to and likely below Λ_b. Some big-pions could decay into this Z', which could be a smoking gun to test our model. In this chapter, we will mainly concentrate on the case with $m_\varphi^2 > 0$.

Symmetry Breaking and Counting PNGB's

At the confinement scale of $\Lambda_b = \mathcal{O}(\mathrm{TeV})$, the gauge coupling of $SU(N_b)$ becomes large such that the bi-fermion operator develops a nonzero VEV. For a weak $U(1)'$ gauge interaction [8], following the vacuum alignment argument in Ref. [142], we anticipate the fermion condensate to spontaneously break the $U(1)'$ gauge symmetry but preserve the $SU(5)_{\mathrm{GUT}}$ symmetry. Defining $Q_L = (\psi_{1,L}, \psi_{2,L})$ and similarly for the right-handed fermions, one has

$$\langle\overline{Q}_L Q_R\rangle = \frac{\Lambda_b^3}{16\pi^2}\,\mathbb{I}_{10} \approx 4\pi\, f_\Pi^3\,\mathbb{I}_{10}\,, \tag{74}$$

which spontaneously breaks the $U(1)'$ gauge symmetry. After $\overline{Q}_L Q_R$ develops a VEV, the existence of a tadpole potential term for φ also generates a nonzero VEV defined as $\langle\varphi\rangle \equiv v_\varphi/\sqrt{2}$, which also breaks $U(1)'$. Specifically, we can write the bare fermion mass matrix $\overline{Q}_L M_Q(\varphi) Q_R$ as

$$M_Q(\varphi) = \begin{pmatrix} y_{\mathrm{T}}\,\varphi\,\mathbb{I}_3 & 0 & 0 & 0 \\ 0 & y_{\mathrm{D}}\,\varphi\,\mathbb{I}_2 & 0 & 0 \\ 0 & 0 & y_{\mathrm{T}}\,\varphi^*\,\mathbb{I}_3 & 0 \\ 0 & 0 & 0 & y_{\mathrm{D}}\,\varphi^*\,\mathbb{I}_2 \end{pmatrix}. \tag{75}$$

---

[8] The gauge coupling g' should be smaller than 0.35(0.28) for $N_b = 3(5)$ to have its Landau pole below the GUT scale; see Appendix B.2.

Using a non-linear parametrization for the big-pions, we have

$$\overline{Q}_L Q_R = \langle \overline{Q}_L Q_R \rangle \, U \; = \; \Lambda_b \, f_\Pi^2 \, \exp\left(\frac{2i \, T^A \Pi^A}{f_\Pi} \right) , \tag{76}$$

with the big-pion generators normalized such that $\mathrm{Tr}[T^A T^B] = \frac{1}{2}\delta^{AB}$. Thus, the full potential for the scalar field φ and the big-pions is

$$V(\varphi, \Pi) = \overline{m}_\varphi^2 \, \varphi^* \varphi + \lambda_\varphi (\varphi^* \varphi)^2 \; - \; \Lambda_b \, f_\Pi^2 \, \mathrm{Tr}\left[M_Q \, U + U^\dagger \, M_Q^\dagger \right] . \tag{77}$$

In the limit of $f_\Pi \ll m_\varphi$, the VEV for φ induced by the fermion condensation is

$$\langle \varphi \rangle \equiv \frac{v_\varphi}{\sqrt{2}} = \frac{2 \, \Lambda_b \, f_\Pi^2}{\overline{m}_\varphi^2} \, (3 \, y_{\mathrm{T}} + 2 \, y_{\mathrm{D}}) \left[1 \, + \, \mathcal{O}\left(\lambda_\varphi (3 \, y_{\mathrm{T}} + 2 \, y_{\mathrm{D}})^2 \frac{\Lambda_b^2 \, f_\Pi^4}{\overline{m}_\varphi^6} \right) \right] . \tag{78}$$

After fields develop their VEV's, the spontaneous global symmetry breaking pattern is

$$SU(10)_L \times SU(10)_R \times U(1)_V \times U(1)_\varphi \to SU(10)_V \times U(1)_V \, , \tag{79}$$

where we have ignored the $U(1)_A$ symmetry that is broken by the $SU(N_b)$ instanton effects. Altogether we anticipate a total of 100 pseudo Nambu-Goldstone bosons (PNGBs), the big-pions.

In addition to these continuous global symmetries, our model contains two approximate discrete symmetries. Before turning on SM and $U(1)'$ gauge interactions, one can identify the following two transformations:

$$P_m : \; \psi_1^{\mathrm{T,D}} \leftrightarrow \psi_2^{\mathrm{T,D}} \, , \qquad \varphi \to \varphi^* \, , \qquad Z'_\mu \to -Z'_\mu \, , \qquad T^A A_\mu^A \to T^A (A_\mu^A)^{\mathcal{C}} = -(T^A)^* A_\mu^A \, , \tag{80}$$

$$G_d : \; \psi_1^{\mathrm{T,D}} \to (\psi_2^{\mathrm{T,D}})^{\mathcal{C}} = i\gamma^2 (\psi_2^{\mathrm{T,D}})^* \, , \; \psi_2^{\mathrm{T,D}} \to (\psi_1^{\mathrm{T,D}})^{\mathcal{C}} = i\gamma^2 (\psi_1^{\mathrm{T,D}})^* \, , \; \varphi \to \varphi^* \, , \; Z'_\mu \to -Z'_\mu \, . \tag{81}$$

Here, $\mathcal{C}$ denotes charge conjugation and the SM gauge fields are denoted by A_μ^A. All SM fermions are invariant under both discrete transformations. The first symmetry, P_m, is just a simple matter parity and is a good symmetry when $y_1^{\mathrm{T,D}} = y_2^{\mathrm{T,D}}$. Under it, the SM gauge fields transform as by charge conjugation. The SM fermion electroweak gauge interactions explicitly break P_m. The second discrete symmetry, G_d, is a new G-parity for the new strong dynamics sector [143–146]. Because $\psi^{\rm T,D}_{1,L(R)}$ has a different absolute $U(1)'$ charge from $\psi^{\rm T,D}_{2,R(L)}$, the $U(1)'$ gauge interaction explicitly breaks this discrete symmetry.

Decomposing the 100 PNGB's into $[SU(5)_{\rm GUT}\times U(1)']^{P_m\,G_d}$ representations, we have

$$(10\times 10-1)+1 = \quad 24_0^{++}+24_0^{--}+10_{q_2+q_1}+\overline{10}_{-q_2-q_1}+15_{q_2+q_1}+\overline{15}_{-q_2-q_1}+1_0^{--}+1_0^{--}\,, \tag{82}$$

where $10(\overline{10})$ and $15(\overline{15})$ are not eigenstates of the discrete symmetries. Decomposing $SU(5)_{\rm GUT}\times U(1)'$ into representations of SM gauge groups $[SU(3)_c, SU(2)_W]_{U(1)_Y,U(1)'}$, we have $24_0=(8,1)_{0,0}+(3,2)_{-5/6,0}+(\overline{3},2)_{5/6,0}+(1,3)_{0,0}+(1,1)_{0,0}$, $10_{(q_2+q_1)}=(1,1)_{1,q_2+q_1}+(\overline{3},1)_{-2/3,q_2+q_1}+(3,2)_{1/6,q_2+q_1}$ and $15_{(q_2+q_1)}=(1,3)_{1,q_2+q_1}+(3,2)_{1/6,q_2+q_1}+(6,1)_{-2/3,q_2+q_1}$. The big-pions charged under the SM and $U(1)'$ gauge groups become massive after gauge quantum corrections. We present a calculation of their masses later. Of the remaining four gauge singlets, $(1,1)_{0,0}$, three of them are odd under both P_m and G_d, while the remaining one is even under both parities. We label the parity-even singlet as Π_{1_A}, whose generator is

$$(1,1)_{0,0}^{++}:\quad \Pi_{1_A}\quad\text{with}\quad T^{1_A}=\frac{1}{2\sqrt{30}}\,\mathrm{diag}(2\,\mathbb{I}_3,-3\,\mathbb{I}_2,2\,\mathbb{I}_3,-3\,\mathbb{I}_2)\,. \tag{83}$$

This parity-even singlet will be the lightest state in the spectrum that couples through triangle anomalies to the SM gauge bosons. The other three parity-odd states are

$$\begin{aligned}(1,1)_{0,0}^{--}:\quad &\Pi_{1_B}\quad\text{with}\quad T^{1_B}=\frac{1}{2\sqrt{30}}\,\mathrm{diag}(2\,\mathbb{I}_3,-3\,\mathbb{I}_2,-2\,\mathbb{I}_3,3\,\mathbb{I}_2)\,,\\ &\Pi_{1_C}\quad\text{with}\quad T^{1_C}=\frac{1}{\sqrt{20}}\,\mathrm{diag}(\mathbb{I}_5,-\mathbb{I}_5)\,,\\ &\phi_I\quad\ \text{with}\quad \varphi=\frac{1}{\sqrt{2}}\left(v_\varphi+\phi_R+i\phi_I\right)\,.\end{aligned} \tag{84}$$

One linear combination of Π_{1_C} and ϕ_I will be eaten by the Z' and become its longitudinal component. For the remaining three gauge singlet PNGB's, the Yukawa couplings in Eq. (72) explicitly break global $U(1)$'s associated with the PNGB's, making all gauge singlet PNGB's massive.

4.3 The Big-Pion Spectrum

We first calculate the gauge singlet PNGB spectrum. We expand Eq. (77) and find that the $(1,1)^{++}_{0,0}$ singlet Π_{1_A} has no mass mixing with other states; its mass is given by

$$m^2_{\Pi_{1_A}} = \frac{\sqrt{8}\,\Lambda_b\,v_\varphi}{5}\,(3\,y_{\rm D}\,+\,2\,y_{\rm T}) \approx \frac{8\Lambda_d^2\,f_\Pi^2}{5m_\varphi^2}\,y_{\rm T}^2\,(3+2\,\mathcal{R}_y)(2\,+3\,\mathcal{R}_y)\,, \tag{85}$$

with $\mathcal{R}_y \equiv y_{\rm D}/y_{\rm T}$. For the three $(1,1)^{--}_{0,0}$ singlets, we note that the linear combination of Π_{1_C} and ϕ_I eaten by Z' is given by its mixing term with Z' via

$$\mathcal{L} \supset g'\big(q_1 - q_2\big)Z'_\mu\,\partial^\mu\left(v_\varphi\,\phi_I + \sqrt{5}\,f_\Pi\,\Pi_{1_C}\right) \equiv g'\big(q_1-q_2\big)\,v_{Z'}\,Z'_\mu\,\partial^\mu\left(\sin\theta_{Z'}\,\phi_I\,+\,\cos\theta_{Z'}\,\Pi_{1_C}\right)\,, \tag{86}$$

with $v_{Z'}^2 = v_\varphi^2 + 5\,f_\Pi^2$ and $\sin\theta_{Z'} \equiv v_\varphi/v_{Z'}$. The Z' gauge boson mass is related to the combined VEV from fermion condensation and the VEV of φ, and is

$$m_{Z'} = g'\,|q_L - q_R|\,v_{Z'}\,=\,g'\,|q_L-q_R|\sqrt{5\,f_\Pi^2 + v_\varphi^2}\,. \tag{87}$$

Defining the orthogonal combination to the one eaten by the Z' as $\phi'_I = \cos\theta_{Z'}\,\phi_I\,-\,\sin\theta_{Z'}\,\Pi_{1_C}$, we find the square of the mass mixing matrix in the basis of $(\Pi_{1_B},\phi'_I)^T$ to be

$$\big(\Pi_{1_B},\;\phi'_I\big)\begin{pmatrix} \frac{2\sqrt{2}\,(3\,y_{\rm D}+2\,y_{\rm T})}{5}\,v_\varphi\,\Lambda_b & \frac{4\sqrt{3}\,(y_{\rm D}-y_{\rm T})}{5}\,v_{Z'}\,\Lambda_b \\ \frac{4\sqrt{3}\,(y_{\rm D}-y_{\rm T})}{5}\,v_{Z'}\,\Lambda_b & m_\varphi^2\left(1\,+\,\frac{v_\varphi^2}{5\,f_\Pi^2}\right)\end{pmatrix}\begin{pmatrix}\Pi_{1_B}\\ \phi'_I\end{pmatrix}. \tag{88}$$

The rotation matrix from the flavor basis to the mass-eigenstate basis, defined as Π_{1_β} and $\tilde{\phi}'_I$, is calculated to be

$$\begin{pmatrix}\Pi_{1_B}\\ \phi'_I\end{pmatrix} = \begin{pmatrix}\cos\eta & -\sin\eta\\ \sin\eta & \cos\eta\end{pmatrix}\begin{pmatrix}\Pi_{1_\beta}\\ \tilde{\phi}_I\end{pmatrix}, \tag{89}$$

Big-pions	$\frac{m^2_{\text{bare}}(\Pi^i)}{m^2_{\Pi_{1_A}}}$
$(8,1)_{0,0}$, $(\overline{3},1)_{-2/3,q_2+q_1}$, $(6,1)_{-2/3,q_2+q_1}$	$\frac{5}{2+3\,\mathcal{R}_y}$
$(1,3)_{0,0}$, $(1,3)_{1,q_2+q_1}$, $(1,1)_{1,q_2+q_1}$	$\frac{5\,\mathcal{R}_y}{2+3\,\mathcal{R}_y}$
$(3,2)_{-5/6,0}$, $(3,2)_{1/6,q_2+q_1}$	$\frac{5(1+\mathcal{R}_y)}{4+6\,\mathcal{R}_y}$

Table 6: The bare big-quark mass contributions to various gauge charged big-pion masses.

with $\eta \approx 4\sqrt{\frac{3}{5}}\,\Lambda_d\, f_\Pi\,(y_{\rm T} - y_{\rm D})/m_\varphi^2$. The corresponding state masses are

$$m^2_{\Pi_{1_\beta}} = 40\, y_{\rm T}\, y_{\rm D}\, \frac{\Lambda_d^2\, f_\Pi^2}{m_\varphi^2}\,, \qquad\qquad m^2_{\tilde{\phi}_I} = m_\varphi^2 + 8\,(3\, y_{\rm T}^2 + 2\, y_{\rm D}^2)\, \frac{\Lambda_d^2\, f_\Pi^2}{m_\varphi^2}\,. \tag{90}$$

For the gauge charged big-pions, we can use the electromagnetic correction to $\pi^\pm$ in the SM to estimate the radiative corrections from gauge interactions to the big-pion masses. Specifically, we use [130]

$$\Delta m^2 = \sum_{i=1,2,3,Z'} \frac{C_2(r_i)\,\alpha_i(f_\Pi)}{\alpha(f_\pi)}\, \frac{f_\Pi^2\, \Delta m_\pi^2}{f_\pi^2}\,, \tag{91}$$

with $\Delta m_\pi^2 = m^2_{\pi^\pm} - m^2_{\pi^0}$ and $f_\pi = 93$ MeV. This formula may not work for non-QCD-like strong dynamics. Additional uncertainties on our spectrum calculation would apply in this case. Here, $C_2(r_i)$ is the quadratic Casimir of the representation r_i under the SM i'th and Z' gauge groups. To calculate the bare big-quark mass contribution to big-pion masses, we use the Dashen formula

$$M^2_{AB} = \frac{1}{f_\Pi^2}\langle \overline{Q}\,\{T^A, \{T^B, M_Q\}\}Q\,\rangle\,. \tag{92}$$

The results of various gauge charged big-pion masses are shown in Table 6.

Searches for diphoton resonances put the strongest constraints on the model parameters [126,127]. To discuss the features of this spectrum, we choose a benchmark mass of $m_{\Pi_{1A}} = 1.5$ TeV for Π_{1_A}. The ATLAS and CMS collaborations place constraints on the diphoton production cross section for a 1.5 TeV scalar at ~ 0.2 fb, so we target a production cross section of $\sigma = 0.1$ fb, which fixes

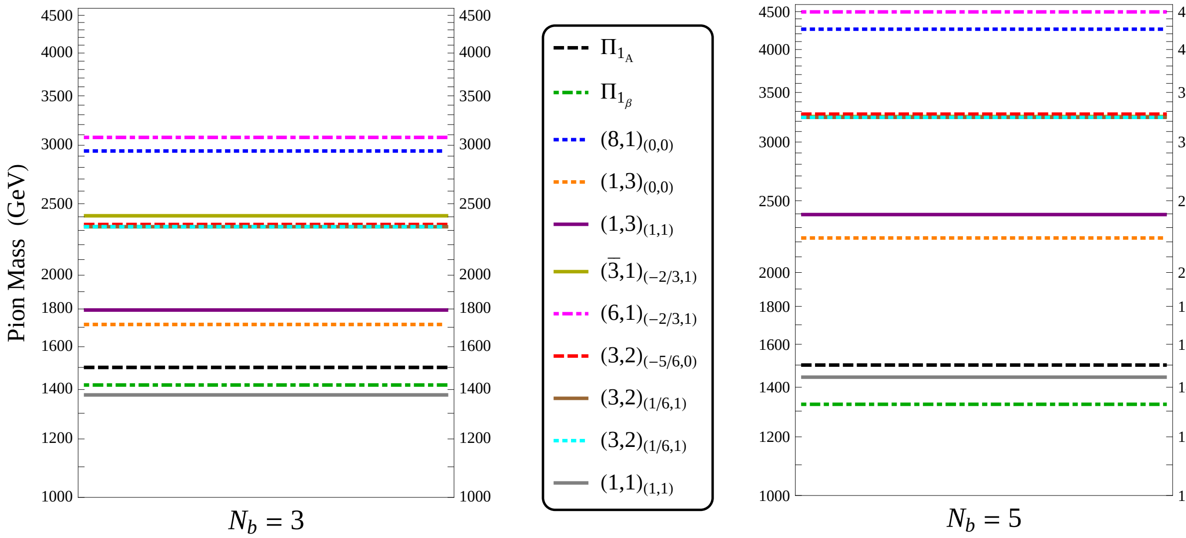

Figure 20: Big-pion mass spectrum for $m_{\Pi_{1_A}} = 1500$ GeV and $g'(m_{\Pi_{1_A}}) = 0.2$. The values of f_Π used here give a 0.1 fb diphoton cross section for each N_b value.

the value of the big-pion decay constant at $f_\Pi = (1040, 1380, 1730)$ GeV for $N_b = (3, 4, 5)$. Then there is only one additional independent combination of Yukawa couplings which we take to be $\mathcal{R}_y = y_{\rm D}/y_{\rm T}$. As a further benchmark choice, we fix the values of $\mathcal{R}_y$ for different N_b by choosing an identical boundary condition with $y_{\rm D} = y_{\rm T}$ at the GUT scale. As shown in Appendix B.3, the ratio $\mathcal{R}_y$ is insensitive to the actual boundary values and ranges from 0.51 for $N_b = 3$ to 0.36 for $N_b = 5$. Fixing the preferred $\mathcal{R}_y$ values and adding bare big-quark mass and gauge loop contributions to the big-pion masses together, we show the benchmark mass spectra in Fig. 20 for $N_b = 3$ and $N_b = 5$. From Fig. 20, one can see that Π_{1_A} is not the lightest big-pion in the spectrum; the gauge singlet big-pion Π_{1_β} and the big-pion only charged under $U(1)_Y$ and $U(1)'$ are slightly lighter than 1500 GeV. The heaviest big-pion is the color-sextet and has a mass from about 3.1 TeV ($N_b = 3$) to 4.5 TeV ($N_b = 5$). Following that is the color-octet big-pion with an almost degenerate mass. The radiative corrections from gauge interactions are very important. For instance, the fraction of the QCD-gauge-loop contribution to the color-octet big-pion mass square is around 63% for $N_b = 3$ and 80% for $N_b = 5$. The CP-odd state $\tilde{\phi}_I$ and its CP-even partner ϕ_R, both of which have much heavier masses, are not shown in Fig. 20. For a fixed value of $\mathcal{R}_y$ and requiring no Landau pole for the Yukawa coupling $y_{\rm T}$ below the GUT scale, we have an upper bound on the mass parameter $m_\varphi \lesssim (23, 36, 52)$ TeV for $N_b = (3, 4, 5)$, after fixing $m_{\Pi_{1A}}$ and f_Π

to our benchmark choices.

4.4 Properties of Z'

As shown in Eq. (87), the Z' mass is related to the chiral symmetry breaking scale of the new strong dynamics sector. For a weak gauge coupling of g' on the order of electromagnetic interaction strength, the Z' mass is anticipated to be $\sim$ 500 GeV for f_Π fitting our benchmark parameters. There are no tree-level interactions of the Z' with SM particles. At loop-level, we have found that the kinetic mixing of the Z' with SM hypercharge gauge boson determines its interactions with the SM and decay properties. The relevant kinetic mixing term is defined as

$$\mathcal{L} \supset -\frac{1}{4}\hat{B}_{\mu\nu}\hat{B}^{\mu\nu} - \frac{1}{4}\hat{Z}'_{\mu\nu}\hat{Z}'^{\mu\nu} - \frac{\sin\chi}{2}\,\hat{B}_{\mu\nu}\,\hat{Z}'_{\mu\nu}\,, \tag{93}$$

in the flavor basis. The mixing parameter $\sin\chi$ is scale-dependent. Above the GUT scale, $y_\mathrm{D} = y_\mathrm{T}$ and $\mathrm{Tr}(T_Y\,T_{Z'}) = 0$, so this coefficient is zero. Below the GUT scale, due to different coupling running of y_D and y_T (see Appendix B.3), a non-zero value of $\sin\chi$ is generated from a vacuum polarization "bubble digram" with $\hat{B}$ and $\hat{Z}'$ as external fields. At one-loop, the resulting mixing angle is [147]

$$\sin\chi = \frac{N_b\, g_Y\, g'}{6\pi^2}(q_1+q_2)\ln\left(\frac{y_\mathrm{D}}{y_\mathrm{T}}\right). \tag{94}$$

In Appendix B.4, we diagonalize both the kinetic and mass mixings of the Z', γ and Z boson system. Various decay branching ratios of the Z' are shown in the left panel of Fig. 21. For the benchmark point of $g' = 0.2$, $N_d = 4$ and $f_\Pi = 1380$ GeV, the Z' mass is $m_{Z'} = 620$ GeV and its width is $\Gamma_{Z'} \approx 164$ keV. For a lighter Z' below around 50 GeV, the Z' has similar couplings to SM fermions as the SM photon, while for a heavier mass above about 200 GeV, the Z' behaves more like a hypercharge gauge boson. Unless its mass is close to the SM Z boson value, the leptonic branching ratio of this Z' is a factor of $4-5$ larger than the SM Z boson. For the benchmark point of $m_{Z'} = 620$ GeV, the leptonic branching ratio of the Z' is 25%.

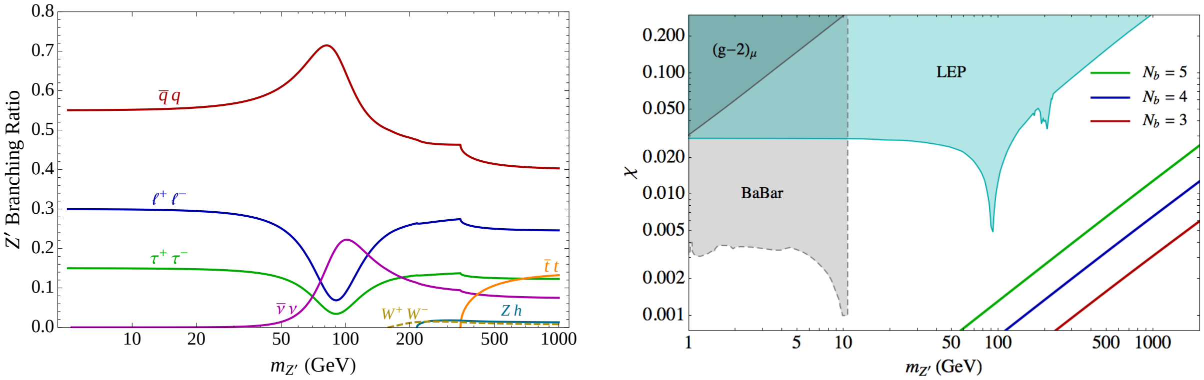

Figure 21: Left panel: the decay branching ratios of Z' to SM particles. Right panel: 95% CL exclusion limits on Z' kinetic mixing as a function of mass for different N_b.

In the right panel of Fig. 21, we show the bounds on the mass and kinetic mixing of a Z' boson from precision measurements of SM observables [148]. Low mass Z' bosons are most strongly constrained by the muon anomalous magnetic moment [149] and BaBar searches for dark gauge bosons in four-lepton final states [150], whereas high mass Z' bosons are constrained by e^+e^- collider measurements [151]. Not shown are additional narrow-Z' enhanced constraints from various e^+e^- experiments where $m_{Z'} \simeq \sqrt{s}$ that do not affect our conclusion. We conclude that our model parameter region is unconstrained by low-energy experiments.

4.5 Properties of Big-Pions

Starting with Π_{1_A}, we list the most relevant interactions for all big-pions in our model spectrum. Since the triangle anomaly mediated interactions become the leading interactions for the big-pions with real representations under the SM and $U(1)'$ gauge groups, we first introduce a general formula for these types of interactions. Additional higher-dimensional operators are required to induce decays of the QCD triplet and sextet, as well as $U(1)_Y$ or $U(1)'$ charged big-pions.

For big-pions charged under real representations of SM gauge group, the general form for the triangle anomaly mediated interaction is

$$\mathcal{L}_{\text{anomaly}} \supset -\frac{g_A\, g_B\, N_b}{64\pi^2\, f_\Pi}\epsilon^{\mu\nu\rho\sigma}\,\Pi^C\, F^A_{\mu\nu}\, F^B_{\rho\sigma}\, d^{ABC}\,, \tag{95}$$

Types	$\mathcal{A}_{GG}$	$\mathcal{A}_{\gamma\gamma}$	$\mathcal{A}_{Z\gamma}$	$\mathcal{A}_{ZZ}$	$\mathcal{A}_{WW}$	$\mathcal{A}_{Z'\gamma}$	$\mathcal{A}_{Z'Z}$
Couplings	$-g_s^2$	$\frac{7}{3}\,e^2$	$\frac{(9\,t_W^{-1} - 5\,t_W)}{3}\,e^2$	$\frac{(9\,t_W^{-2} + 5\,t_W^2)}{6}\,e^2$	$\frac{3}{s_W^2}\,e^2$	$5\,g'e$	$-5\,t_W\,g'e$

Table 7: The coefficients of Π_{1_A} triangle anomaly interactions with two gauge bosons as defined by $N_b/(16\sqrt{30}\,\pi^2 f_\Pi)\,\mathcal{A}_{XY}\,\Pi_{1_A}\,\epsilon_{\mu\nu\alpha\beta}X^{\mu\nu}Y^{\alpha\beta}$. Here, $t_W \equiv \tan\theta_W$ and θ_W is the Weinberg angle.

where the group structure constant is $d^{ABC} = 2\,\mathrm{Tr}\left[T^C\,\{T^A,\,T^B\}\right]$. Here, the normalization for the big-pion generators is canonical with $\mathrm{Tr}[T^C T^{C'}] = \frac{1}{2}\delta^{CC'}$. The SM gauge group generators are reducible and have 10×10 representations as $T^A = \mathrm{diag}(t^A, -t^{A*})$, with $\mathrm{Tr}(T^A T^B) = \delta^{AB}$, in the space of the big-pions.

Properties of Parity-Even Π_{1_A}

Using the general triangle anomaly interaction formula Eq. (95), we have interactions for Π_{1_A}, which is even under both the P_m and G discrete symmetries, shown in Table 7. Based on the interactions of Π_{1_A} with gauge bosons, we calculate its various partial widths. For instance, one has

$$\begin{aligned}
\Gamma(\Pi_{1_A} \to gg) \;\; &= \frac{8\,N_b^2\,g_s^4\,m_{\Pi_{1_A}}^3}{30 \times 16^2\,\pi^5\,f_\Pi^2}\,, \\
\Gamma(\Pi_{1_A} \to \gamma\gamma) \;\; &= \frac{49\,N_b^2\,e^4\,m_{\Pi_{1_A}}^3}{270 \times 16^2\,\pi^5\,f_\Pi^2}\,, \\
\Gamma(\Pi_{1_A} \to Z'\gamma) &= \frac{25\,N_b^2\,g'^2 e^2\,m_{\Pi_{1_A}}^3}{60 \times 16^2\,\pi^5\,f_\Pi^2}\left(1 - \frac{m_{Z'}^2}{m_{\Pi_{1_A}}^2}\right)^3 .
\end{aligned} \tag{96}$$

There also exist additional interactions of Π_{1_A} with other big-pions. For instance, the following charge radius transition operator

$$c_{Z'}\,\frac{g'}{16\pi^2\,f_\Pi^2}\,\partial^\mu\Pi_{1_A}\,\partial^\nu\Pi_{1_\beta}\,Z'_{\mu\nu}\,, \tag{97}$$

can mediate a sub-dominant decay of Π_{1_A} into (off-shell) Π_{1_β} and Z'.

Numerically, we show the various branching ratios and the total width of Π_{1_A} in Table 8 for a fixed gauge coupling of $g' = 0.2$ with a corresponding Z' mass of 620 GeV. We can see that the branching

Mode	gg	$\gamma\gamma$	$Z\gamma$	ZZ	WW	$Z'\gamma$	$Z'Z$
Branching ratio	0.90	0.0046	0.0082	0.021	0.065	0.0025	0.0008
Γ_{tot}	$137\text{ MeV}\left(\frac{N_b}{4}\right)^2\left(\frac{1380\text{ GeV}}{f_\Pi}\right)^2$						

Table 8: The branching ratios and total width for Π_{1_A} with a mass of 1500 GeV. For decays involving the massive Z' gauge boson, $g' = 0.2$ and $m_{Z'} \approx 620$ GeV for $f_\Pi = 1380$ GeV and $N_b = 4$.

ratio into $Z'\gamma$ is comparable to the diphoton one. Depending on the subsequent decays of the Z', one could search for $Z'\gamma$ resonances to confirm this model.

Experimental signatures of this model may first appear in the diphoton channel. Using its couplings to two gluons and two photons, we compute the production cross section for $gg \to \Pi_{1_A} \to \gamma\gamma$, which in the narrow width approximation is given by $\sigma(gg \to \Pi_{1_A} \to \gamma\gamma) = \sigma(gg \to \Pi_{1_A}) \times \text{Br}(\Pi_{1_A} \to \gamma\gamma)$, with

$$\sigma(gg \to \Pi_{1_A}) = \frac{N_b^2\, g_s^4\, m_{\Pi_{1_A}}^4}{30 \times 16^2\, \pi^4\, f_\Pi^2}\, \frac{\pi}{\hat{s}} \delta(\hat{s} - m_{\Pi_{1_A}}^2)\,. \tag{98}$$

Here, $\hat{s}$ means the center-of-mass energy of partons. Integrating this cross section with the MSTW2008 NNLO central parton distribution function set [152] and an NNLO K-factor of 2.5 [153] for a 1500 GeV big-pion at the 13 TeV LHC, we have the required f_Π as

$$f_\Pi = 1380\,\text{GeV}\left(\frac{N_b}{4}\right)\left(\frac{0.1\,\text{fb}}{\sigma \times \text{Br}}\right)^{1/2}\,. \tag{99}$$

In Fig. 22, we show the diphoton rate as a function of f_Π for different big-colors N_b. The decay constants fitting our benchmark diphoton cross section of 0.1 fb range from roughly 1 TeV to 1.7 TeV, so the related confinement scale $\Lambda_b \sim 4\pi f_\Pi$ varies from 13 TeV to 22 TeV. The heavier states including vector ρ_b, a_b mesons and baryons are heavy and unlikely to be probed by the LHC Run 2. The baryons in our model either decay via higher dimension operators or are stable and form a component of the dark matter. We don't explore their properties in detail in this chapter.

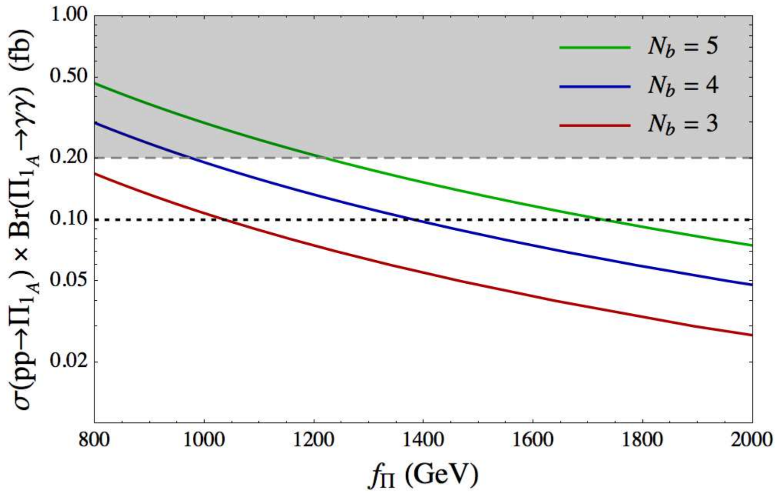

Figure 22: The diphoton rate as a function of f_Π for different N_b. The shaded region shows the exclusion limit from the ATLAS diphoton search at our benchmark mass of 1.5 TeV [127].

In our chiral composite model, Π_{1_A} decays to $Z'\gamma$ with a similar branching fraction to $\gamma\gamma$. For our benchmark point with $g' = 0.2$ and $m_{Z'} = 620$ GeV, the production cross section times branching ratio of the final state of $\ell^+\ell^-\gamma$ is

$$\sigma(pp \to \Pi_{1_A}) \times \mathrm{Br}(\Pi_{1_A} \to Z'\gamma) \times \mathrm{Br}(Z' \to \ell^+\ell^-) \approx \left(\frac{g'}{0.2}\right)^2 \times 0.013 \text{ fb}\,, \tag{100}$$

at the 13 TeV LHC. While this channel is unlikely to provide the first hints of new physics from this model, observation of such a decay mode serves as a key indicator of new chiral dynamics in the big-color sector.

Properties of Parity-odd Π_{1_β}

A single parity-odd big-pion, Π_{1_β}, cannot couple to two gauge bosons because of the discrete symmetries. From a box diagram at one loop, we expect it to couple to three gauge bosons. For instance, one can have the following dimension-9 operator

$$c^G_\beta \, \frac{g_s^2\, g'}{16\pi^2\, f_\Pi\, \Lambda_b^4}\, \partial_\mu \Pi_{1_\beta}\, G^a_{\mu\rho}\, \widetilde{G}^{a\,\rho}_{\sigma}\, \partial_\nu Z'^{\,\nu\sigma}\,, \tag{101}$$

and similar interactions with the W^i and B gauge bosons. So, the leading decay channel of Π_{1_β} is $\Pi_{1_\beta} \to ggZ'$. The dimension-7 operator like $\Pi_{1_\beta} G^a_{\mu\rho} \widetilde{G}^{a\,\rho}_{\sigma} Z'_{\mu\sigma}$ can be shown to be zero. There also exist operators containing two Π_{1_β}'s, for instance

$$c^{GG}_\beta \, \frac{g_s^2}{16\pi^2 \, f_\Pi^2} \, \Pi_{1_\beta} \, \Pi_{1_\beta} \, G^a_{\mu\nu} \, G^{a\,\mu\nu} \,, \tag{102}$$

with c^{GG}_β coming from the strong dynamics and of order unity. This operator provides the dominant interaction for producing Π_{1_β} at the LHC. For $c^{GG}_\beta = 1$, $f_\Pi = 1040$ GeV, and $m_{\Pi_{1_\beta}} = 1400$ GeV, the production cross section of $pp \to \Pi_{1_\beta}\Pi_{1_\beta}$ is 0.005 fb at the 13 TeV LHC, which is unlikely to be observed at the LHC Run 2. After both Π_{1_β}'s decay, we have a very interesting signature with four jets plus one or two leptonic Z'.

Properties of Parity-even Color-octet Π_8

The parity-even color-octet can also couple to two SM gauge bosons through triangle anomalies. Because of the QCD gauge invariance, it couples to two gluons or one gluon plus one hypercharge boson. After electroweak symmetry breaking, the relevant interactions are

$$\begin{aligned} \mathcal{L}_{\rm anomaly} \supset & - \frac{1}{\sqrt{2}} \frac{N_b \, g_s^2}{32\pi^2 f_\Pi} \, d^{abc} \, \Pi_8^a \, \epsilon^{\mu\nu\rho\sigma} \, G^b_{\mu\nu} \, G^c_{\rho\sigma} - \frac{2\sqrt{2}}{3} \frac{N_b \, g_s \, e}{32\pi^2 f_\Pi} \, \Pi_8^a \, \epsilon^{\mu\nu\rho\sigma} \, G^a_{\mu\nu} \, F_{\rho\sigma} \\ & + \frac{2\sqrt{2}}{3} \frac{N_b \, g_s \, e \, t_W}{32\pi^2 f_\Pi} \, \Pi_8^a \, \epsilon^{\mu\nu\rho\sigma} \, G^a_{\mu\nu} \, Z_{\rho\sigma} - \sqrt{2} \, \frac{N_b \, g_s \, g'}{32\pi^2 f_\Pi} \, \Pi_8^a \, \epsilon^{\mu\nu\rho\sigma} G^a_{\mu\nu} \, Z'_{\rho\sigma} \,. \end{aligned} \tag{103}$$

After summing color factors, the partial widths of Π_8 are given by

$$\begin{aligned} &\Gamma(\Pi_8 \to gg) = \frac{25}{4} \frac{N_b^2 \, g_s^4 \, m^3_{\Pi_8}}{30 \times 16^2 \, \pi^5 \, f_\Pi^2} \,, && \Gamma(\Pi_8 \to g\gamma) = \frac{8\,\alpha}{15\,\alpha_s} \, \Gamma(\Pi_8 \to gg) \,, \\ &\Gamma(\Pi_8 \to gZ) = \frac{8\,\alpha\, t_W^2}{15\,\alpha_s} \, \Gamma(\Pi_8 \to gg) \,, && \Gamma(\Pi_8 \to gZ') = \frac{6\, g'^2}{5\, g_s^2} \, \Gamma(\Pi_8 \to gg) \,. \end{aligned} \tag{104}$$

Numerically, we show the various decay branching ratios and the total width in Table 9.

At the LHC, the color-octet big-pion can be singly produced from two gluons. The parton-level

Mode	gg	gZ'	$g\gamma$	gZ
Branching ratio	0.91	0.038	0.042	0.013
$\Gamma_{\rm tot}$	$1.45~{\rm GeV}\left(\frac{N_d}{4}\right)^2\left(\frac{1380~{\rm GeV}}{f_\Pi}\right)^2$			

Table 9: The branching ratios and total width for Π_8 with mass 3580 GeV. For decays involving the massive Z' gauge boson, $g' = 0.2$ was used. All phase space and polarization factors have been neglected here due to the large Π_8 mass.

production cross section is

$$\sigma(gg \to \Pi_8) = \frac{25}{4}\frac{N_b^2\, g_s^4\, m_{\Pi_8}^4}{30 \times 16^2\, \pi^4\, f_\Pi^2}\, \frac{\pi}{\hat{s}}\delta(\hat{s} - m_{\Pi_8}^2)\,. \tag{105}$$

It is also interesting to compare the above formula to the color-singlet production in Eq. (98). The ratio of the two cross sections is

$$\frac{\sigma(gg \to \Pi_8)}{\sigma(gg \to \Pi_{1_A})} = \frac{25}{4}\,\frac{m_{\Pi_8}^2\,\delta(\hat{s} - m_{\Pi_8}^2)}{m_{\Pi_{1_A}}^2\,\delta(\hat{s} - m_{\Pi_{1_A}}^2)}\,, \tag{106}$$

which is independent of f_Π and N_d.

Integrating this parton-level cross section with the MSTW2008 NNLO central parton distribution function set and an NNLO K-factor of 3.0 [154] for the benchmark mass 3580 GeV ($f_\Pi \sim 1380$ GeV and $N_b = 4$) color-octet at the 13 TeV LHC, we find $\sigma(gg \to \Pi_8 \to gZ') \sim 0.05\,{\rm fb}$ for $g' = 0.2$. For different masses, we show the color-octet single production cross section times branching ratio in Fig. 23 for $g\gamma$ (left panel) and gZ' (right panel). As already studied in Ref. [155], the dijet and jet plus photon resonance searches have already imposed stringent constraints on the color-octet production cross sections. However, color-octet pions from the benchmark points considered here are unconstrained by such searches.

Different from the pure vector-like models in Ref. [155], one can also search for the color-octet big-pion as a three-body resonance of $j\,\ell^+\ell^-$ with a mass between 3 TeV to 4.3 TeV. The signal cross section times branching ratio is 0.013 fb for a 3580 GeV color-octet pion which, while unlikely

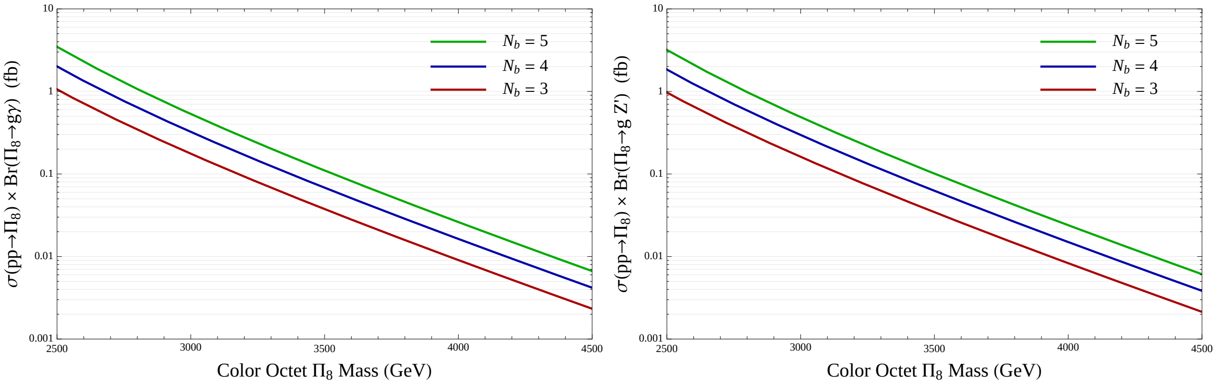

Figure 23: Color-octet big-pion $\Pi_8 \equiv (8,1)_{0,0}$ single production cross-section times its branching ratio to $g\gamma$ (left panel) and gZ' (right panel) as a function of mass at the 13 TeV LHC. This color-octet big-pion is even under both parities, namely $(P_m, G_d) = (+,+)$. An NNLO K-factor of 3.0 was used [154].

to be observed in the near future, provides a relatively clean signal for high luminosity LHC. The color-octet big-pions can also be pair produced via their QCD interactions (see Refs. [99, 100, 156] for similar phenomenology studies). The leading discovery channel is a pair of dijet resonances, but the semi-weak decays of one octet big-pion into $g\gamma$ and gZ' should be visible as well.

Properties of Parity-Odd Color-Octet Π_8^{odd}

The discrete-symmetry-odd color-octet big-pion Π_8^{odd} can decay into three gauge bosons via the following dimension-7 operator

$$c_8^{\mathrm{o}\,GG}\,\frac{g_s^2\,g'}{16\pi^2\,f_\Pi\,\Lambda_b^2}\,f^{abc}\,\Pi_8^{\mathrm{odd}\,a}\,G^b_{\mu\rho}\,\widetilde{G}^{c\,\rho}_{\nu}\,Z'^{\,\mu\nu}\,,\qquad c_8^{\mathrm{o}\,GB}\,\frac{g_s\,g_Y\,g'}{16\pi^2\,f_\Pi\,\Lambda_b^2}\,\Pi_8^{\mathrm{odd}\,a}\,G^a_{\mu\rho}\,\widetilde{B}^{c\,\rho}_{\nu}\,Z'^{\,\mu\nu}\,. \tag{107}$$

Furthermore, it can also decay into the lighter discrete-symmetry-odd singlet Π_{1_β} via the dimension-6 operators

$$c_{8\beta}^{\mathrm{o}\,GG}\,\frac{g_s^2}{16\pi^2\,f_\Pi^2}\,d^{abc}\,\Pi_8^{\mathrm{odd}\,a}\,\Pi_{1_\beta}\,G^b_{\mu\nu}\,G^{c\,\mu\nu}\,,\qquad c_{8\beta}^{\mathrm{o}\,GB}\,\frac{g_s\,g_Y}{16\pi^2\,f_\Pi^2}\,\Pi_8^{\mathrm{odd}\,a}\,\Pi_{1_\beta}\,G^a_{\mu\nu}\,B^{\mu\nu}\,, \tag{108}$$

which should provide the leading decaying channels $\Pi_8^{\rm odd} \to \Pi_{1_\beta} + 2g/g\gamma/gZ$. Similarly, $\Pi_8^{\rm odd}$ can also decay into Π_{1_A} via

$$c_{8A}^{{\rm o}\,GZ'}\,\frac{g_s\,g'}{16\pi^2\,f_\Pi^2}\,\Pi_8^{{\rm odd}\,a}\,\Pi_{1_A}\,G^a_{\mu\nu}\,Z'^{\,\mu\nu}\,, \tag{109}$$

which provides the subdominant decay channel $\Pi_8^{\rm odd} \to \Pi_{1_A}\,g\,Z'$.

At the 13 TeV LHC, $\Pi_8^{\rm odd}$ could be pair-produced via its QCD interactions. The tree-level production cross section is around $2.3 \times 10^{-4}(7.8 \times 10^{-6})$ fb for a 3.0(3.6) TeV $\Pi_8^{\rm odd}$, which is too small to be observed at the LHC.

Properties of Weak Triplets Π_3 and $\Pi_3^{\rm odd}$

The discrete-symmetry-even weak-triplet Π_3 contains both electric charged big-pions $\Pi_3^\pm$ and a neutral big-pion Π_3^0. Through the triangle anomaly, they can couple to two gauge bosons via

$$\begin{aligned}\mathcal{L}_{\rm anomaly} \supset &+ \sqrt{2}\frac{N_b\,e}{32\pi^2\,s_W\,f_\Pi}\,\epsilon^{\mu\nu\rho\sigma}\,(\Pi_3^+\,W^-_{\mu\nu} + \Pi_3^-\,W^+_{\mu\nu})(e\,F_{\rho\sigma} - e\,t_W\,Z_{\rho\sigma} - g'\,Z'_{\rho\sigma}) \\ &+ \sqrt{2}\frac{N_b\,e^2}{32\pi^2 f_\Pi}\,\epsilon^{\mu\nu\rho\sigma}\,\Pi_3^0\,\left[(t_W^{-1} - t_W)\,Z_{\mu\nu}\,F_{\rho\sigma} + F_{\mu\nu}\,F_{\rho\sigma} - Z_{\mu\nu}\,Z_{\rho\sigma}\right] \\ &- \sqrt{2}\,\frac{N_b\,g'\,e}{32\pi^2 f_\Pi}\,\epsilon^{\mu\nu\rho\sigma}\,\Pi_3^0\,(F_{\mu\nu}\,Z'_{\rho\sigma} + t_W^{-1} Z_{\mu\nu}\,Z'_{\rho\sigma})\,.\end{aligned} \tag{110}$$

We show numerical values for the various branching ratios in Table 10 for the benchmark model point with a mass of 970 GeV. At the LHC, the weak-triplet big-pions can be singly produced from vector-boson fusion with two forward jets and small cross sections. They can also be produced in pairs from their weak interactions. While the weak triplets are unlikely to be observed at the LHC, a future 100 TeV collider could be capable of probing these states.

For the discrete-symmetry-odd weak-triplet $\Pi_3^{\rm odd}$ and similar to the color-octet case, the leading decaying operators are

$$c_{3\beta}^{{\rm o}\,WB}\,\frac{e^2}{16\pi^2\,s_W\,c_W\,f_\Pi^2}\,\Pi_3^{{\rm odd}\,i}\,\Pi_{1_\beta}\,W^i_{\mu\nu}\,B^{\mu\nu}\,, \qquad c_{3A}^{{\rm o}\,WZ'}\,\frac{e\,g'}{16\pi^2\,s_W\,f_\Pi^2}\,\Pi_3^{{\rm odd}\,i}\,\Pi_{1_A}\,W^i_{\mu\nu}\,Z'^{\,\mu\nu}\,. \tag{111}$$

Π_3^0 decay	$\gamma\gamma$	ZZ	$Z\gamma$	$Z'\gamma$	$Z'Z$
Br	0.28	0.28	0.204	0.057	0.179
Γ_{tot}	$14\ \text{MeV}\left(\frac{N_d}{4}\right)^2\left(\frac{1380\ \text{GeV}}{f_\Pi}\right)^2$				

$\Pi_3^\pm$ decay	$W^\pm\gamma$	$W^\pm Z$	$W^\pm Z'$
Br	0.579	0.186	0.236
Γ_{tot}	$14\ \text{MeV}\left(\frac{N_d}{4}\right)^2\left(\frac{1380\ \text{GeV}}{f_\Pi}\right)^2$		

Table 10: The decay branching ratios and total width for Π_3^0 (left panel) and $\Pi_3^\pm$ (right panel) with a mass of 1960 GeV. For decays involving the massive Z' gauge boson, $g' = 0.2$ was used.

So, the main decay channels for the charged states are $\Pi_3^{\text{odd}\,\pm} \to \Pi_{1_\beta} W^\pm Z/\gamma$ and $\Pi_{1_A} W^\pm Z'$.

Additional UV Interactions of Complex Big-Pions

Additional interactions in the UV physics are required to make the big-pions with complex representations under SM gauge groups decay [157]. In general, there are two classes of operators, depending on whether additional φ insertions are needed or not. If we write down such operators in a GUT-preserving form, then the gauge structure of the operator is fixed. The big-pions with complex SM representations can come from either the decomposition of 5×5 (and $\overline{5} \times \overline{5}$ which we neglect as it can be treated analogously by conjugation) or $5 \times \overline{5}$. To allow all complex big-pions to decay, we need to introduce operators in which the SM fields transform as $\overline{10}$, $\overline{15}$ and 24. The $\overline{10}$ can come from $\overline{5} \times \overline{5}$ or 5×10. Both cases lead to one big-pion that decays as a leptoquark and one big-pion that decays as a diquark. The $\overline{15}$ must come from a product of $\overline{5} \times \overline{5}$ SM fermions, such that the $(6,1)_{-2/3,q_1+q_2}$ decays as down-type diquarks, while the $(\bar{3},2)_{1/6,q_1+q_2}$ behaves as a leptoquark. The QCD-neutral complex big-pions decay to leptons. The operator with SM fields in a 24 can come from a $5 \times \overline{5}$ or a $10 \times \overline{10}$. In either case, it decays as a diquark. For complex big-pions that also have $U(1)'$ charge, additional insertions of the φ field are required. If we choose $q_1 = 1$ and $q_2 = 0$, then only one insertion is required and the UV operators inducing the decays are dimension-7. In order to have $(3,2)_{-5/6,0}$ decay, one also needs to add a dimension-6 operator without φ insertion. For example, one could introduce decays for all complex big-pions with the following operators,

$$\frac{\varphi^* \overline{\psi}_{2i} \gamma^5 \psi_{1j} \overline{5}_i P_L \overline{5}_j}{\Lambda_1^3}\,, \qquad \frac{\overline{\psi}_2 \gamma^\mu \gamma^5 T^A \psi_2\, \overline{5} \gamma^\mu P_R T^A 5}{\Lambda_2^2}\,, \tag{112}$$

Big-Pion	Decay Modes
Π_{1_A}	gg, $\gamma\gamma$, $Z\gamma$, ZZ, WW, $Z'\gamma$, $Z'Z$
Π_{1_β}	ggZ'
$(8,1)^{++}_{0,0}$	gg, $g\gamma$, gZ, gZ'
$(8,1)^{--}_{0,0}$	$\Pi_{1_\beta}(gg, g\gamma, gZ)$, $\Pi_{1_A}\, g\, Z'$
$(1,3)^{++}_{0,0}$	$W\gamma$, WZ, $\gamma\gamma$, γZ, ZZ, $\gamma Z'$, ZZ', WZ'
$(1,3)^{--}_{0,0}$	$\Pi_{1_\beta}(W\gamma, WZ, \gamma\gamma, ZZ, Z\gamma)$, $\Pi_{1_A}(WZ', \gamma Z', ZZ')$

Big-Pion	Decay Modes
$(6,1)_{-2/3,\, q_2+q_1}$	di-quark
$(1,3)_{1,\, q_2+q_1}$	di-lepton
$(1,1)_{1,\, q_2+q_1}$	di-lepton
$(\overline{3},1)_{-2/3,\, q_2+q_1}$	di-quark, leptoquark
$(3,2)_{-5/6,\, 0}$	leptoquark
$(3,2)_{1/6,\, q_2+q_1}$	di-quark, leptoquark

Table 11: A summary of all big-pion decays. Left: big-pions in real representations with collider prompt decay modes. Right: big-pions in complex representations which may live long enough to be collider stable.

where i, j are indices of $SU(5)$ and we suppress Lorentz and flavor indices. The new particles required to UV-complete the above two operators may change gauge coupling running if they are not $SU(5)$ singlets.

These operators break the discrete symmetries of the theory and so induce decays for both even and odd big-pions. To have these big-pions decay before Big Bang Nucleosynthesis ($\sim$ 1 s), we estimate that the cutoff scales should be less than $\mathcal{O}(10^7\,\text{GeV})$ and $\mathcal{O}(10^{10}\,\text{GeV})$, for Λ_1 and Λ_2 respectively. If the abundance of the complex big-pions is small, their lifetime could be longer and leads to weaker constraints on cutoffs [158]. Searches for stopped long-lived particles at the 8 TeV LHC place a bound on the color triplet mass of to be above around 470 GeV, for a wide range of decay times, $10^{-6}\,\text{s} \lesssim \tau \lesssim 10^4\,\text{s}$ [159]. Similarly for the color sextet, the bound is that the mass should be above around 690 GeV. Furthermore, for τ above $\mathcal{O}(10$ ns$)$, the searches for long-lived charged particles have imposed a more stringent bound, which requires the color triplet complex scalar mass above around 900 GeV [160]. This constraint can be easily satisfied in our model, as can be seen in Fig. 20. Since the colored big-pions in our model are much heavier, we do not anticipate any constraints coming from these bounds. We show the summary table of all big-pion decays in Table 11.

4.6 Discussion

In this chapter we have examined signatures of a chiral composite model in the context of LHC Run 2 discovery. To avoid spoiling the unification of the SM gauge couplings we require that the new matter content be embedded in complete $SU(5)$ GUT representations. The chiral structure is then necessitated by the desire to explain the small masses of the constituent fermions relative to the GUT scale. While recent searches for diphoton resonances by ATLAS and CMS have placed strong constraints on the production cross section of the lightest state coupling to SM gauge bosons, we find that regions of parameter space exist where diphoton signatures would be observable by the end of Run 2. For the benchmark choice of $m_{\Pi_{1_A}} = 1.5$ TeV and $f_\Pi = 1380$ GeV for $N_b = 4$, a production cross section times branching ratio to two photons of $\sigma \times \mathrm{Br} \sim 0.1$ fb could be observable in the near future.

The model also predicts a rich spectrum of pseudo-scalars accompanying the potential digamma resonance. Among the unique features of this model, it predicts two very interesting decay channels involving the Z' gauge boson. One is the decay of Π_{1_A} to $Z'\gamma$ and the other is the decay of the color-octet big-pion to gZ'. For our benchmark model point with $g' = 0.2$ and $m_{Z'} = 620$ GeV, the Z' has roughly a 25% branching fraction to a di-lepton final state, giving signatures of $\ell^+\ell^-\gamma$ or $\ell^+\ell^- j$. If a scalar resonance is confirmed in the future, these signals could be considered smoking gun signatures for chiral composite models.

5 Heavy Stop Searches at the LHC

In this chapter, we focus exclusively on searches for the SUSY partner of the top quark, the stop, at the LHC. Searches for SUSY at the TeV energy scale are motivated in part by its solution to the electroweak hierarchy problem, as outlined in Section 1.3. Because the top quark provides the largest correction to the Higgs mass due to its $\mathcal{O}(1)$ Yukawa coupling, it is anticipated that the stop should be among the lightest SM-charged SUSY particles in the spectrum. Experimental confirmation of the stop is therefore vital to confirming if SUSY indeed provides a solution to the electroweak hierarchy problem. The main body of this chapter has been reproduced from Ref. [161].

5.1 Introduction

While the discovery of the Higgs boson [162, 163] was a major success for the Standard Model, open theoretical questions remain. If the Higgs boson is an elementary scalar field, the stability of the electroweak scale against radiative corrections is not understood, since fields of this type receive quadratically divergent corrections to their mass-squared. Of the proposed solutions to this well known hierarchy problem, one of the best motivated is SUSY, where every SM fermion(boson) is complemented with a superpartner boson(fermion). Elementary scalar masses are protected because a cancellation occurs between the quadratically divergent correction coming from loops with SM particles and their corresponding superpartners enforced by the enlarged symmetry of the model. Nevertheless, SUSY must be broken in order to be consistent with non-observation of superpartners to date. This breaking lifts the superpartner masses to a relatively high scale set by the SUSY breaking sector and messenger mass [164, 165].

As the superpartners become more massive, the expected mass of elementary scalars goes up and fine-tuning is likely required to explain light scalars. Since the Higgs boson receives the largest correction to its mass from a loop involving top quarks, the most important SUSY particle for protecting the Higgs boson mass is the superpartner of the top quark–the top squark or stop [166, 167]. In the MSSM, the electroweak scale is dominantly set by stop masses and mixing, in addition to the tree level mass scales in the superpotential and soft SUSY breaking potential. Thus, the natural expectation is that the lightest third generation squarks should be observable at the Large Hadron Collider (LHC), since the mass scales that set the electroweak scale in the MSSM must not be too far away from the observed electroweak scale in order to avoid large amounts of fine tuning. While a considerable amount of natural MSSM parameter space has been excluded by the most recent results from the LHC [168, 169], viable regions remain, such as the compressed region [170–178]. These regions are likely difficult to achieve in a top down SUSY breaking model.

Here, we accept some fine tuning and focus on a new method to search for pair-produced stops with a mass near 1 TeV which decay to top quarks and light neutralinos, a scenario which has not yet been excluded by the LHC Run 2. We assume the neutralino to be the lightest supersymmetric particle (LSP) with a mass around 100 GeV, which also makes it a possible thermal relic weakly interacting massive particle (WIMP) dark matter candidate. The signal that our new method will be applicable to is $\bar{t}t + \not{E}_{\mathrm{T}}$ (see Ref. [179–184] for earlier studies of two hadronic tops), where the tops decay hadronically and the missing transverse energy $\not{E}_{\mathrm{T}}$ comes from the two neutralinos which leave the detector. Currently, for searches with two hadronic tops, the ATLAS collaboration has imposed a constraint which requires the stop mass to be above 820 GeV with 13.3 fb^{-1} of integrated luminosity, assuming 100% decay branching for the channel $\widetilde{t} \to t\,\widetilde{\chi}_0$ [185] and a light neutralino mass below around 200 GeV. Similarly, the CMS collaboration has obtained a limit of 860 GeV with 12.9 fb^{-1} data [186]. As the $\not{E}_{\mathrm{T}}$ cut is increased to optimize for heavier stops, it becomes increasingly likely that the two tops in the decay have a small angular separation and that the signals of their decay products overlap in the detectors.

We develop a new boosted top tagging procedure that recovers merged top jets, which we call "Merged Top Tagger." Our starting point is the well-known HEPTopTagger algorithm [179, 187]. Rather than simply trying to find a single combination of subjets in a fat jet that looks like a top, the algorithm searches through various combinatoric possibilities in an attempt to find a total of two top-like groups of subjets. Further sensitivity is gained by using the new information of both tops' kinematics to construct and cut on the M_{T2} variable [188]. Based on simulations we have performed, our strategy shows a 50% improvement in S/B and slight improvement in discovery sensitivity for 1.2 TeV stops decaying to tops and 100 GeV detector-stable neutralinos.

5.2 Motivation for Merged Top-Jets

For the region of parameter space with $m_{\widetilde{t}} - m_{\widetilde{\chi}_0} \gg m_t$, the top quark is boosted and the three partons from the top quark decay are collimated. In similar scenarios with boosted top quarks, both collaborations at the LHC have opted to reconstruct events using jet-substructure techniques such as top-tagging. Assuming conservation of R-parity, the two neutralinos in the final state will be stable and contribute significantly to the total missing transverse energy, $\not{E}_{\mathrm{T}}$. Because of this fact, imposing a large $\not{E}_{\mathrm{T}}$ cut is a very efficient way to increase the signal over background ratio. However, we find that imposing a large $\not{E}_{\mathrm{T}}$ cut isolates the sub-region of phase space of the signal where the neutralinos are approximately aligned to provide large $\not{E}_{\mathrm{T}}$, resulting in the tops (which recoil off the neutralino momenta) also being approximately aligned. Because the pair-produced stops are not very relativistic, the top and neutralino pairs end up approximately back to back. As a result, one should anticipate that a significant fraction of signal events will have geometric overlapping between the six partons from two hadronic tops, a scenario we call *merged top-jets*. The schematic picture of the region of phase space for signal events under discussion is shown in Fig. 24. The subject of this chapter will be a new search strategy for the merged top-jets case, with the goal of improving the discovery potential of stops at the LHC.

To quantitatively understand the fraction of signal events with two merged tops, we first study the signal events at the parton level. Throughout this chapter, we will assume benchmark masses of $m_{\widetilde{t}} = 1.2$ TeV and $m_{\widetilde{\chi}} = 100$ GeV, and $\mathrm{Br}(\widetilde{t} \rightarrow t + \widetilde{\chi}) = 100\%$. The lightest stop mass is chosen to be close to the reach of the LHC Run 2 with 100 fb^{-1}. In our simulation, we have the stop to be mainly right-handed, although our later kinematic analysis is insensitive to this choice (for the detailed analysis for left-handed and right-handed stops, see Ref. [189]). In the left panel of Fig. 25, we define a measure to demonstrate the alignment of the two tops as the cut on $\not{E}_{\mathrm{T}}$ is increased. To show this, we define $\Delta R_{\min,t\bar{t}}$ as the minimum geometrical separation among all pairs with one

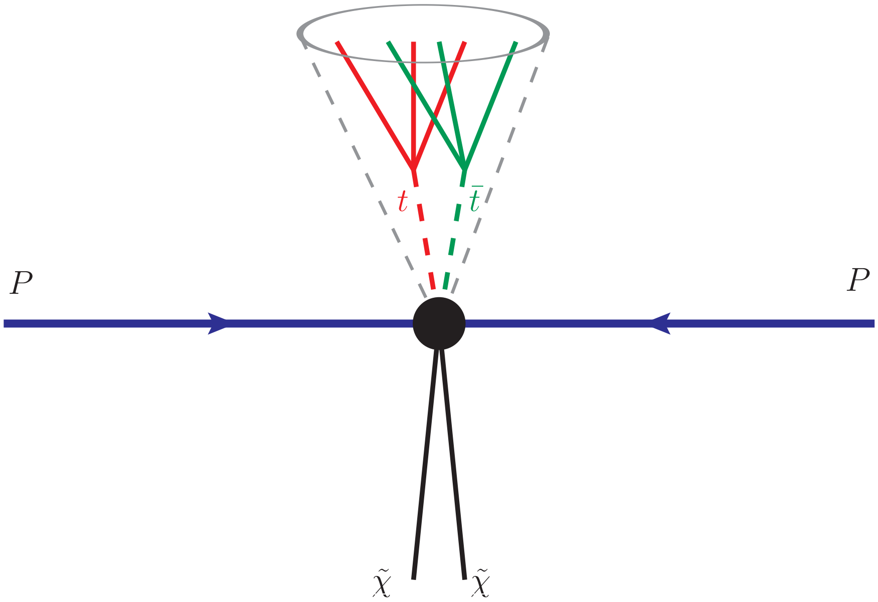

Figure 24: The schematic plot of the region of phase space for signal events with a large cut on $\not{E}_{\mathrm{T}}$. To provide large $\not{E}_{\mathrm{T}}$, the neutralino momenta must approximately align. This also results in alignment of the tops, which recoil off the sum of the neutralino momenta. When performing jet-substructure analysis with a large value of the jet clustering parameter R, the six partons from the two hadronic tops are likely to be included in a single fat jet.

parton from the top and one parton from the anti-top. Then we define $\max(\Delta R_{\max,tt}, \Delta R_{\max,\bar{t}\bar{t}})$ as the maximum separation among all pairs with two partons belonging only to the top or anti-top. The ratio of these two quantities, $\Delta R_{\min,t\bar{t}} \,/\, \max(\Delta R_{\max,tt}, \Delta R_{\max,\bar{t}\bar{t}})$, will be small when the smallest distance between one parton from the top and one parton from the anti-top is smaller than the largest distance between partons in the same top or anti-top, which is the aligned or merged scenario. As a result, we expect the event distribution of this measure to shift to smaller values as the cut on the missing transverse energy is increased, and this expectation is confirmed in the left panel of Fig. 25.

When two partons from the top and anti-top are geometrically close to each other, the standard jet-substructure analysis to tag boosted top-jets becomes problematic. This is because the large fat-jet analysis employed frequently fails to isolate the two tops in separate fat jets. To demonstrate this issue at parton level, we apply the Cambridge/Aachen clustering algorithm [190] with $R = 1.5$ to the signal events and count the number of partons belonging to the top or anti-top contained in

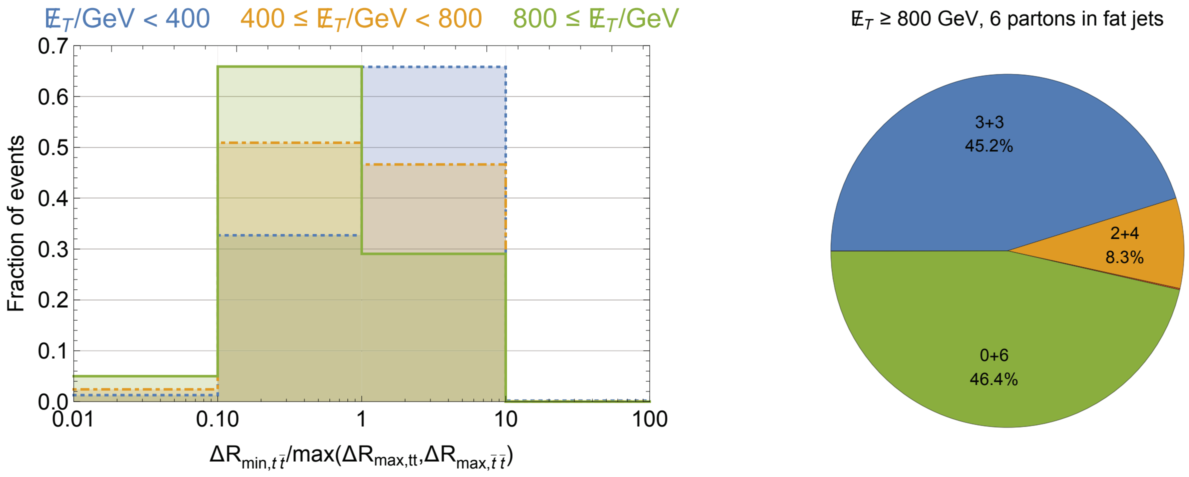

Figure 25: **Left panel:** The fraction of signal events as a function of a variable (see text for definition) which measures the overlapping of partons from the two tops: a smaller value means a larger overlap. **Right panel:** The distribution of partons in a $R = 1.5$ Cambridge/Aachen fat jet and $p_T > 200$ GeV. Not shown are the negligible fractions of events with 1+5 and 1+2+3.

each fat jet. In the right panel of Fig. 25, one can see that the fully merged 0+6 case (all partons in one fat jet) and the partially merged 2+4 case (2 partons in one fat jet, 4 partons in another) account for 54.7% of the events, with the separated 3+3 case accounting for 45.2% of the events. The 1+5 and 1+2+3 cases are extremely sub-dominant due to the fat jet definition including a transverse momentum cut of $p_T > 200$ GeV.

It is now clear that the standard jet-substructure analysis is not optimal for reconstructing our signal events after a large $\not{E}_{\rm T}$ cut, since standard top taggers (which assume well isolated tops by only searching for one top tag per fat jet) frequently fail to tag two tops in the fully or partially merged cases which constitute a majority of our signal events after a large $\not{E}_{\rm T}$ cut. To fully recover the signal kinematics and define additional transverse-mass variables like M_{T2}, it is important to resolve and tag the two top-jets with high efficiency. In next section of this chapter, we develop a search strategy based on the HEPTopTagger [179, 187] algorithm and check the improvement of signal over background after the particle-level simulations.

5.3 The Merged Top Tagger Algorithm

Having established our motivation for tagging two merged top-jets, we now develop a jet-substructure based algorithm to reconstruct both boosted hadronic tops for the signal and background. Our algorithm for tagging two merged top-jets is based on the existing top-tagging algorithm of HEPTopTagger in Ref. [179], although it can also be implemented using other top-tagging methods such as N-subjettiness [191]. Before discussing our algorithm, we briefly summarize the features of HEPTopTagger. By default, HEPTopTagger takes a single fat jet as an input, on which it will perform a mass drop [192] operation to obtain a list of the relevant hard substructure. It then iterates through all pairings of three hard subjets and filters [192] each triplet in order to define the triplet mass. It then keeps *only* the triplet which has a filtered mass closest to the top mass m_t. This single remaining triplet is then required to pass additional mass constraints which ensures the triplet does not behave like a QCD event and that it satisfies some top and W gauge boson mass constraints.

For our signal events, after a large $\not{E}_{\mathrm{T}}$ cut, the two top-jets have a significant probability of being merged, and the original HEPTopTagger algorithm becomes less efficient. This is because the original HEPTopTagger algorithm can find at most one top per fat jet, even in the case where the input fat jet contains two tops. Furthermore, even in the one top per fat jet case, the original algorithm will fail when the triplet with the best filtered mass fails the mass criteria, even though there may exist other triplets with filtered masses still not that far away from the top quark mass, but a better chance to pass all mass criteria. To address those issues, we introduce the following "Merged Top Tagger" algorithm with an aim to tag two merged top-jets:

1. Using the Cambridge/Aachen algorithm with $R = 1.5$, identify initial fat jets with $p_T(J) > 200$ GeV.

2. For the leading p_{T} fat jet, find all hard subjets using a mass drop criterion: when undoing the last clustering of the jet j, into two subjets j_1, j_2 with $m_{j_1} > m_{j_2}$, we require $m_{j_1} < 0.8\ m_j$ to keep j_1 and j_2. Otherwise, we keep only j_1. For each subjet j_i, we further de-cluster it

until its jet mass is 30 GeV or below.

3. Iterate through all pairings of three hard subjets (HSJ triplets) found in Step 2: first, filter them with resolution $R_{\text{filter}} = \min(0.3, \Delta R_{jk}/2)$. Next, use the five hardest filtered constituents and calculate the triplet mass m_{filtered} (for less than five filtered constituents use all of them). Keep all HSJ triplets which satisfy $m_{t_{\min}} < m_{\text{filtered}} < m_{t_{\max}}$ (Default: $m_{t_{\min}} = 140$ GeV and $m_{t_{\max}} = 250$ GeV).

4. For each HSJ triplet saved from Step 3, re-cluster the five filtered constituents into exactly three subjets j_1, j_2, j_3, ordered by p_{T}. If the masses (m_{12}, m_{13}, m_{23}) satisfy one of the following three criteria, save the filtered HSJ triplet as a top candidate:

$$
\begin{aligned}
&0.2 < \arctan\left(\frac{m_{13}}{m_{12}}\right) < 1.3 \qquad \text{and} \qquad R_{\min} < \frac{m_{23}}{m_{123}} < R_{\max}\,, \\
&R_{\min}^2\left[1+\left(\frac{m_{13}}{m_{12}}\right)^2\right] < 1-\left(\frac{m_{23}}{m_{123}}\right)^2 < R_{\max}^2\left[1+\left(\frac{m_{13}}{m_{12}}\right)^2\right] \qquad \text{and} \qquad \frac{m_{23}}{m_{123}} > 0.35\,, \\
&R_{\min}^2\left[1+\left(\frac{m_{12}}{m_{13}}\right)^2\right] < 1-\left(\frac{m_{23}}{m_{123}}\right)^2 < R_{\max}^2\left[1+\left(\frac{m_{12}}{m_{13}}\right)^2\right] \qquad \text{and} \qquad \frac{m_{23}}{m_{123}} > 0.35\,.
\end{aligned}
$$

   with $R_{\min} = (1 - f_W) \times M_W/m_t$ and $R_{\max} = (1 + f_W) \times M_W/m_t$ (we will choose the value $f_W = 0.5$ [193] to increase signal efficiencies). The number 0.35 is chosen to help remove QCD events. The above selection criteria are identical to HEPTopTagger [179].

5. If there is more than one top candidate from Step 4, check all two pairings of top candidates and keep any for which their HSJ triplets share no subjets (unique pairs). If only one unique pair is found, return it as two tagged tops. If more than one unique pair is found, return the pair of top candidates which minimizes the quantity $|m_{J_{1,\text{filtered}}} - m_t| + |m_{J_{2,\text{filtered}}} - m_t|$ as tagged tops. Otherwise, continue to Step 6.

Up to this point, the modified HEPTopTagger algorithm has only been extended to deal with the fully merged case when two tops are contained within a single fat jet. To deal with the partially merged case when some partons from the first top are clustered into the fat jet of the second top, we also introduce the following steps to capture particles in the vicinity of the leading fat jet, which we accomplish by removing the particles belong to the leading top candidate(s) and reclustering the event. Specifically, we extend the algorithm in the following way:

6. If at least one top candidate exists from Step 4, remove the particles associated with one top candidate from the final state particles. The remaining particles are then reclustered using the same Cambridge/Aachen algorithm with $R = 1.5$. For the leading p_{T} fat jet found after this reclustering (if any), repeat the above Steps 2-4 to identify more top candidates. Of all top candidates found in the reclustered fat jet, keep the one which has a filtered mass closest to m_t (if any), and pair it with the top candidate before the new reclustering procedure. For the cases with more than one top candidate from Step 4, perform this procedure on all of them, and return the pair which minimizes the quantity $|m_{J_{1,\mathrm{filtered}}} - m_t| + |m_{J_{2,\mathrm{filtered}}} - m_t|$ as tagged tops. If no top candidate pairs are found, continue to Step 7.
7. If the two leading p_{T} fat jets from the initial event clustering have not both already been analyzed, repeat Steps 2-6 on the next leading initial fat jet by p_{T}, if it exists. If no initial fat jets remain or if the two leading p_{T} initial fat jets have already been analyzed, then the algorithm has failed to tag two tops. Of all the top candidates from the leading p_{T} initial fat jet, return the one that minimizes $|m_{J_{\mathrm{filtered}}} - m_t|$ as a single tagged top. If there are no top candidates in the leading p_T initial fat jet, use the next leading p_T initial fat jet. If there are no top candidates in any initial fat jet, the algorithm has failed to tag a single top.

Not only does our modified algorithm allow two tops to be tagged in the fully and partially merged cases, it also finds the combination of hard subjets such that both tops are as close to the true top mass as possible. To quantify the improvement our algorithm offers for tagging merged top-jets, we define the following efficiency parameter

$$\mathcal{E}_{N_t \geq 2}\,(\not{E}_{\mathrm{T}}\,\mathrm{range}) \equiv \frac{\text{Events with} \geq 2 \text{ top tags in } \not{E}_{\mathrm{T}}\,\text{range}}{\text{All events in } \not{E}_{\mathrm{T}}\,\text{range}}\,, \tag{113}$$

which we can use to gauge the relative performance of our modified algorithm versus the original HEPTopTagger algorithm over different ranges of missing transverse energy. According to our

	Signal		$\bar{t}t+\text{jets}$		$\bar{t}t+Z$	
Algorithm	$\not{E}_{\mathrm{T}} > 400$ GeV	$\not{E}_{\mathrm{T}} > 800$ GeV	$\not{E}_{\mathrm{T}} > 400$ GeV	$\not{E}_{\mathrm{T}} > 800$ GeV	$\not{E}_{\mathrm{T}} > 400$ GeV	$\not{E}_{\mathrm{T}} > 800$ GeV
Original	18%	14%	6.0%	7.1%	8.4%	11%
Modified	48%	55%	18%	26%	23%	41%
Ratio	2.6	3.9	3.0	3.6	2.8	3.6

Table 12: The efficiencies, $\mathcal{E}_{N_t \geq 2}$, to tag two top-jets using the original HEPTopTagger and our Merged Top Tagger. The signal events have $m_{\tilde{t}} = 1.2$ TeV and $m_{\tilde{\chi}} = 100$ GeV. Only the dominant backgrounds are shown here for comparison.

hypothesis, a larger cut on $\not{E}_{\mathrm{T}}$ should increase the number of merged top signal events, pushing more signal events into the region where the original algorithm cannot tag two tops. As a result, we expect the ability of the modified algorithm to tag two tops to increase relative to the original algorithm for higher missing energy windows, an expectation which is confirmed in Table 12. Also shown in Table 12 are the two top-tagging efficiencies for the two leading backgrounds, $\bar{t}t+\text{jets}$ (one hadronic top and one leptonic top) and $\bar{t}t+Z$ (two hadronic tops, Z decays to two neutrinos). Having discussed the tagging efficiency for our new algorithm, we turn now to estimate the improvement for the signal over background ratio and the signal discovery significance.

5.4 Estimation of Discovery Significance

In this section, we estimate the discovery sensitivity of stops in the fully-hadronic channel at the LHC Run 2 with 100 fb^{-1}. The details of our numerical simulations are presented in Appendix C.1. After the application of a large cut on missing transverse energy, we find the leading backgrounds are $\bar{t}t+\text{jets}$ (one leptonic top and one hadronic top) and $\bar{t}t+Z$ (two hadronic tops, Z decays to two neutrinos). The basic cuts to select events impose the following requirements:

(a) Missing energy $\not{E}_{\mathrm{T}} > 400$ GeV.

(b) Using our modified algorithm, require at least two top-tagged jets with $p_{\mathrm{T}}(J) > 200$ GeV.

(c) At least two anti-k_{T}, $R = 0.4$ b-tagged jets with p_{T} above 30 GeV.

(d) Veto events with isolated leptons with $p_{\mathrm{T},\ell} > 15$ GeV and $|\eta_\ell| < 2.4$.

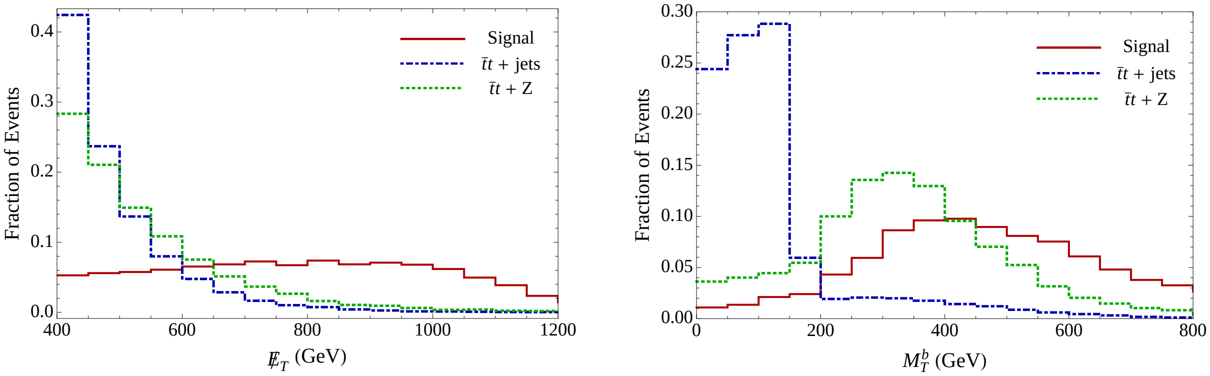

Figure 26: **Left panel:** The normalized event distributions in $\not{E}_{\mathrm{T}}$ for the signal and leading backgrounds after basic cuts. **Right panel:** Same as the left but in terms of M_{T}^b. The signal has $m_{\tilde{t}} = 1.2$ TeV and $m_{\tilde{\chi}} = 100$ GeV.

For simplicity, we have implemented a b-tagging efficiency of 0.8 (mistag efficiency of 0.2 for charm quarks and 0.05 for light quarks and gluon) [185, 194] in our simulation. One could also perform direct b-tagging on the subjets of the fat jets as in Ref. [193]. Here, the main requirement of our simplistic and conservative b-tagging approach is to sufficiently reduce the $W/Z+$jets backgrounds by requiring two b-tags in the event.

After the basic cuts, we note two powerful kinematical variables which are useful for reducing backgrounds. The most obvious one is $\not{E}_{\mathrm{T}}$, which is shown in the left panel of Fig. 26. The other variable is the transverse mass associated with the b-jets and $\not{E}_{\mathrm{T}}$, which has already been adopted by both CMS [186] and ATLAS [185]. It is given by

$$M_{\mathrm{T}}^b = \min\left[M_{\mathrm{T}}(\vec{p}_{b_1}, \vec{\not{E}}_{\mathrm{T}}), M_{\mathrm{T}}(\vec{p}_{b_2}, \vec{\not{E}}_{\mathrm{T}})\right] . \tag{114}$$

The transverse mass is defined as $M_{\mathrm{T}}(\vec{p}_{b_i}, \vec{\not{E}}_{\mathrm{T}}) = 2p_{\mathrm{T}}^{b_i}\,\not{E}_{\mathrm{T}}[1 - \cos(\phi_{b_i} - \phi_{\not{E}_{\mathrm{T}}})]$, where ϕ_{b_i} and $\phi_{\not{E}_{\mathrm{T}}}$ are the azimuthal angles of the b-jet and $\vec{\not{E}}_{\mathrm{T}}$. In the right panel of Fig. 26, we show the signal and background distributions for this variable. As one can see, the $\bar{t}t+$jets background has an endpoint around the top quark mass, so requiring a sufficiently large M_{T}^b can dramatically reduce this background. We also note that the tail of the M_{T}^b distribution for $\bar{t}t+$jets comes from mistagged b-jets, which do not come from top quark decays and therefore are not subject to this

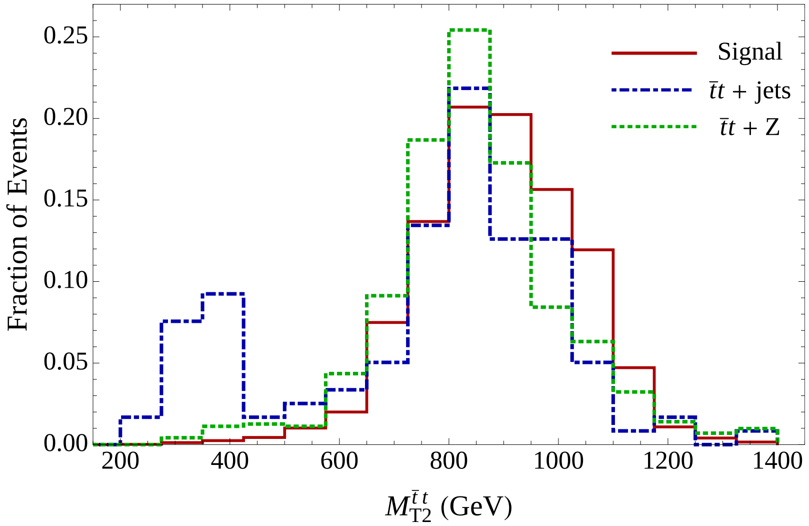

Figure 27: Distributions for $M_{\mathrm{T2}}^{\bar{t}t}$ after the optimized cuts of $\not{E}_{\mathrm{T}} > 800$ GeV and $M_{\mathrm{T}}^{b} > 240$ GeV for a 1.2 TeV stop mass.

kinematic cutoff.

With our new tagging algorithm, one can define additional kinematic variables based on the two top quarks in the final state. With the large missing transverse energy at hand, one natural choice is the M_{T2}-like variable. Specifically for events with two tops and missing transverse energy, one can define the following $M_{\mathrm{T2}}^{\bar{t}t}$ variable as [188, 195, 196]

$$M_{\mathrm{T2}}^{\bar{t}t} = \min\left\{ \bigcup_{\vec{p}_{\mathrm{T}}^{1}+\vec{p}_{\mathrm{T}}^{2}=\vec{\not{p}}_{\mathrm{T}}} \max\left[M_{\mathrm{T}}(\vec{p}_{t_1}, \vec{p}_{\mathrm{T}}^{1}), M_{\mathrm{T}}(\vec{p}_{t_2}, \vec{p}_{\mathrm{T}}^{2}) \right] \right\} . \tag{115}$$

In Fig. 27, we show the distribution for $M_{\mathrm{T2}}^{\bar{t}t}$ for both the signal and leading backgrounds. The signal event distribution has a peak feature with an end-point of around 1.2 TeV, which can be easily understood from the stop mass and the large missing energy cut of $\not{E}_{\mathrm{T}} > 800$ GeV. The $\bar{t}t + Z$ background has a similar distribution to the signal events and behaves as an irreducible background. For the $\bar{t}t$ + jets background, two peak structures appear in the distribution. The peak at higher values is similar to the signal region of phase space with two top-jets moving in the same direction, while the peak at lower values is due to the region of phase space where one top-jet

Modified top-tagging	after basic cuts	$\not\!\!E_{\mathrm{T}} > 800$ GeV	$M_{\mathrm{T}}^{b} > 240$ GeV	$M_{\mathrm{T2}}^{\bar{t}t} > 500$ GeV	events (100 fb^{-1})
signal	0.17 fb	0.084 fb	0.081 fb	0.080 fb	8.0
$\bar{t}\,t$ + jets	4.66 fb	0.090 fb	9.8×10^{-3} fb	7.8×10^{-3} fb	0.78
$\bar{t}\,t + Z$	0.17 fb	0.010 fb	9.1×10^{-3} fb	8.8×10^{-3} fb	0.88
Z + jets	0.024 fb	1.3×10^{-3} fb	1.0×10^{-3} fb	1.0×10^{-3} fb	0.1
W + jets	6.4×10^{-3} fb	0.2×10^{-3} fb	0.2×10^{-3} fb	0.2×10^{-3} fb	0.02
					$S/B = 4.5$ $\sigma_{\mathrm{LL}} = 4.2$

Table 13: Signal and background cross sections after cuts using our modified algorithm at the $\sqrt{s} = 13$ TeV LHC. The choice of cuts is optimized to increase σ_{LL} in Eq. (116). Here, we have $m_{\widetilde{t}} = 1.2$ TeV and $m_{\widetilde{\chi}} = 100$ GeV.

approximately aligns with the missing transverse momentum, leading to a smaller transverse mass. Imposing a lower limit cut on $M_{\mathrm{T2}}^{\bar{t}t}$ can therefore reduce the $\bar{t}t$ + jets background.

Using the kinematic variables outlined above, we perform an optimization of cuts to increase the expected signal discovery significance. Since we expect small numbers of signal and background events, we use the following expected log likelihood discovery significance

$$\sigma_{\mathrm{LL}} \equiv \sqrt{-2\left[S + (B+S)\log\frac{B}{B+S}\right]}\,, \tag{116}$$

which approaches $S/\sqrt{B}$ for large signal and background. After optimizing the cuts on the three variables $\not\!\!E_{\mathrm{T}}$, M_{T}^{b} and $M_{\mathrm{T2}}^{\bar{t}t}$, we show the cut-flow of events in Table 13, which shows that requiring two top-jets from our modified tagging algorithm along with the rest of the basic cuts already reduces the dominant $\bar{t}t$ + jets background substantially. The cuts on $\not\!\!E_{\mathrm{T}}$ and M_{T}^{b} are still the most efficient for increasing S/B. As a result, large values of S/B and σ_{LL} are obtained. The chosen model parameter with $m_{\widetilde{t}} = 1.2$ TeV and $m_{\widetilde{\chi}} = 100$ GeV will be tested at the LHC Run 2 with 100 fb^{-1}.

To compare to a search using the original HEPTopTagger algorithm, we replace part (b) of the basic cuts by

Original top-tagging	after basic cuts	$\not{E}_T > 800$ GeV	$M_T^b > 260$ GeV	events (100 fb^{-1})
signal	0.24 fb	0.11 fb	0.10 fb	10.0
$\bar{t}t$ + jets	13.6 fb	0.19 fb	0.0174 fb	1.74
$\bar{t}t + Z$	0.443 fb	0.016 fb	0.014 fb	1.35
Z + jets	0.164 fb	3.2×10^{-3} fb	1.6×10^{-3} fb	0.16
W + jets	0.047 fb	1.2×10^{-3} fb	0.6×10^{-3} fb	0.06
				$S/B = 3.0$ $\sigma_{\text{LL}} = 4.1$

Table 14: The same as Table 13 but based on the original HEPTopTagger algorithm.

(b′) Require at least one top-tagged jet with $p_T(J) > 200$ GeV based on the original HEPTopTagger algorithm,

and show the cut-flow of signal and backgrounds in Table 14. Comparing the results from Table 13 and Table 14, one can see that our modified top-tagging algorithm yields an obvious improvement for S/B and a mild increase for σ_{LL}.

5.5 Discussion

We note that the signal acceptance obtained when requiring two top tagged jets is not that high compared to the original HEPTopTagger algorithm with the requirement of only one top tagged jet. This is simply due to the fact that a non-negligible fraction of top quarks from 1.2 TeV stop decays are not boosted. These events can have the partons from top decays well separated from each other. For instance, the b-hadron could be well separated from the hadronic W and may not have enough transverse momentum to satisfy the fat jet $p_T > 200$ GeV requirement. In principle, one could include those events with an ordinary b-jet that does not belong to any fat jet. With a simple implementation, we have found the signal acceptance can be further increased by around 13% with a slightly smaller value of $S/B = 4.4$, but slightly larger value of $\sigma_{\text{LL}} = 4.4$. If one wants to further increase the discovery sensitivity, one should combine events with boosted and non-boosted top quarks [186].

In addition, our algorithm should be validated with a full detector simulation before use. The simplified approach to detector effects, as well as to b-tagging, adopted in this work is justified by the fact that the dominant smearing of jet kinematics is coming from QCD physics, but there is some effect of calorimetric smearing as well. Our work demonstrates the gains to be had by adopting our algorithm even neglecting these effects and knowing that the final projections for discovery sensitivity are an estimation.

In this chapter, we have concentrated on simplified models with stops and neutralinos. However, the key observation illustrated in Fig. 24 is general and could be applied to other models, under the condition that a sizeable cut on the missing transverse energy prefers to have the visible particles collimated. One possible example is pair-produced gluinos with off-shell squark mediated decay, $\widetilde{g} \to jj\widetilde{\chi}_0$. The four jets in the final state could merge into a single fat jet after a sufficiently large cut on $\not{E}_{\mathrm{T}}$. A similar jet-substructure based analysis is therefore ideal to improve the signal discovery significance.

In summary, we have identified a new and interesting region of phase space for the heavy stop plus light neutralino model. The subset of signal events with large missing transverse momentum has a region of phase space where the partons coming from the decay of the two hadronic top quarks have a large overlapping. We have developed a jet-substructure based algorithm to identify these two merged or semi-merged hadronic tops. Based on our estimation of signal discovery significance with only statistical errors, we have found that our algorithm can dramatically increase S/B by 50% and yield a mild increase in the discovery significance. It is also important to point out that our new algorithm is ideal for use with additional kinematic variables which require the complete reconstruction of the two hadronic top momenta to further increase S/B and the discovery significance. A stop mass of 1.2 TeV and a light neutralino will be concretely tested at the LHC Run 2 with 100 fb^{-1}.

6 Conclusion

In this dissertation, we have examined the phenomenological consequences of strong dynamics within the frameworks of QCD and BSM physics. From a model of the low-energy QCD effective potential, we determined that an undetected bound state of $bb\overline{b}\overline{b}$ heavy quarks is predicted to exist with a mass of 18.69 ± 0.03 GeV and with a detectable decay mode of $0^{++} \to \Psi(1S)\Psi(1S)^* \to \ell^+\ell^-\ell^+\ell^-$. Separately, we examined the potential to observe dark matter interacting via QCD gluons at the LHC within the context of effective field theory. An important distinction is made in that the effective operator description of such interactions is likely to break down at the energy scales probed at the 8 TeV LHC, which is even more crucial to the current LHC energy scale of 13 TeV. Our conclusion that UV-completions of such operators lead to vastly different discovery modes is still relevant for current searches in an expanded dark matter program at the LHC.

We next examined a class of BSM physics models that includes a new unbroken $SU(N)$ gauge group. We point out that in many non-supersymmetric models of BSM physics, vector-like masses, while natural, are likely to be fine-tuned without a symmetry protecting them like the chiral symmetry of the Standard Model. To examine the consequences of this new symmetry, we introduced an additional $U(1)'$ gauge group. Like the QCD pions, one of the first signatures of such models could be a resonance to two gauge bosons. The chiral symmetry breaking structure predicts a rich spectrum of new particles, and searching for a heavy Z' gauge boson with an enhanced leptonic branching fraction can distinguish this class of models from others. Finally, within the framework of SUSY we examined the current searches for stops and found that in the heavy mass regime new search strategies are likely to be needed. By identifying a significant regime of phase space with a final state of two merged top-jets and large missing transverse energy, we presented a new algorithm to identify merged tops which lead to an increase in discovery potential for heavy stops.

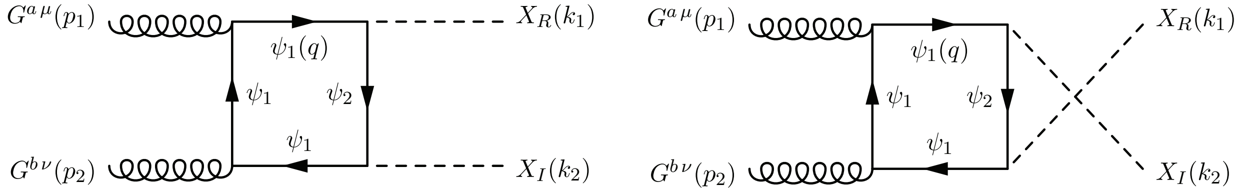

Figure 28: Loop diagrams for generating $\mathcal{O}_2^{\text{cRayleigh}}$ via a colored particle in loop..

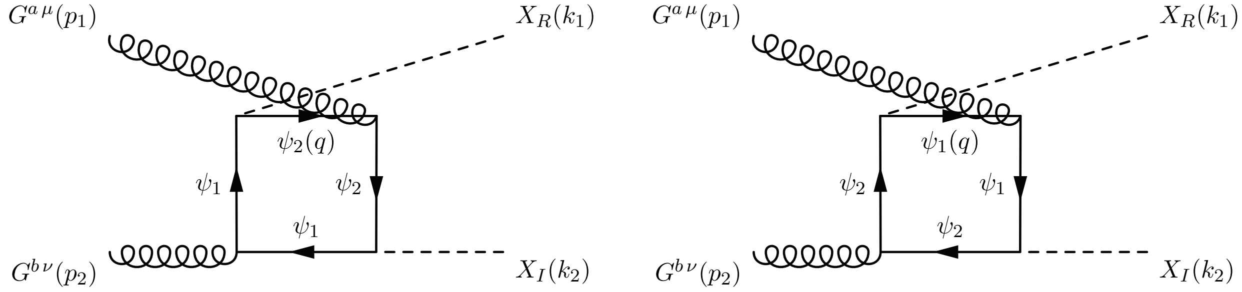

Figure 29: Loop diagrams for generating $\mathcal{O}_2^{\text{cRayleigh}}$ via a colored particle in loop..

A Chromo-Rayleigh Dark Matter

A.1 Loop Level Calculations for the Coefficient of $\mathcal{O}_2^{\text{cRayleigh}}$

Starting from the Lagrangian in Eq. (67), we match the coefficient for $\mathcal{O}_2^{\text{cRayleigh}}$ at one-loop level. Other than the two Feynman diagrams in Fig. 13, we also have another four diagrams in Fig. 28 and Fig. 29.

Summing the two diagrams in Fig. 13, we have the matrix element as

$$\begin{aligned} i\mathcal{M}_1 =& 4ig_s^2 y_1 y_2 \mathrm{Tr}[t^a t^b]\varepsilon_\mu(p_1)\varepsilon_\nu(p_2) \\ &\times \int \frac{d^4q}{(2\pi)^4} \frac{\mathrm{Tr}[(\not{q}+m_2)\gamma^\mu(\not{q}-\not{p}_1+m_2)\gamma^\nu(\not{q}-\not{k}_1-\not{k}_2+m_2)\gamma^5(\not{q}-\not{k}_1+m_1)]}{[q^2-m_2^2][(q-p_1)^2-m_2^2][(q-k_1-k_2)^2-m_2^2][(q-k_1)^2-m_1^2]}\,. \end{aligned} \tag{117}$$

In the heavy fermion limit, we have a simplified version of the matrix element as

$$i\mathcal{M}_1 = i\,\frac{g_s^2 y_1 y_2}{4\pi^2}\delta^{ab}\varepsilon_\mu(p_1)\varepsilon_\nu(p_2)\epsilon^{\mu\nu\rho\sigma}p_{1\rho}p_{2\sigma}\left[\frac{-m_1^5 + 2m_1^3 m_2^2 \log\left(m_1^2/m_2^2\right) + m_1 m_2^4}{m_2(m_1^2 - m_2^2)^3}\right]. \tag{118}$$

The two diagrams in Fig. 28 have a similar answer as $i\mathcal{M}_2 = i\mathcal{M}_1(m_1 \leftrightarrow m_2)$. The two digrams in Fig. 29 has a summed matrix as

$$i\mathcal{M}_3 = i\frac{g_s^2 y_1 y_2}{2\pi^2}\delta^{ab}\varepsilon_\mu(p_1)\varepsilon_\nu(p_2)\epsilon^{\mu\nu\rho\sigma}p_{1\rho}p_{2\sigma}\left\{\frac{m_1 m_2\left[2(m_1^2 - m_2^2) - (m_1^2 + m_2^2)\log\left(m_1^2/m_2^2\right)\right]}{(m_1^2 - m_2^2)^3}\right\}. \tag{119}$$

Add all diagrams together, we have the summed matrix element

$$i\mathcal{M}_1 + i\mathcal{M}_2 + i\mathcal{M}_3 = \frac{g_s^2 y_1 y_2}{4\pi^2\, m_1\, m_2}\delta^{ab}\varepsilon_\mu(p_1)\varepsilon_\nu(p_2)\epsilon^{\mu\nu\rho\sigma}p_{1\rho}p_{2\sigma}\,. \tag{120}$$

To match to the coefficient of $\mathcal{O}_2^{\rm cRayleigh}$, one has

$$\frac{\alpha_s\, y_1 y_2}{\pi\, m_1\, m_2} = \frac{2\,\alpha_s}{\pi\,\Lambda_2^2}\,. \tag{121}$$

B Chiral Composite Model

B.1 Light Elementary Scalar Field

The model presented above includes a chiral symmetry-breaking scalar whose mass is expected to be out of reach of near-future experiments. Here we present a brief discussion of models where the real component of the scalar φ field is light. The strong $SU(N_b)$ is demoted to a global flavor symmetry, and $m_\varphi^2 < 0$ such that the scalar field develops a non-zero VEV via the Higgs mechanism. For $\lambda_{\varphi h} = 0$, we have

$$\langle\varphi\rangle \equiv \frac{v_\varphi}{\sqrt{2}} = \sqrt{-\frac{m_\varphi^2}{2\lambda_\varphi}}\,. \tag{122}$$

Expanding about the minimum, $\varphi = (v_\varphi + \phi_R + i\phi_I)/\sqrt{2}$, the imaginary component ϕ_I is eaten by the Z' gauge boson and the remaining scalar degree of freedom has mass

$$m_{\phi_R} = \sqrt{\frac{\lambda_\varphi v_\varphi^2}{2}} = \sqrt{-\frac{m_\varphi^2}{2}}\,. \tag{123}$$

We set the real scalar ϕ_R to be at the benchmark mass of 1.5 TeV, and require a cross section $\sigma(pp \to \phi_R \to \gamma\gamma) \simeq 0.1$ fb. The gluon fusion production cross section is given by

$$\hat{\sigma}(gg \to \phi_R) \approx \frac{N_b^2 \alpha_s^2}{72\sqrt{2}\pi}\,\frac{m_{\phi_R}^2}{v_\varphi^2}\,\delta(\hat{s} - m_{\phi_R}^2)\,, \tag{124}$$

and the branching fraction to two photons is approximately $\mathrm{Br}(\phi_R \to \gamma\gamma) \approx 2\alpha^2/3\alpha_s^2 = 4 \times 10^{-3}$. Using the MSTW2008 NLO PDFs [152] and including a K-factor of 2.5, we find the diphoton production cross section to be

$$\sigma(pp \to \phi_R \to \gamma\gamma) \approx 0.73 \text{ fb} \times \left(\frac{1 \text{ TeV}}{v_\varphi}\right)^2 \left(\frac{N_b}{4}\right)^2\,. \tag{125}$$

Requiring a phenomenologically-motivated cross section of 0.1 fb, we anticipate $v_\varphi \sim 2 - 3$ TeV for $N_b = 3 - 5$.

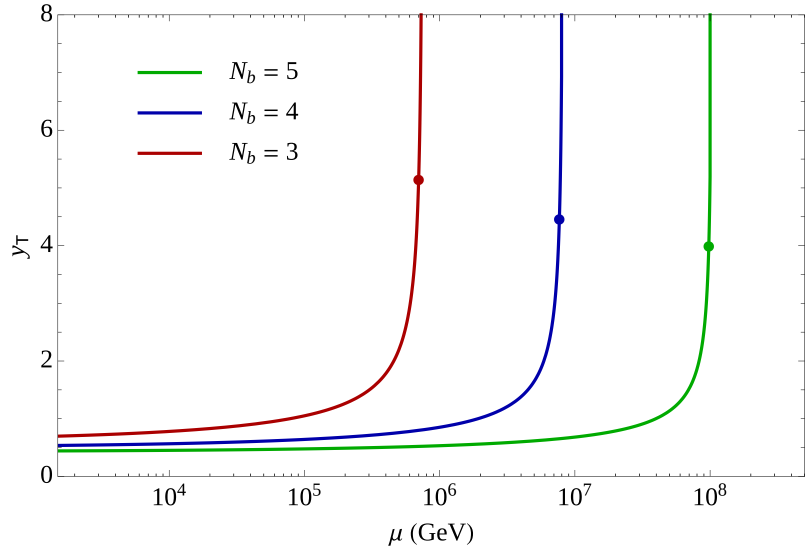

Figure 30: One loop runnings of $y_{\rm T}$ for the elementary scalar model, for $y^T(1.5\ \text{TeV}) = y^D(1.5\ \text{TeV})$. The dots show the approximate value at which the Yukawa couplings become non-perturbative.

The bare fermion masses are given by $m_{\psi_{1,2}} = y_{1,2}\, v_\varphi/\sqrt{2}$. The strongest bounds come from the QCD triplet masses, which are constrained to be $m_{\psi^{\rm T}} \gtrsim 1$ TeV [197] for $\psi^{\rm T}$ mixed with the bottom quark. For $N_b = 4$ and $y_1^{\rm T,D} = y_2^{\rm T,D} \equiv y_{\rm T,D}$, this requires a Yukawa coupling $y_{\rm T} \gtrsim 0.5$. Requiring these relatively large Yukawa couplings at m_ψ leads to Landau poles below the GUT scale in models with our matter content. For $N_b = 4$, the coupling becomes non-perturbative ($y > 4\pi/\sqrt{2N_b}$) at $\mathcal{O}(10^7$ GeV). Fig. 30 shows the Yukawa coupling running for $N_b = 3, 4, 5$.

Furthermore, the tree level coupling $\phi_R Z' Z'$ will dominate the decay processes unless it is kinematically forbidden, which provides the additional constraint $m_{Z'} > m_{\phi_R}/2$. The Z' mass is given by

$$m_{Z'} = g'\,|q_1 - q_2|\,v_\varphi = g'\,|q_1 - q_2|\sqrt{-\frac{m_\varphi^2}{\lambda_\varphi}}\,. \qquad (126)$$

For $N_b = 4$, this suggests values of the $U(1)'$ gauge coupling of $g'\,|q_1 - q_2| \gtrsim 0.28$ at m_{ϕ_R}.

B.2 $U(1)'$ Gauge Coupling Running

The one-loop beta function for the $U(1)'$ gauge coupling running is

$$\frac{dg'}{d\log\mu} \equiv \beta(g') = \frac{g'^3}{16\pi^2}\left[\frac{1}{3}\sum_s q_s^2 + \frac{2}{3}\sum_f q_f^2\right], \tag{127}$$

for complex scalars s and Weyl fermions f. For the matter content given in Table 5, we have

$$\beta(g') = \frac{g'^3}{16\pi^2}\left[\frac{1}{3}(q_1 - q_2)^2 + 5\,N_b\,\frac{2}{3}(2\,q_1^2 + 2\,q_2^2)\right]. \tag{128}$$

Solving this equation, we find

$$\frac{1}{g'^2(M_{\rm GUT})} = \frac{1}{g'^2(\mu)} - \frac{1}{8\pi^2}\left[\frac{1}{3}(q_1 - q_2)^2 + \frac{20N_b}{3}(q_1^2 + q_2^2)\right]\log\left(\frac{M_{\rm GUT}}{\mu}\right). \tag{129}$$

To have the Landau pole occur at or below $M_{\rm GUT} \approx 3 \times 10^{16}$ GeV, we need to have (for $q_1 = 1$ and $q_2 = 0$)

$$g'(1\ \text{TeV}) \lesssim \frac{2.76}{\sqrt{1 + 20\,N_b}}, \tag{130}$$

which is

$$g'(1\ \text{TeV}) \lesssim (0.35, 0.31, 0.28) \qquad \text{for} \quad N_b = (3, 4, 5)\,. \tag{131}$$

B.3 Doublet and Triplet Yukawa Coupling Running

The beta functions for the doublet and triplet Yukawa couplings are

$$\mu^2\frac{dy_{\rm T}}{d\mu^2} = \frac{y_{\rm T}}{16\pi^2}\left[\frac{3}{4}y_{\rm T}^2 + \frac{N_f}{2}(3y_{\rm T}^2 + 2y_{\rm D}^2) - 3C_3^{\rm F}\,g_s^2\right], \tag{132}$$

$$\mu^2\frac{dy_{\rm D}}{d\mu^2} = \frac{y_{\rm D}}{16\pi^2}\left[\frac{3}{4}y_{\rm D}^2 + \frac{N_f}{2}(3y_{\rm T}^2 + 2y_{\rm D}^2) - 3C_2^{\rm F}\,g_2^2\right], \tag{133}$$

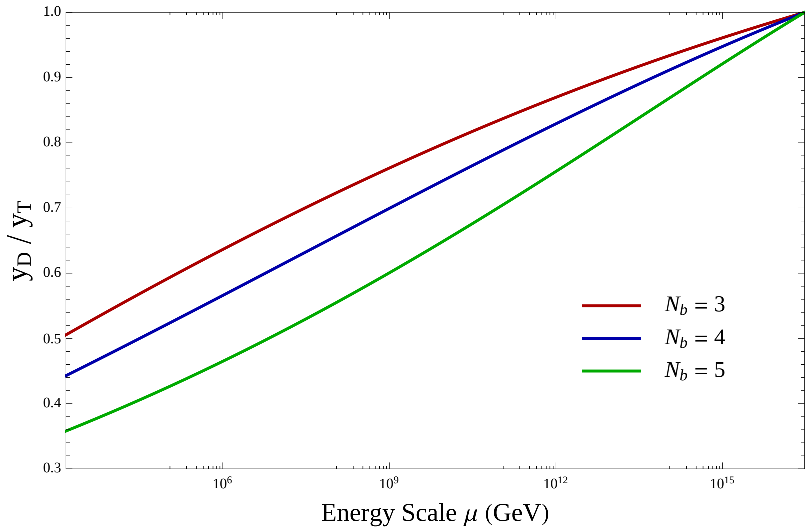

Figure 31: The running of $y_{\rm D}/y_{\rm T}$ as a function of energy scale μ. Boundary condition is chosen to be $y_{\rm D}(\Lambda_{\rm GUT})/y_{\rm T}(\Lambda_{\rm GUT}) = 1$ with $\Lambda_{\rm GUT} \approx 3 \times 10^{16}$ GeV.

where $N_f = 2N_b$; $C_3^{\rm F} = 4/3$ is the quadratic Casimir of $SU(3)_c$; $C_2^{\rm F} = 3/2$ is the quadratic Casimir of $SU(2)_W$; the sub-leading gauge interactions are neglected. We impose the GUT scale boundary condition that $y_{\rm D}(\Lambda_{\rm GUT}) = y_{\rm T}(\Lambda_{\rm GUT}) = y_0$. However, the running of the ratio $\mathcal{R}_y \equiv y_{\rm D}/y_{\rm T}$ is nearly independent of the value of y_0. To see this, we re-write the differential equations for $y_{\rm T}$ and $y_{\rm D}$ in terms of $\mathcal{R}_y$ and $y_{\rm T}$ as follows

$$\mu^2 \frac{d\mathcal{R}_y}{d\mu^2} = \frac{\mathcal{R}_y}{16\pi^2}\left[\frac{3}{4}\, y_{\rm T}^2(\mathcal{R}_y^2 - 1) + 3(C_3^{\rm F}\, g_s^2 - C_2^{\rm F}\, g_2^2)\right], \tag{134}$$

$$\mu^2 \frac{dy_{\rm T}}{d\mu^2} = \frac{y_{\rm T}}{16\pi^2}\left[\frac{3}{4} y_{\rm T}^2 + \frac{N_f}{2}\, y_{\rm T}^2(3 + 2\mathcal{R}_y^2) - 3C_3^{\rm F}\, g_s^2\right], \tag{135}$$

where the new GUT scale boundary conditions are $\mathcal{R}_y(\Lambda_{\rm GUT}) = y_{\rm D}(\Lambda_{\rm GUT})/y_{\rm T}(\Lambda_{\rm GUT}) = 1$ and $y_{\rm T}(\Lambda_{\rm GUT}) = y_0$. We see that the initial running for $\mathcal{R}_y$ does not depend on the value of y_0; it is determined only by the GUT scale gauge couplings. Numerical integration of these equations is shown in Fig. 31. The numerical values for $y_{\rm D}/y_{\rm T}$ at $\mu = 1.5$ TeV are shown in Table 15. Additionally, to avoid a Landau pole at or before $\mu = \Lambda_{\rm GUT} \sim 3 \times 10^{16}$ GeV, we require

$$y_{\rm T}(\mu = 1.5\,{\rm TeV}) < (0.54, 0.50, 0.49) \qquad (N_b = 3, 4, 5)\,. \tag{136}$$

N_b	3	4	5
$\frac{y_{\rm D}}{y_{\rm T}}(\mu = 1.5\,{\rm TeV})$	0.51	0.44	0.36

Table 15: Numerical values for the ratios of the doublet and triplet Yukawa couplings at $\mu = 1.5$ TeV generated from a GUT scale boundary condition of $y_{\rm D}(\Lambda_{\rm GUT})/y_{\rm T}(\Lambda_{\rm GUT}) = 1$.

B.4 Z' Kinetic Mixing and Decay

Gauge Kinetic Mixing

To leading order in the gauge kinetic mixing parameter χ, the process of diagonalizing the field strengths, and then resulting gauge boson mass terms after all symmetry breaking yields the following linear combinations for the gauge bosons [198]

$$\hat{A}_\mu = A_\mu - \chi\, c_W \sin\xi\, Z_\mu - \chi\, c_W \cos\xi\, Z'_\mu\,, \tag{137}$$

$$\hat{Z}_\mu = (\cos\xi + \chi\, s_W \sin\xi)\, Z_\mu + (\chi\, s_W \cos\xi - \sin\xi)\, Z'_\mu\,, \tag{138}$$

$$\hat{Z}'_\mu = \sin\xi\, Z_\mu + \cos\xi\, Z'_\mu\,, \tag{139}$$

where

$$\tan 2\xi = \frac{2\,\chi\, s_W}{1 - (\hat{m}_{Z'}/\hat{m}_Z)^2}\,. \tag{140}$$

Decay of the Z' Gauge Boson to Standard Model Fermions

After diagonalization of the gauge boson kinetic and mass terms, we find that the Z' gauge boson has a milli-charge coupling to the SM neutral current, given as

$$\mathcal{L}_N = \frac{g_2}{\cos\theta_W}\left[\Theta_{ZZ'}\, J_3^\mu + (s_W\, c_W\, \Theta_{AZ'} - s_W^2\, \Theta_{ZZ'})\, J_{\rm EM}^\mu\right] Z'_\mu\,, \tag{141}$$

with

$$\Theta_{AZ'} = -\chi\, c_W \cos\xi\,, \qquad\qquad \Theta_{ZZ'} = \chi\, s_W \cos\xi - \sin\xi\,. \tag{142}$$

Inserting the Standard Model fermion current, the part of the Lagrangian relevant for Z' decay can be cast in a familiar form

$$\mathcal{L}_N \supset \frac{g_2}{2\,c_W}\bar{\psi}\gamma^\mu(\mathcal{E}_V - \mathcal{E}_A\gamma^5)\psi\, Z'_\mu\,, \tag{143}$$

with the vector and axial milli-couplings defined as

$$\mathcal{E}_V = (T^3 - 2Qs_W^2)\,\Theta_{ZZ'} + 2Q\, s_W\, c_W\Theta_{AZ'}\,, \qquad\qquad \mathcal{E}_A = T^3\,\Theta_{ZZ'}\,. \tag{144}$$

From this, we find that the Z' decay width to Standard Model fermions is

$$\Gamma(Z' \to \bar{\psi}\psi) = \frac{g_2^2}{48\pi\, c_W^2}\left(\mathcal{E}_V^2 + \mathcal{E}_A^2\right) m_{Z'}\,. \tag{145}$$

Decay of the Z' Gauge Boson to Zh and W^+W^-

If the Z' gauge boson is heavy enough, there are also decay channels for $Z' \to Z\,h$ and $Z' \to W^+W^-$. The decay to Zh comes from the hZZ vertex in the Standard Model, which has a coupling of $g_{hZZ} = m_Z^2/v_{\mathrm{EW}}$, where $v_{\mathrm{EW}} = 246$ GeV is the electroweak VEV. After diagonalization of the gauge boson kinetic and mass terms, we have the following term in the Lagrangian

$$\mathcal{L}_h \supset g_{hZZ}\,(2\chi\, s_W \cos 2\xi - \sin 2\xi)\, h\, Z_\mu Z'^\mu \,\equiv g_{hZZ'}\, h\, Z_\mu Z'^\mu\,, \tag{146}$$

at $\mathcal{O}(\chi)$, which allows the decay $Z' \to Z\,h$. The decay width is [199]

$$\Gamma(Z' \to Z\,h) = \frac{g_{hZZ'}^2\, m_{Z'}}{192\pi}\sqrt{\lambda(1, r_Z^2, r_h^2)}\left[\lambda(1, r_Z^2, r_h^2) + 12\, r_Z^2\right]\,, \tag{147}$$

where $r_Z = m_Z/m_{Z'}$, $r_h = m_h/m_{Z'}$, and $\lambda(a,b,c) = a^2+b^2+c^2-2ab-2ac-2bc$. The $Z' \to W^+W^-$ decay is mediated by the WWA and WWZ vertices in the Standard Model, which have couplings of $g_{WWA} = e$ and $g_{WWZ} = e\cot\theta_W$. The Z' boson will therefore couple to W^+W^- with strength

$$g_{WWZ'} = e\,\left[\cot\theta_W\,(s_W\chi\cos\xi - \sin\xi) - c_W\chi\cos\xi\right] = -e\cot\theta_W\sin\xi\,, \tag{148}$$

which leads to a decay width of [200]

$$\Gamma(Z' \to W^+W^-) = \frac{g^2_{WWZ'}\,m_{Z'}}{192\pi}\left(\frac{m_{Z'}}{m_Z}\right)^4 (1-4\,r_W^2)^{3/2}\left(1+20\,r_W^2+12\,r_W^4\right)\,, \tag{149}$$

where $r_W = m_W/m_{Z'}$.

C Heavy Stops

C.1 Simulation Details

We use `MadGraph5_aMC@NLO` [201] package to simulate all parton level events. Showering of the parton level events was done in `Pythia8` [93]. After showering, a 0.1×0.1 detector granularization was applied for particles in the final state, which were then analyzed and clustered using `FastJet` [202]. For the signal, we simulated 50000 events at a center-of-mass energy of 13 TeV. We assume a K-factor of 1.5 for the signal production cross section [203]. The desired signal topology where the stops decay with a branching ratio of 100% to tops and neutralinos, with the tops decaying hadronically, was forced in the simulation. All other parameters in the signal simulation were left at their default values.

For all background events, we simulate events at a center-of-mass energy of 13 TeV, using the default SM model file, with default model values. For the $\bar{t}\,t$ + jets background, we simulated 4.975×10^7 events. We used an unmatched sample involving 2 jets, which we checked the variable distributions for a matched sample after the final cuts. We assume a K-factor of 1.3 [201]. The desired semi-leptonic background topology where one top decays leptonically (without taus) and the other hadronically was forced in the simulation. All other parameters in the $\bar{t}\,t$ +jets simulation were left at their default values, except for imposing a generator level cut requiring the missing transverse energy (sum of the neutrino momenta) to be above 200 GeV. For the $\bar{t}\,t + Z$ background, we simulated 7.5×10^5 events. The desired background topology where both tops decay hadronically and the Z boson decays to neutrinos was forced in the simulation. All other parameters in the $\bar{t}\,t + Z$ simulation were left at their default values, except requiring a baseline cut of $\not{E}_{\mathrm{T}} > 200$ GeV. For the $Z +$ jets background, we simulated 3.75×10^7 events. The desired background topology where the Z boson decays to neutrinos was forced in the simulation. All other parameters in the $Z + 3j$ simulation were left at their default values, except requiring $\not{E}_{\mathrm{T}} > 200$ GeV. For the $W +$ jets background, we simulated 4.975×10^7 events. The desired background topology where the W boson decays to $\ell\bar{\nu}$ or $\bar{\ell}\nu$, where ℓ does not include taus, was forced in the simulation. All other parameters in the $W + 3j$ simulation were left at their default values, except a cut of $\not{E}_{\mathrm{T}} > 200$ GeV.

Bibliography

[1] **CDF** Collaboration, F. Abe *et al.*, "Observation of top quark production in $\bar{p}p$ collisions," *Phys. Rev. Lett.* **74** (1995) 2626–2631, `hep-ex/9503002`.

[2] **D0** Collaboration, S. Abachi *et al.*, "Observation of the top quark," *Phys. Rev. Lett.* **74** (1995) 2632–2637, `hep-ex/9503003`.

[3] **DONUT** Collaboration, K. Kodama *et al.*, "Observation of tau neutrino interactions," *Phys. Lett.* **B504** (2001) 218–224, `hep-ex/0012035`.

[4] **CMS** Collaboration, S. Chatrchyan *et al.*, "Observation of a new boson at a mass of 125 GeV with the CMS experiment at the LHC," *Phys. Lett.* **B716** (2012) 30–61, `1207.7235`.

[5] **ATLAS** Collaboration, G. Aad *et al.*, "Observation of a new particle in the search for the Standard Model Higgs boson with the ATLAS detector at the LHC," *Phys. Lett.* **B716** (2012) 1–29, `1207.7214`.

[6] **Particle Data Group** Collaboration, C. Patrignani *et al.*, "Review of Particle Physics," *Chin. Phys.* **C40** (2016), no. 10, 100001.

[7] S. Weinberg, "The Cosmological Constant Problem," *Rev. Mod. Phys.* **61** (1989) 1–23.

[8] J. M. Pendlebury *et al.*, "Revised experimental upper limit on the electric dipole moment of the neutron," *Phys. Rev.* **D92** (2015), no. 9, 092003, `1509.04411`.

[9] F. Capozzi, E. Lisi, A. Marrone, D. Montanino, and A. Palazzo, "Neutrino masses and mixings: Status of known and unknown 3ν parameters," *Nucl. Phys.* **B908** (2016) 218–234, `1601.07777`.

[10] G. Bertone and D. Hooper, "A History of Dark Matter," *Submitted to: Rev. Mod. Phys.* (2016) `1605.04909`.

[11] E. Witten, "Cosmic Separation of Phases," *Phys. Rev.* **D30** (1984) 272–285.

[12] **LUX** Collaboration, D. S. Akerib *et al.*, "Results from a search for dark matter in the complete LUX exposure," *Phys. Rev. Lett.* **118** (2017), no. 2, 021303, `1608.07648`.

[13] H. Georgi and S. L. Glashow, "Unity of All Elementary Particle Forces," *Phys. Rev. Lett.* **32** (1974) 438–441.

[14] J. R. Ellis, M. K. Gaillard, and D. V. Nanopoulos, "Baryon Number Generation in Grand Unified Theories," *Phys. Lett.* **B80** (1979) 360. [Erratum: Phys. Lett.B82,464(1979)].

[15] **Belle** Collaboration, K. Abe *et al.*, "Observation of a new narrow charmonium state in exclusive B+- —¿ K+- pi+ pi- J / psi decays," in *Proceedings, 21st International Symposium on Lepton and Photon Interactions at High Energies (LP 03): Batavia, ILL, August 11-16, 2003.* 2003. `hep-ex/0308029`.

[16] **Belle** Collaboration, S. K. Choi *et al.*, “Observation of a resonance-like structure in the pi+- psi-prime mass distribution in exclusive B —¿ K pi+- psi-prime decays,” *Phys. Rev. Lett.* **100** (2008) 142001, `0708.1790`.

[17] **BESIII** Collaboration, M. Ablikim *et al.*, “Observation of a Charged Charmoniumlike Structure in e^+e^- ? $?^+?^-$ J/? at $\sqrt{s}$ =4.26??GeV,” *Phys. Rev. Lett.* **110** (2013) 252001, `1303.5949`.

[18] **LHCb** Collaboration, R. Aaij *et al.*, “Observation of $J/\psi\phi$ structures consistent with exotic states from amplitude analysis of $B^+ \to J/\psi\phi K^+$ decays,” *Phys. Rev. Lett.* **118** (2017), no. 2, 022003, `1606.07895`.

[19] Y. Bai, S. Lu, and J. Osborne, “Beauty-full Tetraquarks,” `1612.00012`.

[20] T. Appelquist and H. D. Politzer, “Orthocharmonium and e+ e- Annihilation,” *Phys. Rev. Lett.* **34** (1975) 43.

[21] E. Eichten, K. Gottfried, T. Kinoshita, J. B. Kogut, K. D. Lane, and T.-M. Yan, “The Spectrum of Charmonium,” *Phys. Rev. Lett.* **34** (1975) 369–372. [Erratum: Phys. Rev. Lett.36,1276(1976)].

[22] C. Quigg and J. L. Rosner, “Quantum Mechanics with Applications to Quarkonium,” *Phys. Rept.* **56** (1979) 167–235.

[23] W. Kwong, J. L. Rosner, and C. Quigg, “Heavy Quark Systems,” *Ann. Rev. Nucl. Part. Sci.* **37** (1987) 325–382.

[24] N. Brambilla, A. Pineda, J. Soto, and A. Vairo, “Effective field theories for heavy quarkonium,” *Rev. Mod. Phys.* **77** (2005) 1423, `hep-ph/0410047`.

[25] H.-X. Chen, W. Chen, X. Liu, and S.-L. Zhu, “The hidden-charm pentaquark and tetraquark states,” *Phys. Rept.* **639** (2016) 1–121, `1601.02092`.

[26] J. A. Wheeler, “Polyelectrons,” *Ann. NY Acad. Sci.* **48** (1946) 219–238.

[27] E. A. Hylleraas and A. Ore, “Binding Energy of the Positronium Molecule,” *Phys. Rev.* **71** (1947) 493–496.

[28] Y. K. Ho, “Binding energy of positronium molecules,” *Phys. Rev.* **A33** (1986) 3584–3587.

[29] A. M. Frolov and V. H. Smith, “The CMP invariance for symmetrical Coulomb four-body systems with unit charges,” *J. Phys.* **B29** (1996) L433–L440.

[30] D. B. Cassidy and A. P. Mills, “The production of molecular positronium,” *Nature* **449** (2007) 195.

[31] F. London, “Zur Theorie und Systematik der Molekularkräfte,” *Zeitschrift für Physik* **63** (1930) 3–4.

[32] T. Appelquist and W. Fischler, “Some Remarks on Van Der Waals Forces in QCD,” *Phys. Lett.* **B77** (1978) 405–410.

[33] N. Brambilla, G. Krein, J. Tarrús Castelà, and A. Vairo, "Long-range properties of $1S$ bottomonium states," *Phys. Rev.* **D93** (2016), no. 5, 054002, `1510.05895`.

[34] T. Appelquist, M. Dine, and I. J. Muzinich, "The Static Limit of Quantum Chromodynamics," *Phys. Rev.* **D17** (1978) 2074.

[35] M. E. Peskin, "Short Distance Analysis for Heavy Quark Systems. 1. Diagrammatics," *Nucl. Phys.* **B156** (1979) 365–390.

[36] G. Bhanot and M. E. Peskin, "Short Distance Analysis for Heavy Quark Systems. 2. Applications," *Nucl. Phys.* **B156** (1979) 391–416.

[37] E. Eichten, K. Gottfried, T. Kinoshita, K. D. Lane, and T.-M. Yan, "Charmonium: The Model," *Phys. Rev.* **D17** (1978) 3090. [Erratum: Phys. Rev.D21,313(1980)].

[38] W. Chen, H.-X. Chen, X. Liu, T. G. Steele, and S.-L. Zhu, "Hunting for exotic doubly hidden-charm/bottom tetraquark states," `1605.01647`.

[39] L. J. Reinders, H. Rubinstein, and S. Yazaki, "Hadron Properties from QCD Sum Rules," *Phys. Rept.* **127** (1985) 1.

[40] A. V. Berezhnoy, A. V. Luchinsky, and A. A. Novoselov, "Tetraquarks Composed of 4 Heavy Quarks," *Phys. Rev.* **D86** (2012) 034004, `1111.1867`.

[41] M. Karliner, J. L. Rosner, and S. Nussinov, "Production and Decay of (Q Q Qbar Qbar) States," `1611.00348`.

[42] J. Carlson, J. B. Kogut, and V. R. Pandharipande, "A Quark Model for Baryons Based on Quantum Chromodynamics," *Phys. Rev.* **D27** (1983) 233.

[43] F. Okiharu, H. Suganuma, and T. T. Takahashi, "Detailed analysis of the tetraquark potential and flip-flop in SU(3) lattice QCD," *Phys. Rev.* **D72** (2005) 014505, `hep-lat/0412012`.

[44] J. Vijande, A. Valcarce, and J. M. Richard, "Stability of multiquarks in a simple string model," *Phys. Rev.* **D76** (2007) 114013, `0707.3996`.

[45] I. Kosztin, B. Faber, and K. Schulten, "Introduction to the diffusion Monte Carlo method," *Am. J. Phys.* **64** (1996) 633, `physics/9702023`.

[46] W. D. Smith, "How to find Steiner minimal trees in euclideand-space," *Algorithmica* **7** (1992), no. 1-6, 137–177.

[47] A. De Rujula, H. Georgi, and S. L. Glashow, "Hadron Masses in a Gauge Theory," *Phys. Rev.* **D12** (1975) 147–162.

[48] E. Eichten and F. Feinberg, "Spin Dependent Forces in QCD," *Phys. Rev.* **D23** (1981) 2724.

[49] M. Dine, "Spin Dependent Interactions in Heavy Quark Systems," *Phys. Lett.* **B81** (1979) 339–342.

[50] A. M. Frolov, S. I. Kryuchkov, and V. H. Smith, "(e-, e+) -pair annihilation in the positronium molecule Ps-2," *Phys. Rev.* **A51** (1995) 4514–4519.

[51] A. De Rujula, H. Georgi, and S. L. Glashow, "Molecular Charmonium: A New Spectroscopy?," *Phys. Rev. Lett.* **38** (1977) 317.

[52] **CMS** Collaboration, V. Khachatryan *et al.*, "Observation of Υ(1S) pair production in proton-proton collisions at $\sqrt{s} = 8$ TeV," *JHEP* (2016) `1610.07095`.

[53] Y. Bai and J. Osborne, "Chromo-Rayleigh Interactions of Dark Matter," *JHEP* **11** (2015) 036, `1506.07110`.

[54] M. Cahill-Rowley, R. Cotta, A. Drlica-Wagner, S. Funk, J. Hewett, *et al.*, "Complementarity of dark matter searches in the phenomenological MSSM," *Phys.Rev.* **D91** (2015), no. 5, 055011, `1405.6716`.

[55] A. L. Erickcek, P. J. Steinhardt, D. McCammon, and P. C. McGuire, "Constraints on the Interactions between Dark Matter and Baryons from the X-ray Quantum Calorimetry Experiment," *Phys.Rev.* **D76** (2007) 042007, `0704.0794`.

[56] B. A. Dobrescu, D. Hooper, K. Kong, and R. Mahbubani, "Spinless photon dark matter from two universal extra dimensions," *JCAP* **0710** (2007) 012, `0706.3409`.

[57] J. Bagnasco, M. Dine, and S. D. Thomas, "Detecting technibaryon dark matter," *Phys.Lett.* **B320** (1994) 99–104, `hep-ph/9310290`.

[58] M. T. Frandsen, U. Haisch, F. Kahlhoefer, P. Mertsch, and K. Schmidt-Hoberg, "Loop-induced dark matter direct detection signals from gamma-ray lines," *JCAP* **1210** (2012) 033, `1207.3971`.

[59] J. Liu, B. Shuve, N. Weiner, and I. Yavin, "Looking for new charged states at the LHC: Signatures of Magnetic and Rayleigh Dark Matter," *JHEP* **1307** (2013) 144, `1303.4404`.

[60] S. Chang, R. Edezhath, J. Hutchinson, and M. Luty, "Effective WIMPs," *Phys.Rev.* **D89** (2014), no. 1, 015011, `1307.8120`.

[61] H. An, L.-T. Wang, and H. Zhang, "Dark matter with t-channel mediator: a simple step beyond contact interaction," *Phys.Rev.* **D89** (2014), no. 11, 115014, `1308.0592`.

[62] Y. Bai and J. Berger, "Fermion Portal Dark Matter," *JHEP* **1311** (2013) 171, `1308.0612`.

[63] A. DiFranzo, K. I. Nagao, A. Rajaraman, and T. M. Tait, "Simplified Models for Dark Matter Interacting with Quarks," *JHEP* **1311** (2013) 014, `1308.2679`.

[64] O. Buchmueller, M. J. Dolan, and C. McCabe, "Beyond Effective Field Theory for Dark Matter Searches at the LHC," *JHEP* **1401** (2014) 025, `1308.6799`.

[65] B. Batell, T. Lin, and L.-T. Wang, "Flavored Dark Matter and R-Parity Violation," *JHEP* **1401** (2014) 075, `1309.4462`.

[66] M. Papucci, A. Vichi, and K. M. Zurek, "Monojet versus the rest of the world I: t-channel models," *JHEP* **1411** (2014) 024, `1402.2285`.

[67] Y. Bai and J. Berger, "Lepton Portal Dark Matter," *JHEP* **1408** (2014) 153, `1402.6696`.

[68] S. Chang, R. Edezhath, J. Hutchinson, and M. Luty, "Leptophilic Effective WIMPs," *Phys.Rev.* **D90** (2014), no. 1, 015011, `1402.7358`.

[69] P. Agrawal, Z. Chacko, and C. B. Verhaaren, "Leptophilic Dark Matter and the Anomalous Magnetic Moment of the Muon," *JHEP* **1408** (2014) 147, `1402.7369`.

[70] M. Garny, A. Ibarra, S. Rydbeck, and S. Vogl, "Majorana Dark Matter with a Coloured Mediator: Collider vs Direct and Indirect Searches," *JHEP* **1406** (2014) 169, `1403.4634`.

[71] J.-H. Yu, "Vector Fermion-Portal Dark Matter: Direct Detection and Galactic Center Gamma-Ray Excess," *Phys.Rev.* **D90** (2014), no. 9, 095010, `1409.3227`.

[72] M. R. Buckley, D. Feld, and D. Goncalves, "Scalar Simplified Models for Dark Matter," *Phys.Rev.* **D91** (2015), no. 1, 015017, `1410.6497`.

[73] A. Berlin, S. Gori, T. Lin, and L.-T. Wang, "Pseudoscalar Portal Dark Matter," `1502.06000`.

[74] T. Jacques and K. Nordstrm, "Mapping monojet constraints onto Simplified Dark Matter Models," `1502.05721`.

[75] M. Garny, A. Ibarra, and S. Vogl, "Signatures of Majorana dark matter with t-channel mediators," `1503.01500`.

[76] M. Chala, F. Kahlhoefer, M. McCullough, G. Nardini, and K. Schmidt-Hoberg, "Constraining Dark Sectors with Monojets and Dijets," `1503.05916`.

[77] N. F. Bell, Y. Cai, J. B. Dent, R. K. Leane, and T. J. Weiler, "Dark matter at the LHC: EFTs and gauge invariance," `1503.07874`.

[78] M. A. Shifman, A. Vainshtein, and V. I. Zakharov, "Remarks on Higgs Boson Interactions with Nucleons," *Phys.Lett.* **B78** (1978) 443.

[79] G. Belanger, F. Boudjema, A. Pukhov, and A. Semenov, "Dark matter direct detection rate in a generic model with micrOMEGAs 2.2," *Comput.Phys.Commun.* **180** (2009) 747–767, `0803.2360`.

[80] P. Junnarkar and A. Walker-Loud, "Scalar strange content of the nucleon from lattice QCD," *Phys.Rev.* **D87** (2013), no. 11, 114510, `1301.1114`.

[81] H.-Y. Cheng and C.-W. Chiang, "Revisiting Scalar and Pseudoscalar Couplings with Nucleons," *JHEP* **1207** (2012) 009, `1202.1292`.

[82] R. J. Hill and M. P. Solon, "Standard Model anatomy of WIMP dark matter direct detection I: weak-scale matching," *Phys.Rev.* **D91** (2015) 043504, `1401.3339`.

[83] R. J. Hill and M. P. Solon, "Standard Model anatomy of WIMP dark matter direct detection II: QCD analysis and hadronic matrix elements," *Phys.Rev.* **D91** (2015) 043505, `1409.8290`.

[84] D. Diakonov, M. V. Polyakov, and C. Weiss, "Hadronic matrix elements of gluon operators in the instanton vacuum," *Nucl.Phys.* **B461** (1996) 539–580, `hep-ph/9510232`.

[85] M. Felizardo, T. Girard, T. Morlat, A. Fernandes, A. Ramos, *et al.*, "Final Analysis and Results of the Phase II SIMPLE Dark Matter Search," *Phys.Rev.Lett.* **108** (2012) 201302, `1106.3014`.

[86] **COUPP** Collaboration, E. Behnke *et al.*, "First Dark Matter Search Results from a 4-kg CF_3I Bubble Chamber Operated in a Deep Underground Site," *Phys.Rev.* **D86** (2012) 052001, `1204.3094`.

[87] J. Goodman, M. Ibe, A. Rajaraman, W. Shepherd, T. M. Tait, *et al.*, "Constraints on Dark Matter from Colliders," *Phys.Rev.* **D82** (2010) 116010, `1008.1783`.

[88] Y. Bai, P. J. Fox, and R. Harnik, "The Tevatron at the Frontier of Dark Matter Direct Detection," *JHEP* **1012** (2010) 048, `1005.3797`.

[89] **CMS** Collaboration, V. Khachatryan *et al.*, "Search for dark matter, extra dimensions, and unparticles in monojet events in proton-proton collisions at $\sqrt{s} = 8$ TeV," `1408.3583`.

[90] **ATLAS** Collaboration, "Search for New Phenomena in Monojet plus Missing Transverse Momentum Final States using 10fb-1 of pp Collisions at sqrts=8 TeV with the ATLAS detector at the LHC," `ATLAS-CONF-2012-147, ATLAS-COM-CONF-2012-190`.

[91] A. Alloul, N. D. Christensen, C. Degrande, C. Duhr, and B. Fuks, "FeynRules 2.0 - A complete toolbox for tree-level phenomenology," *Comput.Phys.Commun.* **185** (2014) 2250–2300, `1310.1921`.

[92] J. Alwall, M. Herquet, F. Maltoni, O. Mattelaer, and T. Stelzer, "MadGraph 5 : Going Beyond," *JHEP* **1106** (2011) 128, `1106.0522`.

[93] T. Sjostrand, S. Mrenna, and P. Z. Skands, "A Brief Introduction to PYTHIA 8.1," *Comput.Phys.Commun.* **178** (2008) 852–867, `0710.3820`.

[94] J. S. Conway, "Pretty Good Simulation of high-energy collisions," `090401 release`.

[95] **CMS** Collaboration, S. Chatrchyan *et al.*, "Search for invisible decays of Higgs bosons in the vector boson fusion and associated ZH production modes," *Eur. Phys. J.* **C74** (2014) 2980, `1404.1344`.

[96] **ATLAS** Collaboration, G. Aad *et al.*, "Search for invisible decays of a Higgs boson using vector-boson fusion in pp collisions at $\sqrt{s} = 8$ TeV with the ATLAS detector," `1508.07869`.

[97] Y. Bai, V. Barger, L. L. Everett, and G. Shaughnessy, "Two-Higgs-doublet-portal dark-matter model: LHC data and Fermi-LAT 135 GeV line," *Phys.Rev.* **D88** (2013), no. 1, 015008, `1212.5604`.

[98] U. Haisch and E. Re, "Simplified dark matter top-quark interactions at the LHC," `1503.00691`.

[99] Y. Bai and B. A. Dobrescu, "Heavy octets and Tevatron signals with three or four b jets," *JHEP* **07** (2011) 100, `1012.5814`.

[100] R. S. Chivukula, A. Farzinnia, J. Ren, and E. H. Simmons, “Constraints on the Scalar Sector of the Renormalizable Coloron Model,” *Phys. Rev.* **D88** (2013), no. 7, 075020, `1307.1064`. [Erratum: Phys. Rev.D89,no.5,059905(2014)].

[101] A. V. Manohar and M. B. Wise, “Modifications to the properties of the Higgs boson,” *Phys. Lett.* **B636** (2006) 107–113, `hep-ph/0601212`.

[102] U. Aglietti, R. Bonciani, G. Degrassi, and A. Vicini, “Analytic Results for Virtual QCD Corrections to Higgs Production and Decay,” *JHEP* **01** (2007) 021, `hep-ph/0611266`.

[103] R. Boughezal and F. Petriello, “Color-octet scalar effects on Higgs boson production in gluon fusion,” *Phys. Rev.* **D81** (2010) 114033, `1003.2046`.

[104] Y. Bai, J. Fan, and J. L. Hewett, “Hiding a Heavy Higgs Boson at the 7 TeV LHC,” *JHEP* **08** (2012) 014, `1112.1964`.

[105] B. A. Dobrescu, G. D. Kribs, and A. Martin, “Higgs Underproduction at the LHC,” *Phys. Rev.* **D85** (2012) 074031, `1112.2208`.

[106] T. ATLAS and C. Collaborations, “Measurements of the Higgs boson production and decay rates and constraints on its couplings from a combined ATLAS and CMS analysis of the LHC pp collision data at $\sqrt{s} = 7$ and 8 TeV,”.

[107] M. I. Gresham and M. B. Wise, “Color octet scalar production at the LHC,” *Phys.Rev.* **D76** (2007) 075003, `0706.0909`.

[108] Y. Bai, A. Katz, and B. Tweedie, “Pulling Out All the Stops: Searching for RPV SUSY with Stop-Jets,” *JHEP* **1401** (2014) 040, `1309.6631`.

[109] **CMS** Collaboration, V. Khachatryan *et al.*, “Search for pair-produced resonances decaying to jet pairs in proton-proton collisions at $\sqrt{s} = 8$ TeV,” `1412.7706`.

[110] **CMS** Collaboration, S. Chatrchyan *et al.*, “Search for new physics in the multijet and missing transverse momentum final state in proton-proton collisions at $\sqrt{s}$= 8 TeV,” *JHEP* **1406** (2014) 055, `1402.4770`.

[111] D. Goncalves-Netto, D. Lopez-Val, K. Mawatari, T. Plehn, and I. Wigmore, “Sgluon Pair Production to Next-to-Leading Order,” *Phys.Rev.* **D85** (2012) 114024, `1203.6358`.

[112] T. Appelquist, H.-C. Cheng, and B. A. Dobrescu, “Bounds on universal extra dimensions,” *Phys. Rev.* **D64** (2001) 035002, `hep-ph/0012100`.

[113] M. Perelstein, “Little Higgs models and their phenomenology,” *Prog. Part. Nucl. Phys.* **58** (2007) 247–291, `hep-ph/0512128`.

[114] S. Weinberg, “Larger Higgs Exchange Terms in the Neutron Electric Dipole Moment,” *Phys.Rev.Lett.* **63** (1989) 2333.

[115] **CMS** Collaboration, V. Khachatryan *et al.*, “Search for vector-like charge 2/3 T quarks in proton-proton collisions at $\sqrt{s} = 8$ TeV,” `1509.04177`.

[116] **CMS** Collaboration, S. Chatrchyan *et al.*, "Inclusive search for a vector-like T quark with charge $\frac{2}{3}$ in pp collisions at $\sqrt{s} = 8$ TeV," *Phys.Lett.* **B729** (2014) 149–171, `1311.7667`.

[117] S. Hoeche, F. Krauss, N. Lavesson, L. Lonnblad, M. Mangano, *et al.*, "Matching parton showers and matrix elements," `hep-ph/0602031`.

[118] **LUX** Collaboration, D. Akerib *et al.*, "First results from the LUX dark matter experiment at the Sanford Underground Research Facility," *Phys.Rev.Lett.* **112** (2014) 091303, `1310.8214`.

[119] **SIMPLE** Collaboration, M. Felizardo *et al.*, "The SIMPLE Phase II Dark Matter Search," *Phys.Rev.* **D89** (2014), no. 7, 072013, `1404.4309`.

[120] **PICASSO** Collaboration, S. Archambault *et al.*, "Constraints on Low-Mass WIMP Interactions on ^{19}F from PICASSO," *Phys.Lett.* **B711** (2012) 153–161, `1202.1240`.

[121] **SNO** Collaboration, C. Amole *et al.*, "Dark Matter Search Results from the PICO-2L C_3F_8 Bubble Chamber," `1503.00008`.

[122] **IceCube** Collaboration, M. Aartsen *et al.*, "Search for dark matter annihilations in the Sun with the 79-string IceCube detector," *Phys.Rev.Lett.* **110** (2013), no. 13, 131302, `1212.4097`.

[123] **Super-Kamiokande** Collaboration, K. Choi *et al.*, "Search for neutrinos from annihilation of captured low-mass dark matter particles in the Sun by Super-Kamiokande," *Phys.Rev.Lett.* **114** (2015), no. 14, 141301, `1503.04858`.

[124] **CMS** Collaboration, V. Khachatryan *et al.*, "Search for Resonant Production of High-Mass Photon Pairs in Proton-Proton Collisions at $\sqrt{s}$ =8 and 13 TeV," *Phys. Rev. Lett.* **117** (2016), no. 5, 051802, `1606.04093`.

[125] **ATLAS** Collaboration, M. Aaboud *et al.*, "Search for resonances in diphoton events at $\sqrt{s}$=13 TeV with the ATLAS detector," *JHEP* **09** (2016) 001, `1606.03833`.

[126] **CMS** Collaboration, V. Khachatryan *et al.*, "Search for high-mass diphoton resonances in proton?proton collisions at 13 TeV and combination with 8 TeV search," *Phys. Lett.* **B767** (2017) 147–170, `1609.02507`.

[127] **ATLAS** Collaboration, T. A. collaboration, "Search for scalar diphoton resonances with 15.4 fb^{-1} of data collected at $\sqrt{s}$=13 TeV in 2015 and 2016 with the ATLAS detector,".

[128] A. Strumia, "Interpreting the 750 GeV digamma excess: a review," in *Proceedings, 51st Rencontres de Moriond on Electroweak Interactions and Unified Theories: La Thuile, Italy, March 12-19, 2016*, pp. 407–426, ARISF. ARISF, 2016. `1605.09401`.

[129] Y. Bai, J. Berger, J. Osborne, and B. A. Stefanek, "Phenomenology of Strongly Coupled Chiral Gauge Theories," *JHEP* **11** (2016) 153, `1605.07183`.

[130] C. T. Hill and E. H. Simmons, "Strong dynamics and electroweak symmetry breaking," *Phys. Rept.* **381** (2003) 235–402, `hep-ph/0203079`. [Erratum: Phys. Rept.390,553(2004)].

[131] H.-J. He, N. Polonsky, and S.-f. Su, "Extra families, Higgs spectrum and oblique corrections," *Phys. Rev.* **D64** (2001) 053004, `hep-ph/0102144`.

[132] V. A. Novikov, L. B. Okun, A. N. Rozanov, and M. I. Vysotsky, "Extra generations and discrepancies of electroweak precision data," *Phys. Lett.* **B529** (2002) 111–116, `hep-ph/0111028`.

[133] G. D. Kribs, T. Plehn, M. Spannowsky, and T. M. P. Tait, "Four generations and Higgs physics," *Phys. Rev.* **D76** (2007) 075016, `0706.3718`.

[134] J. Erler and P. Langacker, "Precision Constraints on Extra Fermion Generations," *Phys. Rev. Lett.* **105** (2010) 031801, `1003.3211`.

[135] O. Eberhardt, G. Herbert, H. Lacker, A. Lenz, A. Menzel, U. Nierste, and M. Wiebusch, "Impact of a Higgs boson at a mass of 126 GeV on the standard model with three and four fermion generations," *Phys. Rev. Lett.* **109** (2012) 241802, `1209.1101`.

[136] Y. Iwasaki, K. Kanaya, S. Kaya, S. Sakai, and T. Yoshie, "Phase structure of lattice QCD for general number of flavors," *Phys. Rev.* **D69** (2004) 014507, `hep-lat/0309159`.

[137] T. A. Ryttov and F. Sannino, "Conformal Windows of SU(N) Gauge Theories, Higher Dimensional Representations and The Size of The Unparticle World," *Phys. Rev.* **D76** (2007) 105004, `0707.3166`.

[138] T. Appelquist *et al.*, "Approaching Conformality with Ten Flavors," `1204.6000`.

[139] A. Deuzeman, M. P. Lombardo, K. Miura, T. Nunes da Silva, and E. Pallante, "Phases of many flavors QCD : Lattice results," *PoS* **ConfinementX** (2012) 274, `1304.3245`.

[140] M. P. Lombardo, K. Miura, T. J. Nunes da Silva, and E. Pallante, "On the particle spectrum and the conformal window," *JHEP* **12** (2014) 183, `1410.0298`.

[141] Z. Fodor, K. Holland, J. Kuti, S. Mondal, D. Nogradi, and C. H. Wong, "Fate of the conformal fixed point with twelve massless fermions and SU(3) gauge group," `1607.06121`.

[142] M. E. Peskin, "The Alignment of the Vacuum in Theories of Technicolor," *Nucl. Phys.* **B175** (1980) 197–233.

[143] Y. Bai and R. J. Hill, "Weakly Interacting Stable Pions," *Phys. Rev.* **D82** (2010) 111701, `1005.0008`.

[144] O. Antipin, M. Redi, A. Strumia, and E. Vigiani, "Accidental Composite Dark Matter," *JHEP* **07** (2015) 039, `1503.08749`.

[145] Y. Bai, J. Berger, and R. Lu, "A 750 GeV Dark Pion: Cousin of a Dark G-parity-odd WIMP," *Phys. Rev.* **D93** (2016) 076009, `1512.05779`.

[146] M. Redi, A. Strumia, A. Tesi, and E. Vigiani, "Di-photon resonance and Dark Matter as heavy pions," `1602.07297`.

[147] B. Holdom, "Two U(1)'s and Epsilon Charge Shifts," *Phys. Lett.* **B166** (1986) 196–198.

[148] A. Hook, E. Izaguirre, and J. G. Wacker, “Model Independent Bounds on Kinetic Mixing,” *Adv. High Energy Phys.* **2011** (2011) 859762, `1006.0973`.

[149] M. Pospelov, “Secluded U(1) below the weak scale,” *Phys. Rev.* **D80** (2009) 095002, `0811.1030`.

[150] **BaBar** Collaboration, B. Aubert *et al.*, “Search for a Narrow Resonance in e+e- to Four Lepton Final States,” in *Proceedings, 24th International Symposium on Lepton-Photon Interactions at High Energy (LP09).* 2009. `0908.2821`.

[151] **SLD Electroweak Group, SLD Heavy Flavor Group, DELPHI, LEP, ALEPH, OPAL, LEP Electroweak Working Group, L3** Collaboration, t. S. Electroweak, “A Combination of preliminary electroweak measurements and constraints on the standard model,” `hep-ex/0312023`.

[152] A. D. Martin, W. J. Stirling, R. S. Thorne, and G. Watt, “Parton distributions for the LHC,” *Eur. Phys. J.* **C63** (2009) 189–285, `0901.0002`.

[153] S. Catani, D. de Florian, M. Grazzini, and P. Nason, “Soft gluon resummation for Higgs boson production at hadron colliders,” *JHEP* **07** (2003) 028, `hep-ph/0306211`.

[154] A. Idilbi, C. Kim, and T. Mehen, “Factorization and resummation for single color-octet scalar production at the LHC,” *Phys. Rev.* **D79** (2009) 114016, `0903.3668`.

[155] Y. Bai, V. Barger, and J. Berger, “Color-octet Companions of a 750 GeV Heavy Pion,” `1604.07835`.

[156] R. S. Chivukula, A. Farzinnia, K. Mohan, and E. H. Simmons, “Diphoton Resonances in the Renormalizable Coloron Model,” `1604.02157`.

[157] D. Buttazzo, A. Greljo, G. Isidori, and D. Marzocca, “Toward a coherent solution of diphoton and flavor anomalies,” `1604.03940`.

[158] K. Harigaya and Y. Nomura, “A Composite Model for the 750 GeV Diphoton Excess,” *JHEP* **03** (2016) 091, `1602.01092`.

[159] **CMS** Collaboration, V. Khachatryan *et al.*, “Search for Decays of Stopped Long-Lived Particles Produced in Proton-Proton Collisions at $\sqrt{s} = 8\,\text{TeV}$,” *Eur. Phys. J.* **C75** (2015), no. 4, 151, `1501.05603`.

[160] **CMS** Collaboration, S. Chatrchyan *et al.*, “Searches for long-lived charged particles in pp collisions at $\sqrt{s}$=7 and 8 TeV,” *JHEP* **07** (2013) 122, `1305.0491`.

[161] Y. Bai, J. Berger, J. Osborne, and B. A. Stefanek, “Search for Heavy Stops with Merged Top-Jets,” `1611.05046`.

[162] **CMS** Collaboration, S. Chatrchyan *et al.*, “A New Boson with a Mass of 125 GeV Observed with the CMS Experiment at the Large Hadron Collider,” *Science* **338** (2012) 1569–1575.

[163] **ATLAS** Collaboration, G. Aad *et al.*, “A particle consistent with the Higgs Boson observed with the ATLAS Detector at the Large Hadron Collider,” *Science* **338** (2012) 1576–1582.

[164] S. P. Martin, "A Supersymmetry primer," `hep-ph/9709356`. [Adv. Ser. Direct. High Energy Phys.18,1(1998)].

[165] D. J. H. Chung, L. L. Everett, G. L. Kane, S. F. King, J. D. Lykken, and L.-T. Wang, "The Soft supersymmetry breaking Lagrangian: Theory and applications," *Phys. Rept.* **407** (2005) 1–203, `hep-ph/0312378`.

[166] S. Dimopoulos and G. F. Giudice, "Naturalness constraints in supersymmetric theories with nonuniversal soft terms," *Phys. Lett.* **B357** (1995) 573–578, `hep-ph/9507282`.

[167] A. G. Cohen, D. B. Kaplan, and A. E. Nelson, "The More minimal supersymmetric standard model," *Phys. Lett.* **B388** (1996) 588–598, `hep-ph/9607394`.

[168] M. Cahill-Rowley, J. L. Hewett, A. Ismail, and T. G. Rizzo, "Lessons and prospects from the pMSSM after LHC Run I," *Phys. Rev.* **D91** (2015), no. 5, 055002, `1407.4130`.

[169] H. Baer, V. Barger, D. Mickelson, and M. Padeffke-Kirkland, "SUSY models under siege: LHC constraints and electroweak fine-tuning," *Phys. Rev.* **D89** (2014), no. 11, 115019, `1404.2277`.

[170] Z. Han, A. Katz, D. Krohn, and M. Reece, "(Light) Stop Signs," *JHEP* **08** (2012) 083, `1205.5808`.

[171] A. Delgado, G. F. Giudice, G. Isidori, M. Pierini, and A. Strumia, "The light stop window," *Eur. Phys. J.* **C73** (2013), no. 3, 2370, `1212.6847`.

[172] B. Dutta, W. Flanagan, A. Gurrola, W. Johns, T. Kamon, P. Sheldon, K. Sinha, K. Wang, and S. Wu, "Probing compressed top squark scenarios at the LHC at 14 TeV," *Phys. Rev.* **D90** (2014), no. 9, 095022, `1312.1348`.

[173] W. S. Cho, J. S. Gainer, D. Kim, K. T. Matchev, F. Moortgat, L. Pape, and M. Park, "Improving the sensitivity of stop searches with on-shell constrained invariant mass variables," *JHEP* **05** (2015) 040, `1411.0664`.

[174] G. Ferretti, R. Franceschini, C. Petersson, and R. Torre, "Spot the stop with a b-tag," *Phys. Rev. Lett.* **114** (2015) 201801, `1502.01721`.

[175] H. An and L.-T. Wang, "Opening up the compressed region of top squark searches at 13 TeV LHC," *Phys. Rev. Lett.* **115** (2015) 181602, `1506.00653`.

[176] G. Belanger, D. Ghosh, R. Godbole, and S. Kulkarni, "Light stop in the MSSM after LHC Run 1," *JHEP* **09** (2015) 214, `1506.00665`.

[177] A. Kobakhidze, N. Liu, L. Wu, J. M. Yang, and M. Zhang, "Closing up a light stop window in natural SUSY at LHC," *Phys. Lett.* **B755** (2016) 76–81, `1511.02371`.

[178] H.-C. Cheng, L. Li, and Q. Qin, "Second Stop and Sbottom Searches with a Stealth Stop," `1607.06547`.

[179] T. Plehn, M. Spannowsky, M. Takeuchi, and D. Zerwas, "Stop Reconstruction with Tagged Tops," *JHEP* **10** (2010) 078, `1006.2833`.

[180] X.-J. Bi, Q.-S. Yan, and P.-F. Yin, “Probing Light Stop Pairs at the LHC,” *Phys. Rev.* **D85** (2012) 035005, `1111.2250`.

[181] T. Plehn, M. Spannowsky, and M. Takeuchi, “Stop searches in 2012,” *JHEP* **08** (2012) 091, `1205.2696`.

[182] D. S. M. Alves, M. R. Buckley, P. J. Fox, J. D. Lykken, and C.-T. Yu, “Stops and $\not{E}_T$: The shape of things to come,” *Phys. Rev.* **D87** (2013), no. 3, 035016, `1205.5805`.

[183] D. E. Kaplan, K. Rehermann, and D. Stolarski, “Searching for Direct Stop Production in Hadronic Top Data at the LHC,” *JHEP* **07** (2012) 119, `1205.5816`.

[184] M. R. Buckley, T. Plehn, and M. Takeuchi, “Buckets of Tops,” *JHEP* **08** (2013) 086, `1302.6238`.

[185] **ATLAS** Collaboration, “Search for the Supersymmetric Partner of the Top Quark in the Jets+Emiss Final State at sqrt(s) = 13 TeV,” Tech. Rep. ATLAS-CONF-2016-077, CERN, Geneva, Aug, 2016.

[186] **CMS** Collaboration, “Search for direct top squark pair production in the fully hadronic final state in proton-proton collisions at sqrt(s) = 13 TeV corresponding to an integrated luminosity of 12.9/fb,” Tech. Rep. CMS-PAS-SUS-16-029, CERN, Geneva, 2016.

[187] G. Kasieczka, T. Plehn, T. Schell, T. Strebler, and G. P. Salam, “Resonance Searches with an Updated Top Tagger,” *JHEP* **06** (2015) 203, `1503.05921`.

[188] C. G. Lester and D. J. Summers, “Measuring masses of semiinvisibly decaying particles pair produced at hadron colliders,” *Phys. Lett.* **B463** (1999) 99–103, `hep-ph/9906349`.

[189] I. Low, “Polarized charginos (and top quarks) in scalar top quark decays,” *Phys. Rev.* **D88** (2013), no. 9, 095018, `1304.0491`.

[190] Y. L. Dokshitzer, G. D. Leder, S. Moretti, and B. R. Webber, “Better jet clustering algorithms,” *JHEP* **08** (1997) 001, `hep-ph/9707323`.

[191] J. Thaler and K. Van Tilburg, “Maximizing Boosted Top Identification by Minimizing N-subjettiness,” *JHEP* **02** (2012) 093, `1108.2701`.

[192] J. M. Butterworth, A. R. Davison, M. Rubin, and G. P. Salam, “Jet substructure as a new Higgs search channel at the LHC,” *Phys. Rev. Lett.* **100** (2008) 242001, `0802.2470`.

[193] **CMS** Collaboration, C. Collaboration, “Boosted Top Jet Tagging at CMS,”.

[194] **CMS** Collaboration, “Identification of b quark jets at the CMS Experiment in the LHC Run 2,” Tech. Rep. CMS-PAS-BTV-15-001, CERN, Geneva, 2016.

[195] A. Barr, C. Lester, and P. Stephens, “m(T2): The Truth behind the glamour,” *J. Phys.* **G29** (2003) 2343–2363, `hep-ph/0304226`.

[196] H.-C. Cheng and Z. Han, “Minimal Kinematic Constraints and m(T2),” *JHEP* **12** (2008) 063, `0810.5178`.

[197] **CMS** Collaboration, V. Khachatryan *et al.*, “Search for pair-produced vector-like B quarks in proton-proton collisions at $\sqrt{s} = 8$ TeV,” `1507.07129`.

[198] K. S. Babu, C. F. Kolda, and J. March-Russell, “Implications of generalized Z - Z-prime mixing,” *Phys. Rev.* **D57** (1998) 6788–6792, `hep-ph/9710441`.

[199] V. D. Barger and K. Whisnant, “Heavy Z Boson Decays to Two Bosons in $E(6)$ Superstring Models,” *Phys. Rev.* **D36** (1987) 3429.

[200] A. Leike, “The Phenomenology of extra neutral gauge bosons,” *Phys. Rept.* **317** (1999) 143–250, `hep-ph/9805494`.

[201] J. Alwall, R. Frederix, S. Frixione, V. Hirschi, F. Maltoni, O. Mattelaer, H. S. Shao, T. Stelzer, P. Torrielli, and M. Zaro, “The automated computation of tree-level and next-to-leading order differential cross sections, and their matching to parton shower simulations,” *JHEP* **07** (2014) 079, `1405.0301`.

[202] M. Cacciari, G. P. Salam, and G. Soyez, “FastJet User Manual,” *Eur. Phys. J.* **C72** (2012) 1896, `1111.6097`.

[203] C. Borschensky, M. Krmer, A. Kulesza, M. Mangano, S. Padhi, T. Plehn, and X. Portell, “Squark and gluino production cross sections in pp collisions at $\sqrt{s} = 13$, 14, 33 and 100 TeV,” *Eur. Phys. J.* **C74** (2014), no. 12, 3174, `1407.5066`.